2015-12-15

# Evaluation of the Crystalline Lens Gradient Refractive Index using Laser Ray Tracing and Optical Coherence Tomography

Bianca M. Heilman
*University of Miami*, b.maceo@umiami.edu

UNIVERSITY OF MIAMI

# EVALUATION OF THE CRYSTALLINE LENS GRADIENT REFRACTIVE INDEX USING LASER RAY TRACING AND OPTICAL COHERENCE TOMOGRAPHY

By

Bianca Maceo Heilman

A DISSERTATION

Submitted to the Faculty
of the University of Miami
in partial fulfillment of the requirements for
the degree of Doctor of Philosophy

Coral Gables, Florida

December 2015

UNIVERSITY OF MIAMI

A dissertation submitted in partial fulfillment of
the requirements for the degree of
Doctor of Philosophy

# EVALUATION OF THE CRYSTALLINE LENS GRADIENT REFRACTIVE INDEX USING LASER RAY TRACING AND OPTICAL COHERENCE TOMOGRAPHY

Bianca Maceo Heilman

Approved:

| | |
|---|---|
| Fabrice Manns, Ph.D.<br>Professor of Biomedical<br>Engineering and Ophthalmology | Sonia H. Yoo, M.D.<br>Professor of Ophthalmology and<br>Biomedical Engineering |
| Jean-Marie Parel, Ph.D.<br>Henri and Flore Lesieur Chair in<br>Ophthalmology, Research Associate<br>Professor of Ophthalmology<br>and Biomedical Engineering | Jorge Bohorquez, Ph.D.<br>Associate Professor of<br>Professional Practice of<br>Biomedical Engineering |
| Arthur Ho, M.Optom., Ph.D., FAAO<br>Chief Technologist,<br>Brien Holden Vision Institute<br>Professorial Visiting Fellow,<br>School of Optometry and Vision<br>Science, University of New South<br>Wales, Sydney, Australia | Noel Ziebarth, Ph.D.<br>Assistant Professor of<br>Biomedical Engineering |
| | Dean of the Graduate School |

HEILMAN, BIANCA MACEO (Ph.D., Biomedical Engineering)

Evaluation of the Crystalline Lens Gradient Refractive Index using Laser Ray Tracing And Optical Coherence Tomography (December 2015)

Abstract of a dissertation at the University of Miami.

Dissertation supervised by Professor Fabrice Manns.
No. of pages in text. (112)

The human crystalline lens is a complex and intricate structure that continuously grows throughout our lifetime. The crystalline lens has a non-uniform distribution of protein concentrations which produces an optical gradient within the lens in both the optical and equatorial axes. This gradient refractive index is a unique property of the crystalline lens that significantly contributes to its optical power and aberrations. The objective of this dissertation is to gain a better understanding of the relationship between the crystalline lens shape, its non-uniform gradient refractive index, the lens optical power and aberrations, and their changes with accommodation and age. The information acquired in this dissertation will be used to optimize vision correction procedures and to develop a more accurate lens model to predict the power and aberrations of the whole eye. The studies of this project include establishing techniques to quantify the gradient's contribution to the accommodative amplitude, measuring the optical power and spherical aberration of the lens using laser ray tracing, and developing an enhanced laser ray tracing system which allows for on-axis and off-axis measurements of power and 2-D wavefront aberration maps of the crystalline lens.

## DEDICATION

I lovingly dedicated this dissertation in memory of my grandmother, Alina Raquel Menendez. She always encouraged me to follow my dreams and to pursue what makes me happy. The struggles she faced leaving Cuba to come to the United States, and the sacrifices she made for our family helped shape me into the woman I am today. She is dearly missed, but her beautiful spirit and cheerful nature will continue to live on through me.

**ACKNOWLEDGEMENTS**

My most sincere thanks go to my mentors, Dr. Fabrice Manns and Dr. Jean-Marie Parel, for their guidance and support. A great mentor has the ability to share their wisdom, inspire students and help them to succeed. I was fortunate enough to have two outstanding mentors who spent countless hours in the lab training me and stirring my passion for research. I am forever grateful to have worked so closely with them throughout my undergraduate and graduate studies.

I would like to acknowledge the rest of my dissertation committee: Dr. Jorge Bohorquez, Dr. Arthur Ho, Dr. Sonia Yoo, and Dr. Noel Ziebarth who graciously served on my committee and mentored me throughout my doctoral research.

I am indebted to my colleagues at the Ophthalmic Biophysics Center, both past and present, and our collaborators: Mariela Aguilar, Karam Alawa, Alejandro Arboleda, Dr. Esdras Arrieta, Dr. Robert Augusteyn, Dr. Judith Birkenfeld, David Borja, Florence Cabot, Channing Chang, Alberto de Castro, Carolina de Freitas, Stephanie Delgado, Heather Durkee, Dr. Klaus Ehrmann, Alex Gonzalez, Victor Hernandez, Shawn Kelly, William Lee, Keke Liu, Daniel Lopez, Dr. Susana Marcos, Gabrielle Mesquita, Ashik Mohamed, Kelly Mote, Derek Nankivil, Izuru Nose, Jennifer Rodriguez, Cor Rowaan, Dr. Marco Ruggeri, Juan Silgado, Dr. Stephen Uhlhorn, Dr. Raksha Urs, Dr. Mukesh Taneja, Altricia Williams, Siobhan Williams, and Yue Yao. They provided me with their insight, suggestions, and a helping hand whenever I needed it. This is a very special team and I am honored to have been a part of it.

I would like to thank Dr. Michael Gaines for encouraging me to get involved in research and showing me the potential impact it can have. Participating in the Florida Georgia Alliance for Minority Participation (FGAMP) greatly influenced my decision to pursue a career in biomedical research and I am privileged to have been a part of this exceptional program.

A special thanks to Dr. Josune Urbistondo from Dissertation Writing Group for her help with editing and formatting this dissertation.

I would like to express my deepest gratitude to my parents, Raquel and José Maceo. The sacrifices they made for me and my brother, Joseph, shaped us into the compassionate young adults we are today. They always stressed the value of an education, but more importantly that knowledge is power: "Lo que tu sabes, nadie te lo puede quitar." Thank you for inspiring me to reach for the moon and to pursue "the good life". I love you both and am grateful to be your daughter.

Lastly, I want to thank my husband, Nicholas, whose unwavering love and support has helped me through the challenges of everyday life as well as my Ph.D. I am blessed to have you in my life and I look forward to the next chapter of our lives as we travel across the world to explore the beautiful country of New Zealand.

## TABLE OF CONTENTS

## LIST OF FIGURES

## LIST OF TABLES

## PUBLICATION NOTE

The following are peer-reviewed articles, conference proceedings, presentations, and posters that were published as a direct result of this project:

**Peer-Reviewed Publications:**

**Maceo Heilman B**, Manns F, Ruggeri M, Ho A, Gonzalez A, Rowaan C, Bernal A, Arrieta E, Parel J-M. Accommodative changes in crystalline lens off-axis power. *Investigative Ophthalmology and Visual Science*; In preparation.

**Maceo Heilman B,** Manns F, de Castro A, Durkee H, Arrieta E, Marcos S, Parel J-M. Changes in monkey crystalline lens spherical aberration during simulated accommodation in a lens stretcher. *Investigative Ophthalmology & Visual Science*, 56(3):1743-1750, **2015**.

de Castro A, Birkenfeld J, **Maceo B**, Manns F, Arrieta E, Parel J-M & Marcos S. Influence of shape and gradient refractive index in the accommodative changes of spherical aberration in nonhuman primate crystalline lenses. *Investigative Ophthalmology & Visual Science;* 54(9):6197-6207, **2013**.

**Maceo BM**, Manns F, Borja D, Nankivil D, Uhlhorn S, Arrieta E, Ho A, Augusteyn RC, Parel J-M. Contribution of the crystalline lens gradient refractive index to the accommodation amplitude in non-human primates: In vitro studies. *Journal of Vision;* 11(13): 1–13, **2011**.

**Conference Proceedings and Presentations:**

**Maceo Heilman B**, Ruggeri M, Gonzalez A, Rowaan CJ, Bernal A, Arrieta E, Ho A, Manns F, Parel J-M. Combined laser ray tracing and optical coherence tomography system to measure changes in lens shape and on-axis and off-axis focal length with accommodation. *Association for Research in Vision and Ophthalmology (ARVO) Annual Meeting Abstract and Poster Presentation* #1075; Denver, CO, **2015.**

Manns F, **Maceo Heilman B**, Ho A, Parel J-M. Anatomically-accurate paraxial optical model of cynomolgus lens accommodation with continuous gradient. *Association for Research in Vision and Ophthalmology (ARVO) Annual Meeting Abstract and Poster Presentation* #5998; Denver, CO, **2015.**

**Maceo BM**, de Castro A, Birkenfeld J, Arrieta E, Parel J-M, Marcos S & Manns F. Lens spherical aberrations in cynomolgus monkeys: Comparison of laser ray tracing measurements and reconstructed GRIN model predictions. *Association for Research in Vision and Ophthalmology (ARVO) Annual Meeting Abstract and Poster Presentation* #3776; Orlando, FL, **2014.**

de Castro A, Birkenfeld J, **Maceo BM**, Ruggeri M, Arrieta EA, Parel J-M, Manns F & Marcos S. Crystalline lens gradient refractive index and posterior surface shape from multiple orientations OCT imaging: towards a reconstruction in vivo? *Association for Research in Vision and Ophthalmology (ARVO) Annual Meeting Abstract and Poster Presentation* #3788; Orlando, FL, **2014.**

**Maceo B.** Ex vivo studies of crystalline optics in human and primate lenses using a lens stretcher. *International Conference on the Lens Abstract and Presentation;* Kona, Hawaii, **2014.**

**Maceo BM**, Manns F, de Castro A, Uhlhorn S, Arrieta E, Marcos S, Parel J-M. Lens spherical aberration changes in cynomolgus monkeys during simulated accommodation in a lens stretcher. *Association for Research in Vision and Ophthalmology (ARVO) Annual Meeting Abstract and Poster Presentation* #4272; Seattle, WA, **2013.**

**Maceo BM**, Manns F, Nankivil D, Arrieta E, Esfandiari P, Durkee H, Alawa K, Parel J-M. Age-related changes in lens power, thickness and surface curvatures with stretching force during simulated accommodation in baboons. *Association for Research in Vision and Ophthalmology (ARVO) Annual Meeting Abstract and Presentation* #2226; Ft Lauderdale, FL, **2012.**

Manns F, **Maceo BM**, Ho A, Parel J-M. Age-dependence of the paraxial refractive index gradient and its power in the baboon lens. *Association for Research in Vision and Ophthalmology (ARVO) Annual Meeting Abstract and Presentation* #2231; Ft Lauderdale, FL, **2012**.

**Maceo BM**, Borja D, Nankivil D, Uhlhorn S, Arrieta E, Manns F, Ho A, Augusteyn RC, Parel J-M. Age-related changes in the anterior and posterior surface lens curvatures during simulated accommodation in hamadryas baboons. *Association for Research in Vision and Ophthalmology (ARVO) Annual Meeting Abstract and Presentation* #3403; Ft Lauderdale, FL, **2011**.

Manns F, **Maceo B**, Ho A, Parel J-M. Contribution of the refractive index gradient to the spherical aberration of the human crystalline lens. *Association for Research in Vision and Ophthalmology (ARVO) Annual Meeting Abstract and Presentation* #3406; Ft Lauderdale, FL, **2011**.

Nankivil D, Urs R, **Maceo B,** Arrieta E, Manns F, Ho A, Augusteyn R, Parel J-M. A comparison of biometric properties of the isolated human lens derived from optical coherence tomography, ultrasound biomicroscopy and shadowphotogrammetry. *Association for Research in Vision and Ophthalmology (ARVO) Annual Meeting Abstract and Poster* #1114; Ft Lauderdale, FL, **2011**.

**Maceo B**, Borja D, Nankivil D, Manns F, Uhlhorn SR, Arrieta E, Ho A, Parel JM. Surface and internal power change of the non-human primate crystalline lens during simulated accommodation. *Association for Research in Vision and Ophthalmology (ARVO) Annual Meeting Abstract and Presentation* #5786; Ft Lauderdale, FL, **2010**.

**Maceo BM**, Borja D, Narasimhan S, Nankivil D, Manns F, Uhlhorn SR, Ho A, Parel JM. Age-dependent changes in non-human primate lens surface curvatures during simulated accommodation. *Association for Research in Vision and Ophthalmology (ARVO) Annual Meeting Abstract and Presentation #4289*; Ft Lauderdale, FL, **2009**.

**Maceo BM**, Borja D, Narasimhan S, Nankivil D, Manns F, Uhlhorn SR, Ho A, Parel JM. Age-dependent changes in non-human primate lens surface curvatures during simulated accommodation. *Florida-Georgia Louis Stokes Alliance for Minority Participation (FGLSAMP) Exposition Abstract and Poster;* Miami, FL, **2009**.

**Other related works published during the course of my doctoral studies:**

**Peer-Reviewed Publications:**

Augusteyn RC, **Maceo Heilman B**, Ho A, Parel J-M. Non-human primate ocular biometry. *Investigative Ophthalmology & Visual Science*. **In Press**.

Marussich L, Manns F, Nankivil D, **Maceo Heilman B,** Yao Y, Arrieta-Quintero E, Ho A, Augusteyn R, Parel JM. Measurement of crystalline lens volume during accommodation in a lens stretcher. *Investigative Ophthalmology & Visual Science*, 56(8):4239-4248, **2015**.

Nankivil D, **Maceo Heilman B**, Durkee H, Manns F, Ehrmann K, Kelly S, Arrieta E, Parel J-M A. The zonules selectively alter the shape of the lens during accommodation based on the location of their anchorage points. *Investigative Ophthalmology & Visual Science;* 56(3):1751-1760, **2015**.

Augusteyn RC, Nankivil D, Mohamed A, **Maceo B**, Pierre F, Parel J-M. Human ocular biometry. *Experimental Eye Research;* 102:70-5, **2012**.

**Conference Proceedings and Presentations:**

Augusteyn R, **Maceo B**, Mohamed A, Parel J-M. Are monkeys good models for studying ageing of human vision? *International Conference on the Lens Abstract and Presentation;* Kona, Hawaii, **2014.**

Parel J-M, Durkee H, Kelly S, **Maceo B**, Nankivil D, Aguilar MC, Arrieta E, Manns F, Ehrmann K, Ho A, Yanrong S, Bassnett S, Augusteyn RC. Morphology and physical properties of the zonular framework in primates. *International Conference on the Lens Abstract and Presentation;* Kona, Hawaii, **2014.**

Parel J-M, **Maceo BM**, Rowaan CJ, Manns F, Arrieta E. Effect of temperature on lens power, anterior and posterior surface lens curvatures and force during simulated accommodation in cynomolgus monkeys. *Association for Research in Vision and Ophthalmology (ARVO) Annual Meeting Abstract and Poster Presentation* #4271; Seattle, WA, **2013.**

Augusteyn R.C., **Maceo BM**, Nankivil D, Mohamed A, Alawa K, Parel J-M. Human ocular biometry. *Association for Research in Vision and Ophthalmology (ARVO) Annual Meeting Abstract and Poster* #4925; Ft Lauderdale, FL, **2012**.

Enten AC, Nankivil D, **Maceo B**, Arrieta E, Manns F, Parel J-M. Optomechanical response of primate lenses: Effects of decentration. *Association for Research in Vision and Ophthalmology (ARVO) Annual Meeting Abstract and Poster* #964; Ft Lauderdale, FL, **2011**.

Freitas CP, Ruggeri M, **Maceo B**, Uhlhorn S, Arrieta E, Manns F, Augusteyn R, Ho A, Parel J-M. Internal crystalline lens structure imaging using long range optical coherence tomography. *Association for Research in Vision and Ophthalmology (ARVO) Annual Meeting Abstract and Poster* #966; Ft Lauderdale, FL, **2011**.

Ho A, Manns F, **Maceo B**, Borja D, Uhlhorn S, Arrieta E, Parel J-M. Estimation of central average group refractive index of crystalline lens from optical thickness measurements. *Association for Research in Vision and Ophthalmology (ARVO) Annual Meeting Abstract and Poster* #963; Ft Lauderdale, FL, **2011**.

Marussich L, Nankivil D, **Maceo B**, Arrieta E, Urs R, Manns F, Ho A, Augusteyn R, Parel J-M. Changes in primate crystalline lens volume during simulation of accommodation in a lens stretcher. *Association for Research in Vision and Ophthalmology (ARVO) Annual Meeting Abstract and Poster* #962; Ft Lauderdale, FL, **2011**.

Nankivil D, **Maceo B**, Borja D, Arrieta E, Manns F, Parel JM. The effect of posterior zonular transection on the baboon lens during stretching. *Association for Research in Vision and Ophthalmology (ARVO) Annual Meeting Abstract and Poster #796*; Ft Lauderdale, FL, **2010**.

Nankivil D, **Maceo B**, Dias J, Borja D, Arrieta E, Manns F, Parel JM. Change in zonular tension of the cynomolgus monkey during lens stretching. *Association for Research in Vision and Ophthalmology (ARVO) Annual Meeting Abstract and Poster #2798;* Ft Lauderdale, FL, **2009**.

# CHAPTER 1

## AIMS OF THE STUDY

The human eye grows rapidly during the prenatal stages of development and continues to grow throughout the first year of life. The corneal and globe dimensions reach their maximum size at around 1.2 years (Augusteyn et al., 2012). Unlike the rest of the eye, the crystalline lens continuously grows throughout our lifetime (Augusteyn, 2010). Due to this continued growth, the dimensions of the lens as well as the optical and mechanical properties change with age.

Changes in the optical properties of the lens with age influence the optics of the whole eye and contribute to a decrease in overall visual quality. It is challenging to obtain *in vivo* measurements of the crystalline lens power and aberrations due to its position behind the cornea and iris. The development of lens stretching devices that reproduce accommodation in post-mortem tissue has allowed for the study of lens accommodation *in vitro*. With these devices, it is possible to acquire direct measurements of the lens shape, power and aberrations.

One unique characteristic of the crystalline lens is that it has a non-uniform distribution of protein concentrations which produces an optical gradient within the lens (Augusteyn, 2010; Smith, 2003). The gradient is an important and distinctive property of the lens that significantly contributes to its optical power and aberrations (Atchison & Smith, 2000; Garner & Smith, 1997; Smith, 2003; Tabernero, Berrio, & Artal, 2011). The gradient also changes with age.

The objective of this dissertation is to gain a better understanding of the relationship between the crystalline lens shape, its non-uniform gradient refractive index,

the lens optical power and aberrations, and their changes with accommodation and age. The information acquired in this dissertation will be used to optimize vision correction procedures, particularly wavefront guided treatments, and to develop a more accurate lens model to predict the power and aberrations of the whole eye. The three specific aims of the proposed study are:

**Aim 1: Quantify the contribution of the lens gradient refractive index to accommodation and presbyopia**

*Ex vivo* lenses will be placed in a second generation lens stretcher (EVAS II) to measure changes in the lens power, thickness and shape during simulated accommodation. Lens stretching experiments will be performed over a broad age range of non-human primate crystalline lenses. The results will be used to quantify the gradient's contribution to the accommodative amplitude and its contribution to the loss of accommodation with age.

**Aim 2: Quantify the contribution of the gradient refractive index to lens spherical aberration**

A Laser Ray Tracing (LRT) system will be designed and built to measure the changes in lens spherical aberration during simulated accommodation in a motorized lens stretcher. The LRT uses a translating image sensor to record images of the individual rays passing through the lens. These images will be processed to recreate the ray slopes and measure the spherical aberration of the crystalline lens. These results will provide insight

into the gradient's role in lens spherical aberration and how spherical aberration changes with accommodation and age.

**Aim 3: Develop a system to measure the off-axis power and aberrations of the crystalline lens**

The LRT system developed in Aim 2 will be enhanced to allow on-axis and off-axis measurements of power and 2-D wavefront aberration maps of the crystalline lens. The beam delivery optics will be mounted on a motorized rotation stage that pivots around the crystalline lens to allow acquisition of off-axis spot patterns. An imaging sensor mounted on a two-dimensional motorized positioning stage below the lens will be used to record the spot positions along each individual ray for all delivery angles. The first application of the LRT system will be to measure the on- and off-axis power of the lens in the accommodated (unstretched) and relaxed (stretched) states. Off-axis power measurements will enable us to characterize the changes in lens power with field angle and to study how accommodation impacts these changes.

# CHAPTER 2

# BACKGROUND AND SIGNIFICANCE

## 2.1 Motivation

The research aims of this dissertation were driven by Phaco-Ersatz. Phaco-Ersatz (Parel et al., 1986) is a lens refilling technique for cataract surgery in which the hardened lens contents are replaced with an elastic polymer which has similar optical and mechanical properties to that of a young human crystalline lens. The successful clinical realization of Phaco-Ersatz requires the coordinated development of new optical, surgical and polymer technologies. In order to meet these demands, a large multi-disciplinary and multi-institutional research program was established between the Vision Cooperative Research Centre (Vision CRC) in Sydney, Australia and the Ophthalmic Biophysics Center (OBC) at the Bascom Palmer Eye Institute in Miami. The goal of the project is to develop the polymers, surgical techniques, and *ex vivo* optical and mechanical testing platforms to optimize the Phaco-Ersatz lens refilling procedure.

Along the way, the Phaco-Ersatz project raised some fundamental questions about the optical properties of the crystalline lens: How does a lens refilled with a material of uniform refractive index compare to the natural lens which has a gradient refractive index? What role does the gradient play in influencing lens power and aberrations? How does the shape and refractive index of the lens affect the accommodative response? These questions were the driving factors for the research described in this dissertation.

## 2.2 The lens

The cornea and crystalline lens refract the light rays entering the eye and focus them onto the retina. The total optical power of the eye is determined by the combined power of its focusing elements. Roughly two-thirds of the eye's focusing power is produced by the cornea while the remaining one-third is produced by the lens (Atchison & Smith, 2000). Unlike the cornea which has a relatively fixed power throughout adulthood, the power of the crystalline lens changes with age.

The lens can also change shape in order to produce a variable amount of power. This change in lens shape enables the eye to change focus. The optical power of the crystalline lens is determined by the surface curvatures, the refractive index differences at the aqueous-lens and lens-vitreous interfaces, and the refractive index gradient distribution within the lens (Atchison & Smith, 2000).

## 2.3 Crystalline lens optics and structure

The human crystalline lens is a complex and intricate structure that continuously grows throughout our lifetime (Augusteyn, 2008; Augusteyn, 2010) (Figure 2.1). A typical young adult human lens has a diameter of 9 mm, thickness of 4.5 mm, and anterior and posterior lens surface radii of curvature of 10 mm and 5.5 mm, respectively, in the relaxed state. The contents of the lens (primarily crystallin proteins and fiber cells) are enclosed within a transparent capsular bag. The capsular bag is a strong, elastic membrane which provides structural support and molds the shape of the lens (Fincham, 1937; Fisher, 1969; Glasser & Kaufman, 1999).

The crystalline lens has a non-uniform distribution of protein concentrations which produces an optical gradient within the lens in both the optical and equatorial axes (Augusteyn, 2010; Smith, 2003). This gradient refractive index (GRIN) is a unique property of the crystalline lens that significantly contributes to its optical power and aberrations (Atchison & Smith, 2000; Garner & Smith, 1997; Smith, 2003; Tabernero, Berrio, & Artal, 2011). In the young human lens, the refractive index gradually increases from the surface of the lens towards the nucleus Figure 2.2). Refractive index values range from 1.365 at the surface to about 1.415 at the center of the lens (Moffat, Atchison & Pope, 2002; Jones et al., 2005; Kasthurirangan et al., 2008; Augusteyn, 2008).

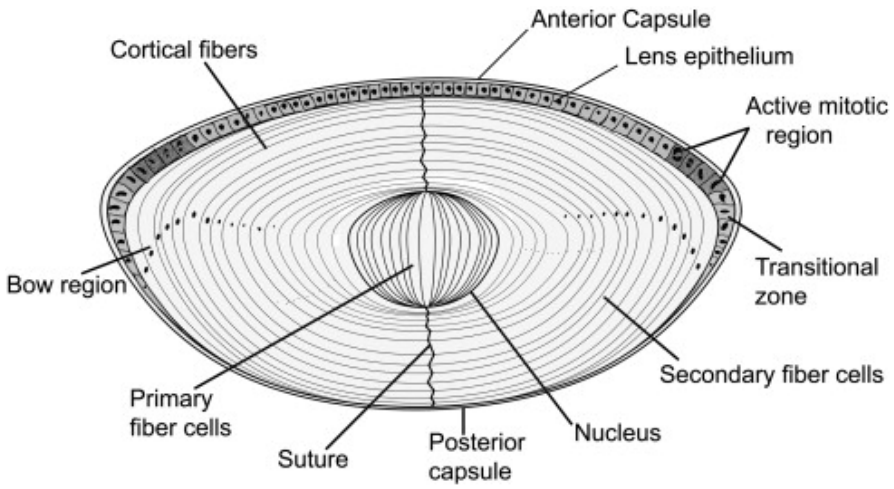


**Figure 2.1:** Schematic of the crystalline lens showing the single layer of epithelial cells covering the anterior cross-section (Sharma & Santhoshkumara, 2009). The elongated fiber cells are directly in contact with the epithelial layer in the anterior region and make contact with the capsule in the posterior region. The cells differentiate, elongate, lose their organelles in the lens bow region and start to form newly differentiated fiber cells.

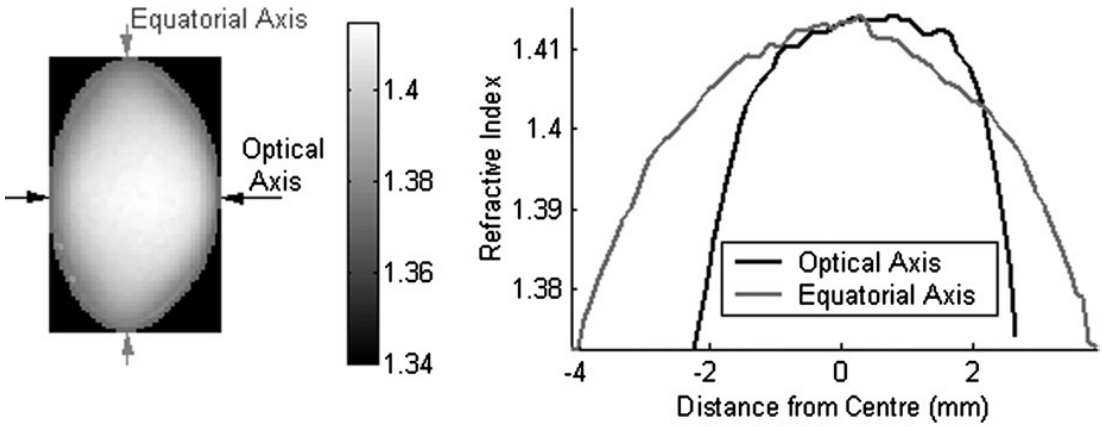


**Figure 2.2:** Refractive index maps (Left) and profiles (Right) for a 7-year-old human crystalline lens (Jones et al., 2005). The refractive index gradually increases from the surface of the lens towards the center in the optical and equatorial axes.

## 2.4 Accommodation

The lens contributes roughly one third of the eye's total refractive power, but the major role of the lens is to allow the eye to change focus in a process called accommodation. Accommodation is the eye's ability to gradually increase and decrease optical power over a continuous range of distances. Accommodation is the result of changes in the crystalline lens shape. The most widely accepted theory of accommodation is the Helmholtz theory (Helmholtz, 1855; Gullstrand, 1909).

According to the Helmholtz theory, the lens changes shape as a result of ciliary muscle contraction and relaxation. When the ciliary muscle is relaxed, the zonules are under tension and pull on the lens capsule; thus, flattening the anterior and posterior surfaces of the lens (Figure 2.3, Left). In this relaxed (unaccommodated) state, the flattened lens surfaces result in a decrease in optical power and the eye is adjusted for distance vision. In the accommodated state, the ciliary muscle contracts releasing the tension on the zonular fibers and allowing them to relax. When the zonules are no long under tension, the lens assumes a rounder shape and the thickness increases (Figure 2.,

Right). The curved lens surfaces produce an increase in optical power and the eye is adjusted for near vision (Charman, 2008; Fincham, 1937).

Since the lens changes shape with accommodation, it is reasonable to expect that the GRIN profile also changes with accommodation. *In vivo* studies using magnetic resonance imaging (MRI) found that the central and peripheral refractive indices do not change significantly with accommodation, but that there is a change in the distribution of the refractive index (Kasthurirangan et al., 2008). According to Gullstrand's intracapsular theory of accommodation, changes in the internal structure of the lens contribute to the accommodation amplitude (Gullstrand, 1909; Gullstrand, 1911).

In order to account for the contribution of the GRIN, Gullstrand used a higher equivalent refractive index in the lens of his schematic eye in the accommodated state rather than in the relaxed state. On the contrary, more recent studies have shown that the equivalent index of the lens does not change with accommodation (Garner & Smith, 1997; Hermans, Dubbelman, Van der Heijde, & Heethaar, 2008). Understanding the gradient's role in accommodation is valuable for the Phaco-Ersatz project because the natural lens containing a gradient refractive index is replaced with a homogenous material of uniform refractive index. This has an impact on retinal image quality, and the power and aberrations of the whole eye.

## 2.5 Presbyopia

As the crystalline lens continues to grow with age, it gradually loses its ability to change shape, resulting in the progressive loss of accommodation (Glasser & Campbell, 1999; Dubbelman & Van der Heijde, 2001; Dubbelman et al., 2005). Presbyopia is the

loss of near visual function that results from the progressive loss of accommodation with age (Weale, 1989; Kaufman, 1992; Werner et al., 2000). Symptoms of presbyopia commence at around 40-50 years of age. In 2005, there were approximately 1.04 billion people worldwide with presbyopia (Holden et al., 2008). Although the true cause of presbyopia is still unknown, the most widely accepted cause is attributed to stiffening of the crystalline lens with age.

The mechanical properties of the lens affect its ability to change shape with accommodation (Atchison, 1995; Glasser & Campbell, 1998; Glasser & Campbell, 1999; Weeber et al., 2007; Heys, Cram & Truscott, 2004). Evidence has shown that lens hardness measurements vary between the nucleus and cortex, and that the hardness of these regions gradually increases with age (Fisher, 1971; Pau & Kranz, 1991; Tabandeh et al., 1994; Weeber et al., 2005).

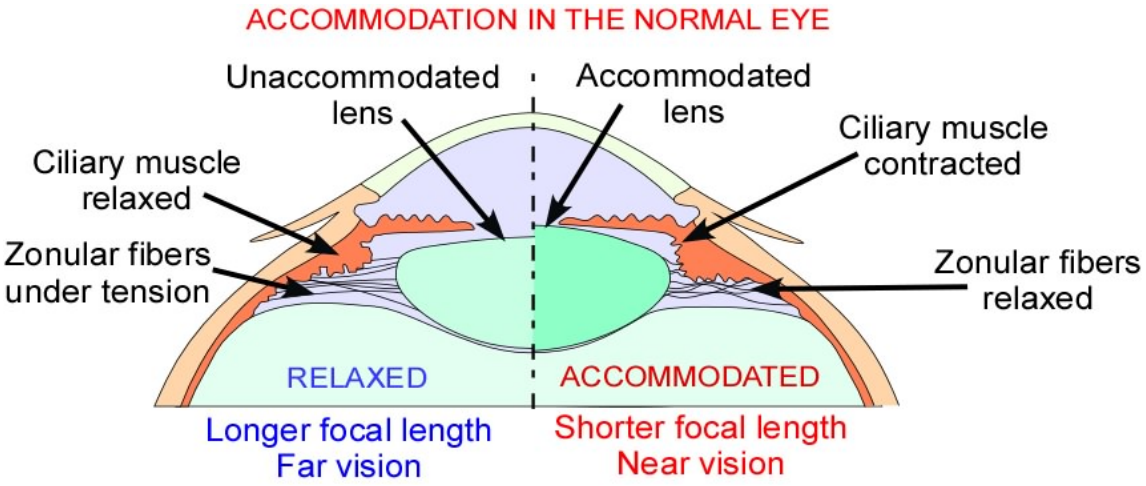


**Figure 2.3:** Accommodation in the normal eye. (Left) When the eye is in the relaxed state, the ciliary muscle is relaxed, applying tension on the zonular fibers which pull on the lens capsule. The lens surfaces assume a flatter shape and the eye is adjusted for far vision. (Right) In the accommodated state, the ciliary muscle is contracted which releases the tension on the zonular fibers. The lens assumes a rounder shape and the eye is adjusted for near vision (Modified from drawing by Dr. Fabrice Manns).

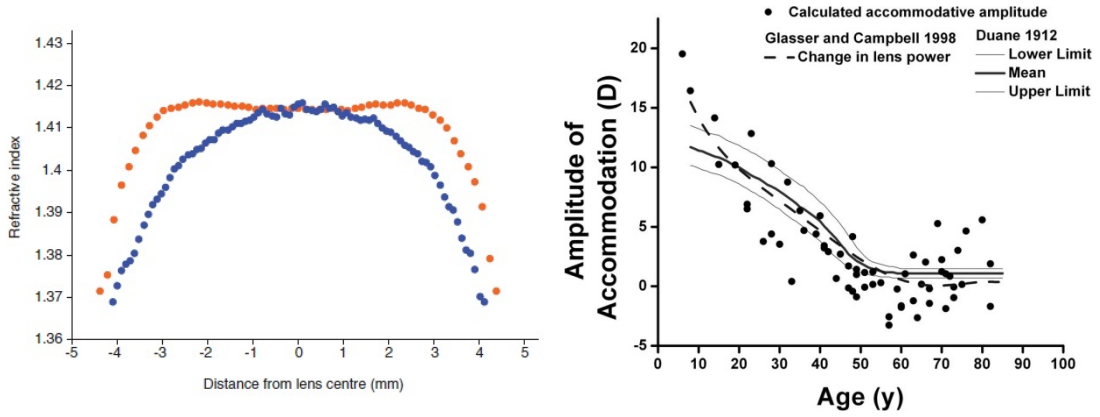


**Figure 2.4:** (Left) Refractive index profiles along the optical axis for a 27- (blue dots), and 63- (orange dots) year-old human lenses obtained using magnetic resonance imaging (MRI) (Augusteyn, Jones & Pope, 2008). (Right) The gradual decrease of accommodation amplitude with age from Duane's study compared with the changes in isolated lens power measured at the OBC (black dots) and by Glasser & Campbell (dashed line) (Borja et al., 2008a).

The lens undergoes age-related changes in its optical properties as well. The refractive index distribution becomes relatively uniform in the central region of the lens, forming a plateau (Augusteyn, Jones & Pope, 2008; Jones et al., 2005; Moffat, Atchison & Pope, 2002). As seen in **Error! Reference source not found.** (Left), the refractive index profile of a 27-year-old human crystalline lens gradually increases from the surface of the lens to the center, forming a parabolic shaped curve. In the 63-year-old human, the refractive index is approximately uniform (n = 1.415) in the central 6-mm region, and there is a steep decrease in refractive index towards the periphery of the lens. There is evidence that the size of the refractive index plateau increases with age (Augusteyn, Jones & Pope, 2008; Jones et al., 2005; Moffat, Atchison & Pope, 2002; de Castro et al., 2011; Kasthurirangan et al., 2008).

Studies on isolated lenses suggest that changes in the refractive index distribution with age decrease both the optical power of the lens and the contribution of the gradient to the lens power (Borja et al., 2008; Borja, Manns et al., 2010; Glasser & Campbell,

1999; Jones et al., 2005). Coincidentally, the power of the isolated lens decreases with age at a rate which correlates well with the decrease in accommodative amplitude (Figure 2.4, Right). It is possible that the distinct flattening of the GRIN profile may contribute to the gradual decrease in lens power with age. However, a correlation between the GRIN profile and lens power changes has not yet been proven.

## 2.6 Importance of gradient optics and missing information

The growing lens poses a difficult challenge since its optical and mechanical properties continuously change with age. Changes in the shape and gradient refractive index of the lens produce changes in the optical power and higher-order aberrations which impact refractive development (Dunne, 1993; Zadnik, 1997; Mutti et al., 1998; Mutti et al., 2000; Sivak, 2008) and the optics of the eye in general (Smith & Pierscionek, 1998; Atchison & Smith, 2001; Smith, 2003; Marcos, 2004) In order to optimize vision correction procedures, particularly wavefront guided treatments and Phaco-Erstaz, we need to gain a better understanding of how changes in the gradient refractive index affect the power and spherical aberrations of the lens and the whole eye. Despite its importance, the changes in the gradient refractive index and its effects on the optics of the crystalline lens and of the whole eye are still not well understood (Smith, 2003; Kasthurirangan et al., 2008).

*In vivo* measurements of the gradient's contribution to accommodation are difficult to obtain because they rely on indirect measurements of lens power or equivalent refractive index (Garner & Smith, 1997). The development of lens stretching systems has allowed us to quantify changes in the lens shape and power during simulated

accommodation (Ehrmann, Ho & Parel, 2008). One of the goals of this project will be to use *in vitro* techniques to determine the gradient's contribution to the accommodation amplitude. This knowledge will guide us in the selection of a suitable polymer and help us to understand the implications of refilling the lens with a uniform material during Phaco-Ersatz.

Additionally, there is increasing interest in studying the peripheral (off-axis) optics of the eye, in particular peripheral refraction, which is associated with refractive error (Charman & Radhakrishnan, 2010). The change in peripheral refraction on accommodation has been correlated with the onset and progression of myopia (Whatham et al., 2009). Little is known about the peripheral optics of the crystalline lens and how the peripheral optics change with accommodation and age. The final aim of this project will focus on measuring the peripheral power of the lens with accommodation.

# CHAPTER 3

# CONTRIBUTION OF THE LENS GRADIENT REFRACTIVE INDEX TO THE CHANGE IN POWER WITH ACCOMMODATION AND AGE[1]

## 3.1 Purpose

In this chapter, we describe the experiments related to Aim 1 of the project. Lens stretching experiments were performed on non-human primate crystalline lenses over a broad age range to measure changes in lens optical power, thickness and shape with accommodation and age. The purpose was to quantify the contribution of the lens gradient refractive index to the accommodative amplitude, and to determine whether its contribution changes with age.

## 3.2 Background and rationale

The contribution of the gradient to the lens power is generally quantified in terms of an "equivalent index," which is the refractive index of a homogeneous lens with the same shape and power as the crystalline lens with gradient index. In vivo and in vitro studies have shown that the equivalent index decreases with age (Borja et al., 2008; Borja, Manns et al., 2010; Dubbelman & Van der Heijde, 2001). This finding is consistent with the observation that the contribution of the gradient index to lens power decreases with age.

In addition to age-related changes, alterations in the refractive index profile must also occur during accommodation since the lens changes shape with accommodation. *In*

[1] The content in this chapter was published in:
Maceo BM, Manns F, Borja D, Nankivil D, Uhlhorn S, Arrieta E, Ho A, Augusteyn RC, Parel J-M. (2011). Contribution of the crystalline lens gradient refractive index to the accommodation amplitude in non-human primates: In vitro studies. *Journal of Vision*, 11(13):23, 1–13.

*vivo* studies using MRI found that the central and peripheral refractive indices do not change significantly with accommodation but that there is a change in the distribution of the refractive index (Kasthurirangan et al., 2008). According to Gullstrand's intracapsular theory of accommodation, changes in the internal structure of the lens contribute to the accommodation amplitude (Gullstrand, 1962/1909, 1911). In order to account for the contribution of the gradient refractive index, Gullstrand used a higher equivalent refractive index in the lens of his schematic eye in the accommodated state than in the relaxed state. However, more recent studies have shown that the equivalent index of the lens does not change during accommodation (Garner & Smith, 1997; Hermans, Dubbelman, Van der Heijde, & Heethaar, 2008). In vivo measurements of the gradient's contribution to lens accommodation are challenging because they require accurate measurements of the lens shape and rely on indirect measurements of lens power and/or equivalent refractive index (Garner & Smith, 1997).

The development of lens stretching devices that reproduce accommodation in post-mortem tissue has allowed for the study of lens accommodation *in vitro* (Glasser & Campbell, 1998; Roorda & Glasser, 2004; Manns et al., 2007; Ehrmann, Ho, & Parel, 2008; Augusteyn et al., 2011). With these devices, it is possible to directly measure the changes in the crystalline lens shape and power and quantify the gradient contribution during simulated accommodation. The *Ex Vivo* Accommodation Simulator II (EVAS II) is a second generation lens stretching system that reproduces the natural processes of accommodation in post-mortem lenses (Ehrmann, Ho, & Parel, 2008) (Figure 3.1, Right). EVAS II was used to measure changes in the lens power and shape with simulated

accommodation to determine the contribution of the gradient refractive index to the accommodative amplitude.

## 3.3 Materials and methods

### *3.3.1 Donor tissue*

Lens stretching experiments were conducted on 36 lenses from 34 cynomolgus monkeys (Macaca fascicularis, postmortem time [PMT], 17.7±12.7 hours; ages, 1.4–14.1 years) and 25 lenses from 19 hamadryas baboons (Papio hamadryas, PMT, 21.64±12.8 hours; ages, 1.8–28.0 years). All experiments adhered to the Association for Research in Vision and Ophthalmology (ARVO) Statement for the Use of Animals in Ophthalmic and Visual Research. The eyes were obtained from the Division of Veterinary Resources at the University of Miami as part of a tissue-sharing protocol and were used in accordance with Institutional Animal Care and Use Guidelines.

The eyes were enucleated immediately after euthanasia, wrapped in gauze, and placed in a closed container. No animals were euthanized for the sole purpose of this study. Upon arrival at the laboratory, all eyes were either directly prepared for stretching experiments or refrigerated at 4ºC (Nankivil et al., 2009).

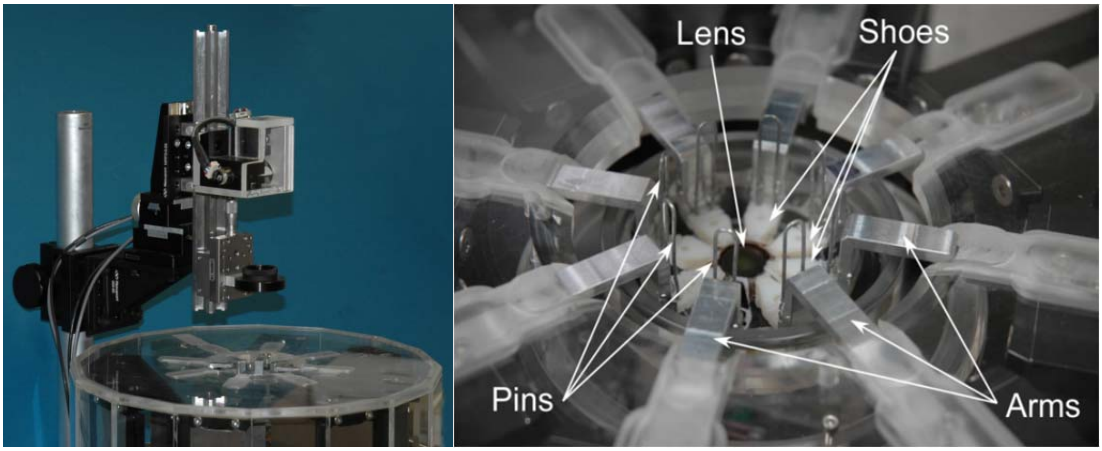


**Figure 3.1:** (Left) Time-domain OCT and EVAS II system. (Right) Ocular tissue mounted in the EVAS II system. The crystalline lens, shoes, pins, and arms are labeled (Nankivil et al. 2015).

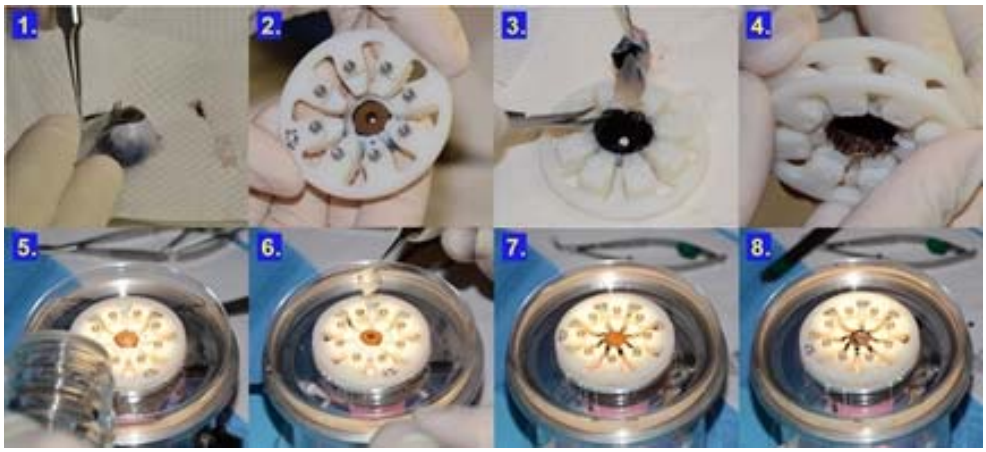


**Figure 3.2:** EVAS II tissue dissection procedure. 1) The extraocular muscles were removed, 2) then the equatorial globe diameter was measured with digital calipers and the best-fitting shoe size was selected. Cyanoacrylate glue was applied to the individual shoes and the eye was aligned and mounted onto the shoes. Once the glue dried, 3) the posterior pole was removed, and 4) the bottom retaining ring was added. 5) The tissue was transferred to a Petri dish atop a custom-made portable dissection stage with diffuse retro-illumination and Dulbecco's modified Eagle's medium was added to preserve the tissue. 6) The cornea was removed and 7) the scleral segments were excised. 8) Lastly, the iris was removed and the tissue is ready to be transferred into the EVAS II system (Nankivil et al. 2015).

### *3.3.2 Tissue preparation*

All tissue dissections were performed by an ophthalmic surgeon (Figure 3.2). The whole globe was bonded to eight scleral attachments (shoes) to maintain the globe's shape integrity during dissection and stretching. Once the shoes were glued to the sclera, the posterior pole was sectioned, and the cornea and iris were removed. Scleral incisions were made in between the adjacent shoes to create eight independent stretching segments

(Ehrmann, Ho & Parel, 2008; Manns et al., 2007). Special care was taken to keep the ciliary body intact. The prepared tissue sample consisting of the ciliary body, zonular fibers, crystalline lens and segmented sclera was then mounted into the lens stretcher.

### *3.3.3 Lens stretching experiments*

EVAS II simultaneously stretches the eight scleral segments radially outward in a step-wise fashion (0.25 mm/step, up to 2.5 mm) (Ehrmann, Ho & Parel, 2008). The tissue was immersed in a small chamber filled with Dulbecco's Modified Eagle Medium (DMEM) throughout the experiment to avoid osmotic swelling.

### *3.3.4 Measurement of anterior and posterior lens surface curvatures and thickness*

For all lenses, one stretching run was performed to quantify the changes in lens shape. Image of the lens cross-section were acquired using a time-domain OCT system (Figure 3.1, Left). At each 0.25 mm increment of stretch, the lens was imaged using a super-luminescent diode with a central wavelength of 825 nm and bandwidth of 25 nm. The system has an optical scan depth of 10 mm and an axial resolution of 12 μm in air (9 μm in tissue) (Uhlhorn et al., 2008). A telecentric beam delivery system is used to produce a meridional B-scan.

The beam delivery system is mounted on a 3-axis translation stage to allow precise centering of the beam in the transverse direction and adjustment of the focus to maximize the signal strength. The beam was aligned prior to the stretching experiment by visualizing the central A-line signal intensity in real-time and adjusting the position of the delivery optics until the signal peaks corresponding to the anterior and posterior lens

surfaces were maximized. Images were recorded with 5000 points/A-line, 500 A-lines/B-scan and a lateral scan length of 10 mm or 12 mm depending on the size of the lens. In some cases, the lens may shift slightly or de-center during a simulated accommodation experiment. In a separate study, the effect of lens decentration on the lens thickness, diameter, radius of curvature, and power measurements were determined to cause less than 1% error. Therefore, lens decentration was considered negligible (Enten et al., 2011).

The OCT images were processed using a semiautomatic edge-detection program developed in MATLAB (MathWorks, Natick, MA) to detect the boundaries of the anterior and posterior lens surfaces. Residual tilt of the lens was corrected by fitting the anterior and posterior surface profiles to a $10^{th}$-order Fourier series consisting of cosine functions in a polar-coordinate system which included terms for tilt and decentration (Urs, Ho, Manns & Parel, 2010). The image was scaled in the axial direction to convert optical distances to geometrical distances using the measured group refractive index of DMEM (n = 1.345 at 825 nm; Borja, Siedlecki et al., 2010) and an estimate of the average group refractive index of the crystalline lens based on the age of the primate. A correction factor was applied to convert human age to equivalent NHP age (NHP age = human age/3; Borja, Manns et al., 2010), assuming the age dependence of the group refractive index in NHPs is similar to that of the human lenses in Uhlhorn et al. (2008).

Distortions on the posterior surface due to refraction at the anterior surface of the lens were corrected using an exact ray trace based on the method from Borja, Siedlecki et al., 2010. The distortion correction technique assumes a uniform refractive index equal to the average index of the lens. The anterior lens shape and corrected posterior lens surface

were then fit over the central 3-mm optical zone with a spherical fit to calculate the radius of curvature for the anterior surface, $R_a$, and posterior surface, $R_p$. For all lenses, the axial lens thickness was directly measured from the scaled images (Figure 3.3).

### *3.3.5 Measurement of lens power*

Following the stretching run to measure lens shape, three additional stretching runs were performed to quantify the changes in lens power for all eyes. The power reported is the average of the three measurements obtained at each step. The optical system uses the OCT light source and beam delivery system. For power measurements, the scanners were programmed to produce a circular ring pattern with a 1.5-mm scan radius. The ring was positioned at the center of the anterior lens surface and the location below the lens where the ring converges to a single spot is detected by a camera mounted on an adjustable vertical translation stage. This location corresponds to the focal point in the image space of the lens.

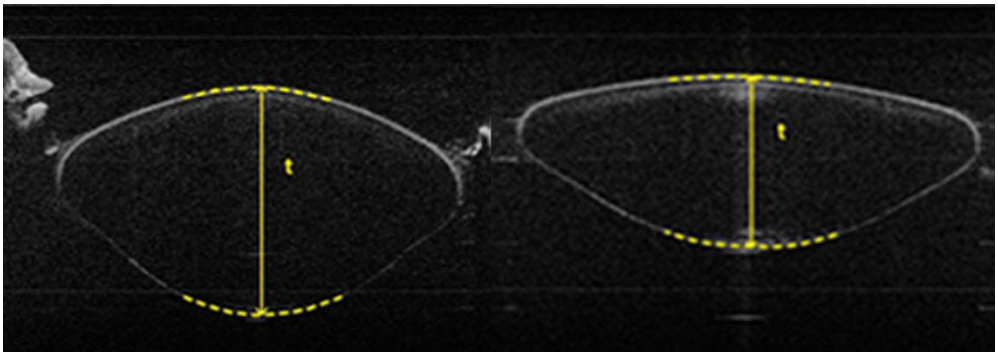


**Figure 3.3:** Sample OCT images of a lens during stretching experiments (3.25-year-old baboon). The images were scaled for refractive index but were not corrected for refractive distortion. The dashed lines show the spherical fit of the central 3-mm of the anterior and posterior surfaces. These images were used to measure lens thickness, *t*. The tissue is shown in the (Left) unstretched (accommodated) state, and (Right) stretched (unaccommodated) state. The radial displacement of the shoes in the stretched state was 2.5 mm. In this particular lens, the dimensions in the unstretched state were: Diameter: 8.07 mm; Thickness: 4.45 mm; Anterior radius: 4.29 mm; Posterior radius: 3.49 mm. The dimensions in the stretched state were: Diameter: 9.11 mm; Thickness: 3.32 mm; Anterior radius: 11.44 mm; Posterior radius: 5.16 mm. The figure also demonstrates the slight upward movement of the lens. The displacement of the lens posterior surface was measured and taken into account in the calculation of lens power (see text).

A paraxial optical model that takes into account the distance from the posterior lens surface to the window, the thickness of the window, and the distance from the window to the camera sensor was used to calculate the back vertex power of the lens. To quantify the intrinsic accuracy of the power measurements, the system was calibrated using a set of glass lenses of known optical power. The accuracy of the measurements was ±0.5 D. The error may be slightly higher in crystalline lenses due to their lower optical quality.

When tissue is mounted in the lens stretcher (unstretched state), the tension on the ciliary body and zonules is completely relaxed. The first and second stretching steps place the accommodative structures (zonules and ciliary body) under tension. During this stretching phase, the lens shifts slightly upward. In the subsequent steps, the posterior lens surface continues to move upward due to changes in the posterior lens shape. The slight upward movement of the lens is evident in Figure 3.3. Any translation of the lens or posterior lens surface that occurs during simulated accommodation is accounted for in the power calculations by measuring the displacement of the posterior surface of the lens. The displacement is added to the distance between the posterior surface of the lens and the window, $d_p$, obtained from a reference image acquired in the unstretched position (Figure 3.4).

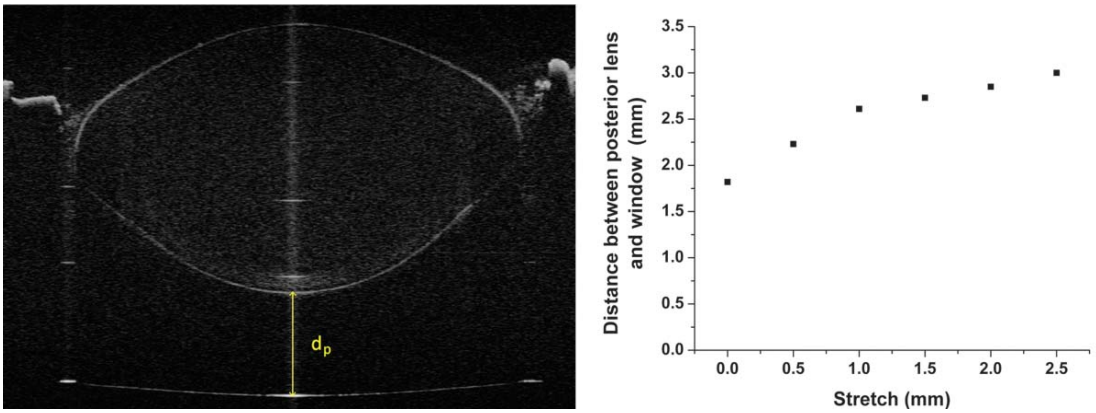


**Figure 3.4.** Compensation for the displacement of the lens posterior surface. (Left) Reference image of a 2.3-year-old baboon lens. The image is scaled for refractive index but is not corrected for refractive distortion. This image is used to measure the distance between the posterior surface of the lens and posterior window of the chamber, $d_p$, in the unstretched position. (Right) Change in the distance between the posterior lens surface and the window with respect to stretch (mm). The displacement of the lens posterior surface for this particular lens is roughly 1.2 mm.

### *3.3.6 Calculation of the surface and gradient contribution to lens power*

To allow for direct comparison with the back vertex power measured during stretching experiments, the contribution of the lens surfaces and gradient to back vertex power were calculated. The surface contribution was defined as the back vertex power of a thick spherical lens with radii of curvature and thickness equal to those of the crystalline lens and with a uniform refractive index equal to the index of the outer cortex (n = 1.365). With this definition, the total contribution of the surfaces, Ps, can be written as:

$$P_S = \frac{P_1}{\left(1 - \frac{t \cdot P_1}{n}\right)} + P_2 \qquad \text{(Eq. 3.1)}$$

where $P_1$ is the power of the anterior surface, $P_2$ is the power of the posterior surface, $t$ is the measured lens thickness and $n$ is the refractive index of the lens outer cortex (Jenkins & White, 1976). The first term on the right-hand side of Eq. (3.1) is the contribution of the anterior surface power and lens thickness to the back vertex power. The second term is the contribution of the posterior surface power to the back vertex power. The

contribution from the thickness term was minimal, corresponding to less than 3% of the anterior surface contribution for all lenses in this study. The change in thickness contributed to less than 0.01 D of the change in power during accommodation for all lenses.

To take into account the effect of spherical aberration, the individual surface powers $P_1$ and $P_2$ were calculated for an incident ray height corresponding to the conditions of the power measurement. For the anterior surface, the ray height was 1.5 mm. For the posterior surface, the ray height calculated by the ray tracing algorithm for the distortion correction was used. For each individual surface, the effective focal length at the corresponding ray height was determined using an exact ray-trace implemented in MATLAB. The power of the anterior and posterior surfaces, $P_1$ and $P_2$, were calculated by converting these focal lengths to dioptric power using a refractive index n=1.365 for the outer cortex and $n_o$=1.336 for the aqueous.

To calculate the contribution of the gradient within the lens, $P_g$, the combined calculated power of the anterior and posterior surfaces was subtracted from the measured back vertex power of the lens, $P_L$:

$$P_g = P_L - P_s \qquad \text{(Eq. 3.2)}$$

Note that the power is measured at 825 nm with a broadband source, while the surface contribution is calculated using the phase index at 589 nm. In theory, the measured power should be adjusted to take into account dispersion effects. However, an analysis using the dispersion model of Atchison & Smith (2005) shows that the difference in refractive index between the lens cortex and aqueous is approximately the same whether the phase

refractive index at 589 nm (Δn=0.0290) or the group refractive at 825 nm (Δn=0.0296) is used. The power measurements were therefore not adjusted for dispersion.

Since power measurements were acquired in separate runs from the curvature measurements, variations between runs may introduce errors in the calculated surface contributions. This error was estimated by quantifying the variability between power runs. The relative error was 2.0 ± 1.2% on average for all lenses in this study. The maximum relative error in the relative surface contribution was 4.0% on average.

### *3.3.7 Data analysis*

The contributions of the lens anterior surface, posterior surface and gradient to the total lens power were calculated for all lenses at each stretching step using Eqs (3.1-3.2). The contribution of the surfaces and gradient to the accommodation amplitude were quantified by plotting the individual contributions as a function of total lens power during stretching. The age-dependence of the contributions was analyzed.

## 3.4 Results

### *3.4.1 General behaviors*

In all lenses, except the 28 year-old (oldest) baboon lens, the anterior and posterior surfaces flattened and total lens power decreased as the lens was stretched, as expected from the Helmholtz theory of accommodation (Figure 3.5). In the oldest baboon lens, there was no significant change in lens shape during stretching experiments. Therefore, the analysis for this lens is limited to the unstretched state.

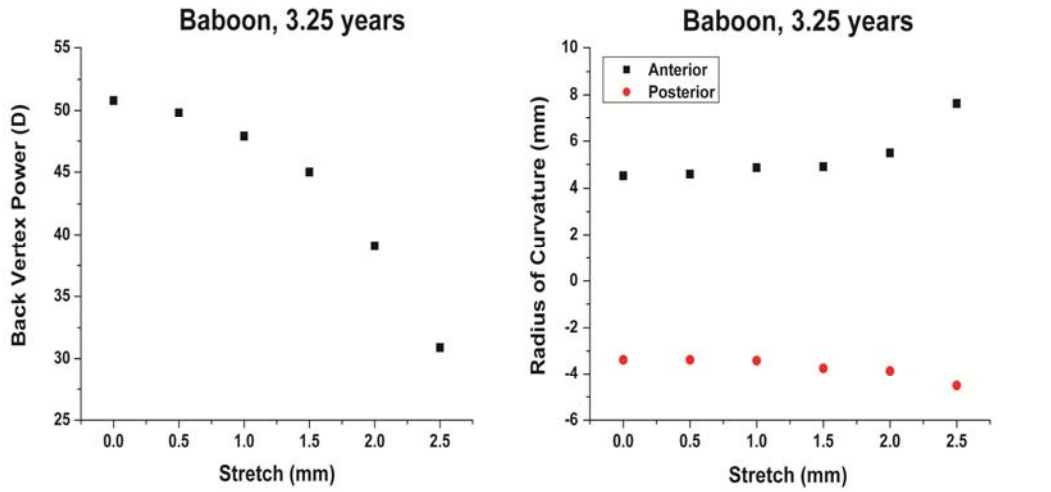


**Figure 3.5:** (Left) Typical plot of lens back vertex power (D) with respect to stretch (mm). The power decreases as the lens is stretched from an accommodated state to an unaccommodated state. (Right) Typical plot of anterior and posterior lens radius of curvature (mm) with respect to stretch (mm). The posterior radii of curvature are negative due to the orientation of the lens surface. The anterior and posterior surfaces of the lens flatten as the lens is stretched.

### *3.4.2 Lens surface and gradient power vs. age*

As reported in previous studies (Borja et al., 2008; Borja, Manns et al., 2010; Jones et al., 2005), the total power of the lens in the unstretched (accommodated) state decreases with age (Figure 3.6). The power of the gradient decreases with age in both species ($p<0.001$ for monkeys, $p<0.001$ for baboons). The power of the anterior and posterior lens surfaces also slightly decreases with age ($p<0.001$ for monkeys, $p<0.001$ for baboons). The total power, surface contribution, and gradient contribution of the monkey lenses are higher than those of the baboon lenses. The power data is shown in Tables 3.1 and 3.2.

| Baboon | Age (years) | Unstretched Lens Back Vertex Power (D) | Anterior Surface Unstretched Power (D) | Posterior Surface Unstretched Power (D) | Gradient Unstretched Power (D) | Anterior Surface Slope (D/D) | Posterior Surface Slope (D/D) | Gradient Slope (D/D) |
|---|---|---|---|---|---|---|---|---|
| 1 OS | 1.80 | 59.0 | 6.9 | 7.7 | 44.4 | 0.187 | 0.122 | 0.719 |
| 2 OD | 2.30 | 59.0 | 7.4 | 9.6 | 41.9 | 0.154 | 0.128 | 0.717 |
| 3 OD | 2.30 | 54.5 | 8.5 | 9.9 | 36.1 | 0.220 | 0.168 | 0.611 |
| 4 OD | 3.00 | 47.6 | 7.3 | 9.2 | 31.1 | 0.258 | 0.225 | 0.514 |
| 5 OD | 3.25 | 49.3 | 7.1 | 9.1 | 33.0 | 0.189 | 0.143 | 0.632 |
| 5 OS | 3.25 | 50.8 | 7.0 | 9.4 | 34.4 | 0.147 | 0.134 | 0.718 |
| 6 OS | 3.67 | 49.1 | 7.4 | 9.1 | 32.7 | 0.207 | 0.155 | 0.639 |
| 7 OD | 5.42 | 47.3 | 7.4 | 9.3 | 30.6 | 0.218 | 0.173 | 0.607 |
| 7 OS | 5.42 | 46.6 | 7.9 | 8.7 | 30.1 | 0.227 | 0.136 | 0.639 |
| 8 OD | 6.92 | 47.1 | 7.0 | 9.0 | 31.1 | 0.190 | 0.094 | 0.715 |
| 8 OS | 6.92 | 45.9 | 6.8 | 8.4 | 30.7 | 0.223 | 0.159 | 0.618 |
| 9 OD | 7.42 | 41.6 | 6.2 | 7.9 | 27.6 | 0.241 | 0.121 | 0.639 |
| 10 OD | 7.83 | 46.3 | 7.7 | 8.5 | 30.1 | 0.206 | 0.130 | 0.666 |
| 10 OS | 7.83 | 44.8 | 7.7 | 9.0 | 28.2 | 0.134 | 0.104 | 0.762 |
| 11 OD | 8.30 | 44.9 | 6.4 | 8.8 | 29.7 | 0.176 | 0.168 | 0.651 |
| 12 OD | 8.33 | 44.4 | 7.0 | 8.3 | 29.1 | 0.222 | 0.138 | 0.634 |
| 12 OS | 8.33 | 46.3 | 7.1 | 8.6 | 30.6 | 0.185 | 0.115 | 0.677 |
| 13 OD | 9.60 | 44.4 | 6.8 | 7.8 | 29.8 | 0.160 | 0.124 | 0.696 |
| 14 OD | 12.10 | 37.6 | 6.2 | 7.3 | 24.1 | 0.281 | 0.123 | 0.588 |
| 15 OS | 14.00 | 41.7 | 5.6 | 8.0 | 28.1 | 0.159 | 0.107 | 0.734 |
| 16 OD | 21.00 | 34.7 | 4.7 | 6.8 | 23.2 | 0.246 | 0.190 | 0.572 |
| 16 OS | 21.00 | 32.9 | 3.9 | 6.4 | 22.6 | 0.221 | 0.106 | 0.670 |
| 17 OD | 21.00 | 30.2 | 4.3 | 7.0 | 18.9 | 0.207 | 0.168 | 0.625 |
| 18OD | 24.66 | 25.2 | 3.8 | 6.2 | 15.3 | 0.240 | 0.185 | 0.590 |
| 19 OS | 28.00 | 27.4 | 2.7 | 5.9 | 18.8 | NA | NA | NA |

**Table 3.1:** Hamadryas baboon results. Measured lens back vertex power, anterior surface, posterior surface and gradient power in the unstretched state, and the anterior surface, posterior surface and gradient contributions to accommodation amplitude (in D/D).

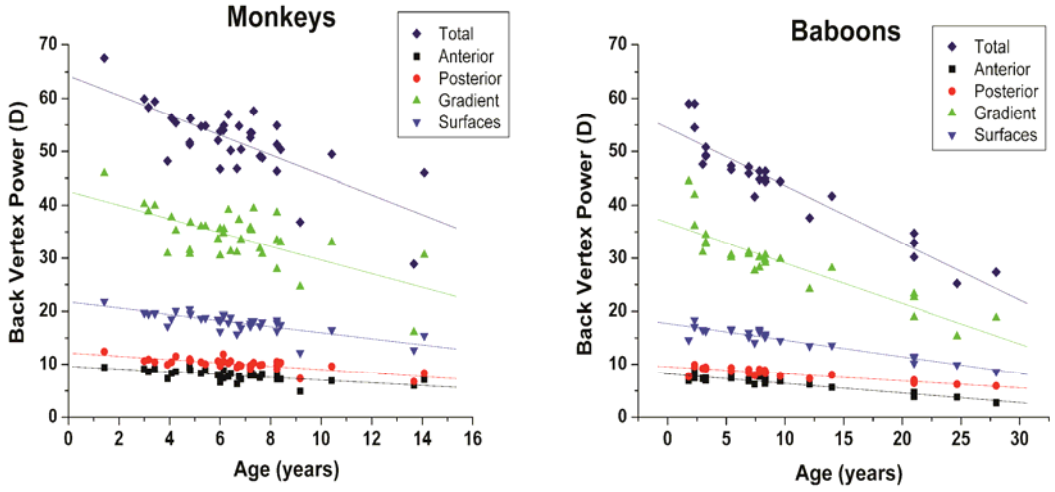


**Figure 3.6:** Unstretched lens power as a function of age for (Left) cynomolgus monkeys and (Right) hamadryas baboons. The lens back vertex power and contributions of the lens anterior surface, posterior surface, combined surfaces and gradient are shown.

| Monkey | Age (years) | Unstretched Lens Back Vertex Power (D) | Anterior Surface Unstretched Power (D) | Posterior Surface Unstretched Power (D) | Gradient Unstretched Power (D) | Anterior Surface Slope (D/D) | Posterior Surface Slope (D/D) | Gradient Slope (D/D) |
|---|---|---|---|---|---|---|---|---|
| 1 OD | 1.42 | 67.6 | 9.4 | 12.4 | 45.9 | 0.168 | 0.168 | 0.668 |
| 2 OD | 3.00 | 59.9 | 9.1 | 10.6 | 40.2 | 0.192 | 0.138 | 0.672 |
| 3 OD | 3.17 | 58.3 | 8.6 | 10.9 | 38.8 | 0.194 | 0.169 | 0.636 |
| 4 OD | 3.42 | 59.4 | 9.1 | 10.4 | 39.9 | 0.221 | 0.126 | 0.651 |
| 5 OD | 3.92 | 48.2 | 7.3 | 9.9 | 30.9 | 0.215 | 0.183 | 0.598 |
| 6 OD | 4.08 | 56.3 | 8.3 | 10.4 | 37.7 | 0.207 | 0.138 | 0.652 |
| 7 OD | 4.25 | 55.4 | 8.6 | 11.5 | 35.2 | 0.214 | 0.182 | 0.599 |
| 8 OD | 4.80 | 51.3 | 9.7 | 10.7 | 30.8 | 0.225 | 0.169 | 0.605 |
| 8 OS | 4.80 | 51.7 | 9.3 | 11.0 | 31.5 | 0.245 | 0.160 | 0.596 |
| 9 OD | 4.83 | 56.2 | 8.8 | 10.7 | 36.7 | 0.195 | 0.143 | 0.664 |
| 10 OS | 5.25 | 54.7 | 8.3 | 10.4 | 36.0 | 0.212 | 0.191 | 0.597 |
| 11 OD | 5.42 | 54.8 | 8.8 | 10.0 | 36.0 | 0.229 | 0.158 | 0.613 |
| 12 OD | 5.92 | 52.1 | 8.0 | 10.6 | 33.6 | 0.198 | 0.178 | 0.624 |
| 13 OS | 6.00 | 53.8 | 7.8 | 10.4 | 35.6 | 0.216 | 0.159 | 0.624 |
| 14 OD | 6.00 | 46.7 | 6.6 | 9.7 | 30.5 | 0.205 | 0.204 | 0.592 |
| 15 OS | 6.13 | 54.0 | 7.4 | 11.9 | 34.7 | 0.181 | 0.197 | 0.618 |
| 16 OD | 6.15 | 54.9 | 8.8 | 10.5 | 35.5 | 0.217 | 0.143 | 0.637 |
| 17 OS | 6.33 | 57.0 | 7.7 | 10.2 | 39.1 | 0.145 | 0.136 | 0.716 |
| 18 OS | 6.42 | 50.2 | 8.3 | 10.6 | 31.3 | 0.244 | 0.220 | 0.536 |
| 19 OD | 6.67 | 46.8 | 6.3 | 9.4 | 31.1 | 0.217 | 0.209 | 0.572 |
| 20 OD | 6.75 | 54.8 | 7.7 | 9.9 | 37.2 | 0.169 | 0.152 | 0.681 |
| 21 OD | 6.83 | 50.4 | 7.2 | 9.7 | 33.5 | 0.192 | 0.177 | 0.633 |
| 22 OS | 7.20 | 53.5 | 7.93 | 9.72 | 35.8 | 0.215 | 0.146 | 0.640 |
| 22 OD | 7.20 | 52.6 | 8.2 | 9.1 | 35.4 | 0.168 | 0.136 | 0.697 |
| 23 OD | 7.25 | 53.5 | 8.3 | 9.9 | 35.3 | 0.202 | 0.150 | 0.643 |
| 24 OS | 7.33 | 57.6 | 7.9 | 10.3 | 39.4 | 0.184 | 0.154 | 0.663 |
| 25 OD | 7.58 | 49.1 | 7.5 | 9.8 | 31.8 | 0.215 | 0.149 | 0.636 |
| 26 OD | 7.67 | 48.8 | 8.1 | 9.9 | 30.8 | 0.232 | 0.174 | 0.587 |
| 27 OD | 8.25 | 46.3 | 7.9 | 10.5 | 27.9 | 0.235 | 0.199 | 0.564 |
| 28 OD | 8.25 | 51.3 | 8.0 | 9.8 | 33.4 | 0.171 | 0.138 | 0.698 |
| 29 OD | 8.25 | 54.9 | 7.2 | 9.1 | 38.6 | 0.164 | 0.141 | 0.695 |
| 30 OD | 8.40 | 50.4 | 7.2 | 10.3 | 33.0 | 0.201 | 0.176 | 0.628 |
| 31 OD | 9.17 | 36.8 | 4.9 | 7.3 | 24.6 | 0.178 | 0.161 | 0.657 |
| 32 OD | 10.42 | 49.5 | 6.9 | 9.6 | 33.0 | 0.166 | 0.168 | 0.668 |
| 33 OD | 13.67 | 28.9 | 6.0 | 6.7 | 16.1 | 0.351 | 0.211 | 0.436 |
| 34 OS | 14.08 | 46.0 | 7.1 | 8.3 | 30.6 | 0.185 | 0.176 | 0.639 |

**Table 3.2:** Cynomolgus monkey results. Measured lens back vertex power, anterior surface, posterior surface and gradient power in the unstretched state, and the anterior surface, posterior surface and gradient contributions to accommodation amplitude (in D/D).

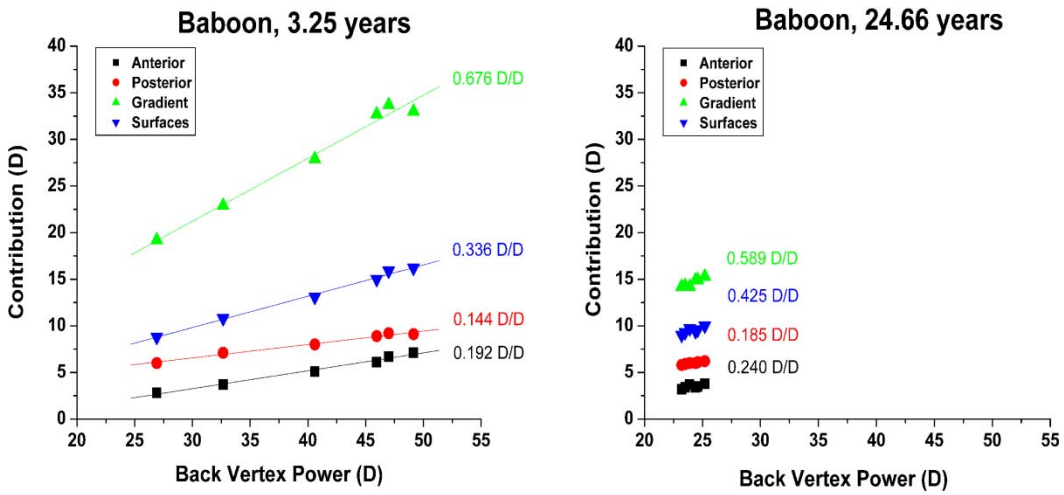


**Figure 3.7:** Typical example of the contribution of the lens anterior surface, posterior surface, combined surfaces and gradient to lens back vertex power during simulated accommodation for (Left) a young baboon and (Right) an older baboon. For young baboons (age<14 years), the $R^2$ values ranged from 0.82 to >0.99 for the anterior surface, 0.84 to >0.99 for the posterior surface, 0.83 to >0.99 for the combined surfaces and 0.93 to >0.99 for the gradient. For the older baboons (age>20 years), the $R^2$ values ranged from 0.81 to 0.93 for the anterior surface, 0.92 to >0.99 for the posterior surface, 0.86 to 0.96 for the combined surfaces and 0.89 to >0.99 for the gradient. For the monkeys, the $R^2$ values ranged from 0.98 to >0.99 for the anterior surface, 0.90 to >0.99 for the posterior surface, 0.94 to >0.99 for the combined surfaces and >0.993 for the gradient.

### *3.4.3 Lens surface and gradient contribution vs. accommodation*

The power of the lens surfaces and gradient decrease linearly as the total lens power decreases during stretching (disaccommodation) (Figure 3.7). The rate of change was quantified by performing a linear regression of the anterior surface, posterior surface, combined surfaces, and gradient contributions. The slope of the linear regression provides the contribution of the surfaces or gradient to the accommodation amplitude. The changes in lens power observed during stretching were significantly reduced in the older baboon lenses (Figure 3.7, Right)

### *3.4.4 Surface and gradient contribution to accommodation amplitude*

In all lenses, the contribution of the anterior surface to accommodation amplitude was larger than that of the posterior surface, and the contribution of the gradient was

larger than the combined contribution of the surfaces (Figure 3.8). The contribution of the anterior surface to the accommodation amplitude ranged from 0.14 D/D to 0.35 D/D for the cynomolgus monkeys and 0.13 D/D to 0.28 D/D for the hamadryas baboons. The contribution of the posterior surface to the accommodation amplitude ranged from 0.13 D/D to 0.22 D/D for the cynomolgus monkeys and 0.09 D/D to 0.23 D/D for the hamadryas baboons. The contribution of the gradient remains constant with age in both species ($p=0.16$ for monkeys, $p=0.35$ for baboons), with a range from 0.44 D/D to 0.68 D/D for cynomolgus monkeys and from 0.51 D/D to 0.76 D/D for hamadryas baboons. There is no major difference between cynomolgus monkeys and hamadryas baboons in the contributions of the surfaces or gradient to accommodation amplitude.

### *3.4.5 Relative contributions of the surfaces and gradient to lens power*

During stretching (disaccommodation), the relative contribution (in % of the lens back vertex power) of the anterior lens surface decreases and the relative contribution of the posterior lens surface increases (Figure 3.9). The decrease in relative contribution of the anterior surface of the lens is consistent with the fact that the anterior surface of the lens flattens more than the posterior surface during disaccommodation (Dubbelman & Van der Heijde, 2001; Dubbelman, Van der Heijde, & Weeber, 2005; Koretz, Cook, & Kaufman, 1997). A regression analysis showed that the contribution of the gradient was constant in 28 monkey lenses and 21 baboon lenses ($p>0.05$). There was a significant change in the relative contribution of the gradient in 8 monkey lenses and 4 baboon lenses; however, this change was always less than 6%.

Since the relative contributions of the gradient and combined surfaces to the lens power are independent of the accommodative state, the unstretched (accommodated) state was used to illustrate the changes with age for all the primates in this study. The relative contribution of the gradient remains constant with age in both species (Figure 3.10). The contributions of the anterior surface, posterior surface and gradient to the lens back vertex power ranged from 13 to 20%, 17 to 23% and 56 to 70% for the cynomolgus monkeys and from 10 to 17%, 13 to 24% and 60 to 75% for the hamadryas baboons. The relative contributions are similar in cynomolgus monkeys and hamadryas baboons.

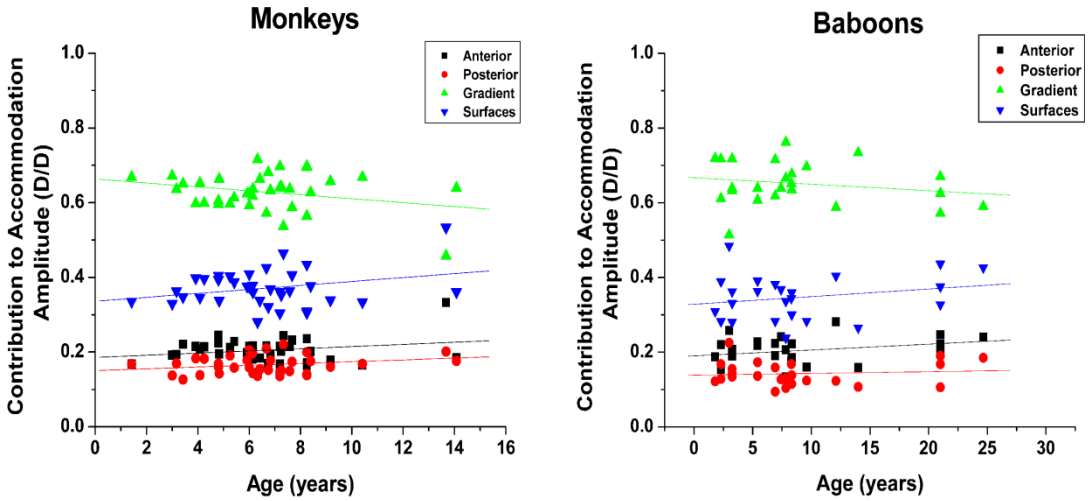


**Figure 3.8:** The contributions calculated for the lens anterior surface, posterior surface, combined surfaces, and gradient contribution with respect to accommodation amplitude plotted as a function of age for cynomolgus monkeys (left) and hamadryas baboons (right).

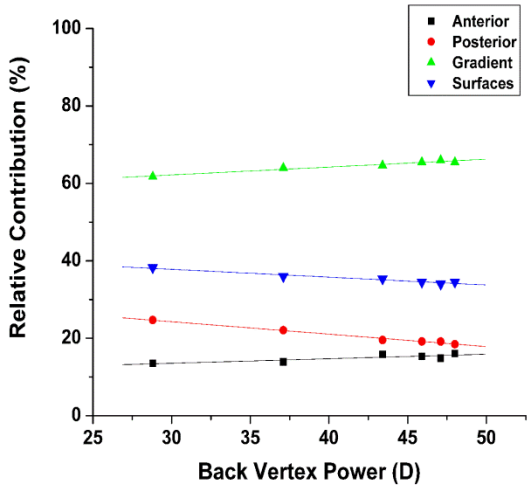


**Figure 3.9:** Example of the relative contribution (%) of the lens anterior surface, posterior surface, combined surfaces and gradient to back vertex power of the lens during simulated accommodation (Baboon, Age 6.92 years). In this lens, there is a statistically significant change in the relative contribution of the gradient during accommodation, from 62% to 66%. The relative contribution of the anterior surface decreases and the relative contribution of the posterior surface increases with accommodation. In the majority of lenses (28 monkey and 21 baboon), the relative contribution of the gradient remained constant.

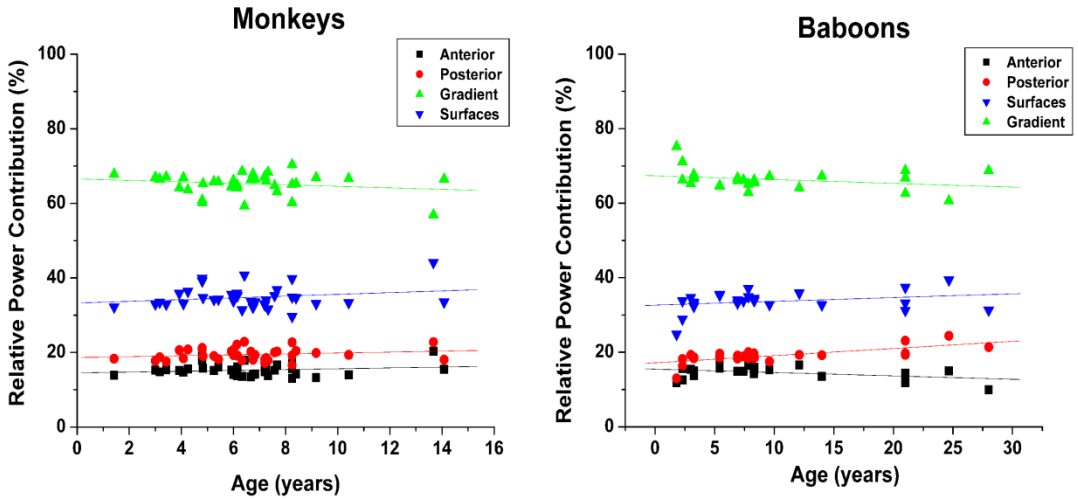


**Figure 3.10:** The relative contributions of the anterior surface, posterior surface, combined surfaces and gradient to the lens back vertex power in the unstretched (accommodated state) plotted as a function of age for (Left) cynomolgus monkeys and (Right) hamadryas baboons. The relative contribution of the gradient remains constant (Monkeys: p=0.28, average 65±3%; Baboons: p=0.19, average 66±3%).

## 3.5 Discussion

The aim of this study was to determine the contribution of the lens gradient refractive index to the change in lens back vertex power during simulated accommodation in primate lenses. The main findings of the study were:

- The power, in D, of the lens surfaces and gradient linearly increases with increasing lens power during accommodation
- The contribution, in D/D, of the anterior lens surface to the accommodation amplitude is greater than the contribution of the posterior surface for all lenses
- The gradient contributes significantly to the accommodation amplitude, corresponding on average to 65% for cynomolgus monkeys and 66% for hamadryas baboons
- The lens back vertex power and the power of the surfaces and gradient decrease with age
- The relative contribution of the gradient to the accommodative amplitude remains constant with age

Clearly, the calculated gradient contribution depends on the value of the outer cortex refractive index. An outer cortex refractive index of 1.365 was used, derived from measurements of protein concentrations (Pierscionek, Smith, & Augusteyn, 1987; Moffat et al., 2002). This value is also the median of published data, which ranges from 1.34 to 1.39 (Nakao, Ono, Nagata, & Iwata, 1969; Pomerantzeff, Pankratov, Wang, & Dufault, 1984; Pierscionek & Chan, 1989; Moffat, Atchison, & Pope, 2002; Jones et al., 2005). In any case, independent of the refractive index value selected within this range, the main conclusion that the gradient contributes to the accommodative power of the lens remains valid. In the extreme cases, n=1.34 results in a gradient power contribution of 94% and n=1.39 results in a gradient power contribution of 21%.

These results are comparable to the *in vivo* human results of Dubbelman, Van der Heijde, & Weeber (2005), which measured the changes in lens shape in response to an

accommodative stimulus. Dubbleman et al. (2005) found a curvature change of 6.7 $mm^{-1}$/D for the anterior surface and 3.7 $mm^{-1}$/D for the posterior surface, which corresponds to power changes of 0.19 D/D for the anterior surface and 0.11 D/D for the posterior surface assuming a surface refractive index of 1.365. The combined contribution of the surfaces is therefore 30%, which is comparable to our findings (~34%). Furthermore, the results were compared with those obtained *in vivo* with Rhesus monkeys by Rosales, Wendt, Marcos, & Glasser (2008). For this comparison, a linear fit was performed on their average anterior and posterior lens curvatures (Ra=11.11 mm - 6.4 mm/D; Rp=-6.64 mm + 0.17 mm/D) and the methods from our study was used to calculate the surface contributions. The resulting contributions were 18.2% for the anterior surface and 14.5% for the posterior surface, which gives a combined surface contribution of 32.7%. This is also in good agreement with our data and the human results of Dubbelman. In addition, our finding that the gradient power (D) decreases with age is in agreement with in vitro and *in vivo* studies on human, cynomolgus, rhesus and baboon lenses (Borja et al., 2008; Borja, Manns et al., 2010; Dubbelman & Van der Heijde, 2001; Jones et al., 2005). These studies show that this decrease in the gradient power is the main contribution to the loss of power in isolated lenses with age.

To further compare the results with previous studies, which quantified the power of the internal structure of the lens using an equivalent refractive index, the relation between the power of the gradient and the equivalent refractive index was determined. To simplify the analysis a thin lens model was used. With some arithmetic manipulation, one can show that the relation between equivalent refractive index and power of the gradient is:

$$n_{eq} = n_o + (n - n_o)\frac{1}{1 - \frac{P_g}{P}} \qquad \text{(Eq. 3.3)}$$

where $n_o$=1.336 is the refractive index of the aqueous, n=1.365 is the refractive index of lens outer cortex, P is the lens power, and $P_g$ is the contribution of the gradient. Eq. (3.3) shows that equivalent refractive index is a measure of the relative contribution of the gradient to the total lens power (ratio $P_g$/P). The finding, that the relative contribution of the gradient remains constant with accommodation, is therefore in agreement with previous studies, which found that the equivalent refractive index of the lens does not change with accommodation (Garner & Smith, 1997; Hermans et al., 2008).

The finding that the gradient contributes significantly to the accommodation amplitude is consistent with Gullstrand's intracapsular theory of accommodation and the previous observation by Garner & Smith (1997) based on a gradient model of the lens. Gullstrand used a higher value for the equivalent refractive index for his schematic lens in the accommodated state to take into account the contribution of the gradient. Our results, together with the simplified model of Eq. (3.3), show that a constant value for the equivalent index with accommodation can be assumed since the relative contribution of the gradient remains constant.

The observation that the relative contribution of the gradient remains constant with age is consistent with the results of a previous study on isolated cynomolgus and rhesus monkey lenses (Borja, Manns et al., 2010), where the gradient contribution was found to be 62% on average for cynomolgus monkeys. The values in the present study are slightly higher (65%) mainly because of differences in the value for the cortex refractive index (1.371 versus 1.365) and different methodology to calculate the lens

power (effective power versus back vertex power). On the other hand, the previous study found a decrease in the relative contribution of the gradient with age in baboon lenses. However, the study only had two older baboon lenses (above 20 years) and had a smaller sample size. With the additional data and broader age range, the present study shows that the relative gradient contribution is constant with age.

Age-related changes in gradient power (D) seem to be primarily due to changes in the axial refractive index profile of the lens (Augusteyn, Jones, & Pope, 2008; Augusteyn, 2010; Jones et al., 2005). On the other hand, the fact that the relative contribution of the gradient remains constant with accommodation suggests that the changes in gradient power with accommodation are not due to changes in the axial distribution, but rather to changes of the iso-indicial curvatures with accommodation. This observation is consistent with *in vivo* MRI studies showing that the axial gradient profile changes much less with accommodation than with age (Kasthurirangan et al., 2008).

In all lenses, only a small change in posterior lens curvature during accommodation was observed, consistent with previous *in vivo* studies on human and rhesus monkey lenses (Brown, 1974; Koretz, Handelman, & Brown, 1984; Koretz, Bertasso, Neider, True-Gabel, & Kaufman, 1987; Dubbelman, Van der Heijde, & Weeber, 2005). However, there is always some uncertainty in the measurement of the posterior lens curvature because the posterior lens is imaged through the anterior surface and gradient (Borja et al., 2008, Dubbelman & Van der Heijde, 2001). In the present study, there are two potential sources of error. First, the OCT images were scaled by dividing the optical path length by an estimate of the group refractive index based on

previous measurements (Uhlhorn et al., 2008). Second, the OCT images were corrected for distortions due to refraction assuming a uniform refractive index equal to the average index of the lens. An analysis was performed to determine how the value of the group refractive index used to scale the lens and correct posterior distortions affects the posterior lens power. For average group refractive indices ranging from 1.39 to 1.42 (Uhlhorn et al., 2008), a variation of less than 0.5 D (5%) for the posterior lens surface power was found. Therefore, the uncertainty on the value of the average refractive index has only a minimal effect on the final results.

### 3.6 Summary

The purpose of this aim was to determine the contribution of the lens gradient refractive index to the change in lens back vertex power with accommodation. A lens stretching system was used to perform simulated accommodation experiments. The changes in lens optical power, thickness and shape were quantified to determine the contribution of the gradient refractive index to the accommodative amplitude.

The gradient was found to contribute on average 65±3% of the total lens power change during accommodation for cynomolgus monkeys and 66±3% for hamadryas baboons, assuming an outer cortex refractive index of 1.365. The relative contribution of the gradient (or equivalent refractive index) remains constant with accommodation. These findings show that accommodation-dependent optical models of the lens can assume a constant equivalent refractive index. They also suggest that a material of uniform refractive index could serve as a lens substitute for lens refilling procedures to restore accommodation (Kessler, 1964; Koopmans, Terwee, Barkhof, Haitjema, &

Kooijman, 2003; Nishi, Mireskandari, Khaw, & Findl, 2009; Parel, Gelender, Trefers, & Norton, 1986).

# CHAPTER 4

# MEASUREMENT OF CRYSTALLINE LENS SPHERICAL ABERRATION USING LASER RAY TRACING[2]

## 4.1 Purpose

Accommodative changes in crystalline lens aberrations are of special interest because they impact retinal image quality and are factors in determining the best focus position of the eye. Changes in ocular aberrations with accommodation may also play a role in refractive error development. This chapter describes the development of a new laser ray tracing method which uses a camera mounted on a vertical positioning stage to directly measure changes in lens spherical aberration. The purpose of this aim is to quantify the accommodative changes in lens power and spherical aberration using laser ray tracing.

## 4.2 Background

Changes in the shape of the lens with accommodation produce changes in the aberrations of the lens and the whole eye (Ivanoff, 1956; Jenkins, 1963; He, Burns, Marcos, 2000; Vilupuru, Roorda, Glasser, 2004). Studies in human and non-human primates (NHPs) have shown that the spherical aberration of the eye shifts toward more negative values with accommodation (Ivanoff, 1956; Jenkins, 1963; He, Burns, Marcos, 2000; Vilupuru, Roorda, Glasser, 2004; Koomen, Tousey, Scolnik, 1949; Atchison et al., 1995; Glasser & Campbell, 1998; Roorda & Glasser, 2004; Gambra, Sawides, Dorronsoro, Marcos, 2009; Cheng et al., 2004). It is difficult to obtain direct *in vivo*

[2] The content in this chapter was published in:
Maceo Heilman B, Manns F, de Castro A, Durkee H, Arrieta E, Marcos S, Parel J-M. (2015) Changes in Monkey Crystalline Lens Spherical Aberration during Simulated Accommodation in a Lens Stretcher. *Investigative Ophthalmology & Visual Science*, 56(3):1743-1750.

spherical aberration measurements of the crystalline lens due to its position behind the cornea and iris.

The aberrations of the lens can be estimated by measuring whole-eye aberrations and subtracting the aberrations of the anterior and posterior corneal surfaces (El Hage & Berny, 1973; Artal, Berrio, Guirao, Piers, 2002) In a study by Smith et al. (2001) the spherical aberration of *in vivo* human lenses was predicted by measuring the aberrations of the whole eye and subtracting those of the anterior corneal surface, based on the measured anterior corneal radius of curvature and asphericity, and the predicted posterior corneal surface, based on the estimated posterior corneal radius of curvature and asphericity. The mean spherical aberration of the lens was found to be negative over a wide range of possible posterior corneal surface values. With the availability of commercial devices that measure the posterior corneal surface, it is now possible to calculate *in vivo* lens spherical aberration more accurately, using ocular biometry and aberrometry combined with optical modeling.

Changes in the aberrations of the crystalline lens with accommodation are of considerable interest because they impact retinal image quality and are factors in determining the best focus position of the eye. The accommodation-induced changes in ocular aberrations may also play a role in the development of refractive error and in determining the optical accommodative response (Charman & Tucker, 1977; Walsh & Charman, 1989; Wilson, Decker & Roorda, 2002; Whatman et al., 2009; Thibos, Bradley, Liu, Lopez-Gil, 2013).

Simulations based on a reconstructed gradient refractive index (GRIN) have been used to predict spherical aberration in *ex vivo* lenses and its changes with accommodation

(de Castro et al., 2013). In the study, the lens shape and GRIN were reconstructed from optical coherence tomography (OCT) images (de Castro et al., 2010; Birkenfeld et al., 2013). A numerical ray trace was performed through the reconstructed lens to predict the spherical aberration. Similar to previous findings, the study found that the lens spherical aberration becomes more negative with accommodation.

In this chapter, a direct technique was used to measure the changes in lens spherical aberration with accommodation in cynomolgus monkey lenses, using measurements based on LRT. Combining OCT with LRT allows for the direct measurement of lens spherical aberration during simulated accommodation in a lens stretcher. The measurements from this study were in good agreement with the results obtained from numerical ray tracing based on a model of the reconstructed lens (de Castro et al., 2013) and serves to validate the GRIN reconstruction technique.

## 4.3 Laser ray tracing overview

### *4.3.1 Rationale for improving method*

Laser ray tracing is a technique that uses a laser scanner to deliver narrow parallel beams of light sequentially through a lens to measure the lens aberrations (Navarro & Losada, 1997; Navarro & Moreno-Barriuso, 1999; Marcos, 2006). Sivak & Kreuzer (1983) measured spherical aberration in excised lenses for a variety of species including dogs, rabbits, frogs, cows and humans. The isolated lenses were suspended using a thin wire and submerged in a tank filled with saline. A helium-neon (HeNe) laser was used to deliver multiple laser beams through the lens and photographs of the side of the tank were taken to determine the ray slopes. The beams were made more visible by adding 2-3

drops of milk to the tank. Figure 4.1 shows multiple laser beams rays passing through an isolated human lens (78 years old).

Previous studies have also measured changes in lens spherical aberration with accommodation, but these had their limitations. Glasser and Campbell (1998) measured the longitudinal spherical aberration of 27 human lenses in a lens stretcher using an LRT system. The lenses were placed in a tank filled with saline and a HeNe laser delivered multiple beams along the lens. Drops of paint were added to scatter the light, and a side-facing camera was used to capture images of the beams projected along the lens. Their results showed that lens spherical aberration becomes more negative with accommodation and more positive with age. However, this photographic LRT technique is subject to measurement uncertainty because it is difficult to quantify the path of the rays in the paraxial region. This is challenging to determine the paraxial focal length of the lens and therefore to quantify the spherical aberration with high precision. In a more recent study by Roorda and Glasser (2004), the technique was refined to produce a three-dimensional wavefront measurement of the lens by using two cameras and measurements of the wavefront slopes rather than the intersections of the rays along the optical axis. However, lens spherical aberration data were reported only for one macaque monkey lens.

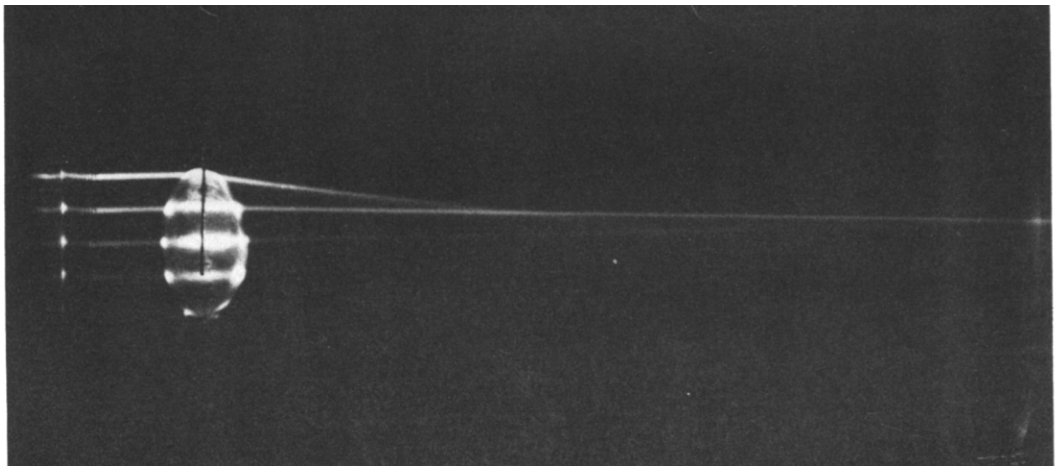

**Figure 4.1:** Photograph of multiple laser beams passing through an isolated human lens (78 years) suspended in a tank. The lens is suspended using a thin wire and submerged in a tank filled with saline (Sivak & Kreuzer, 1983).

### *4.3.2 System Description*

The laser ray tracing system was incorporated with the second generation *Ex Vivo* Accommodation Simulator (EVAS II) using the system's existing instrumentation. A ray trace was performed by synchronizing the time-domain OCT and EVAS II computers. The OCT and EVAS II systems were described in detail in Chapter 3. During an LRT experiment, the OCT scanners move to a specified position and a trigger is sent to the EVAS II computer when the position of the beam has changed. The LRT system delivers equally-spaced parallel rays sequentially along the vertical meridian of the lens. A camera module (Panasonic, GP-CX261V) mounted on a vertical positioning stage below the tissue chamber was used to record the spots corresponding to each individual ray (Figure 4.2).

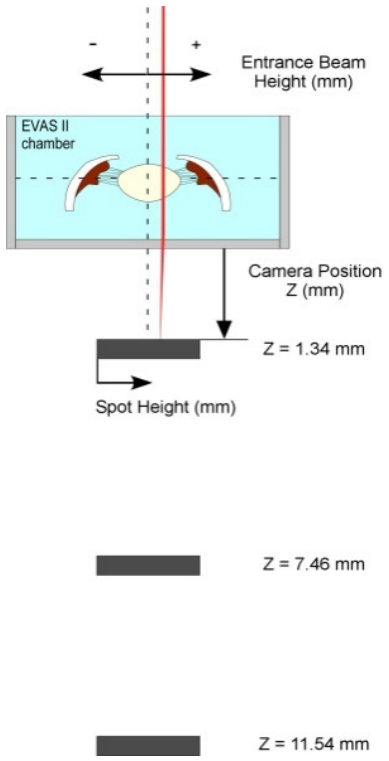


**Figure 4.2:** Schematic of the LRT beam delivery onto a crystalline lens mounted in the EVAS II tissue chamber. The position of the camera is measured as a distance *z* (mm) below the tissue chamber.

### *4.3.3 Calculation of lens power*

A program written in MATLAB (Mathworks, Natick, MA, USA) was used to calculate the centroid of each spot for all of the images. The centroid position was used as an estimate for the ray height, *y*, incident on the camera. The measured spot heights were plotted as a function of entrance ray height. A plot was generated for each axial position of the camera. Figure 4.3 shows the measured ray heights plotted as a function of entrance ray height for a typical cynomolgus monkey lens. These graphs were generated for each axial position, *z*, of the camera and fit with a third-order polynomial:

$$y(z) = y_0 + B(z) \times (h - h_0) + D(z) \times (h - h_0)^3 \qquad \text{(Eq. 4.1)}$$

where $y_0$ is a constant term [mm], *B(z)* is a measure of the paraxial ray path, *D(z)* is a measure of the lens third-order spherical aberration [$mm^{-2}$], *h* is the entrance ray height

[mm], and $h_0$ is an offset that accounts for lens decentration relative to the input ray-trace [mm]. Since the rays travel in a straight line, *B(z)* and *D(z)* are linear functions in terms of axial position, *z*, expressed by:

$$B(z) = B_0 + m_B \cdot z \qquad \text{(Eq. 4.2)}$$

$$D(z) = D_0 + m_D \cdot z \qquad \text{(Eq. 4.3)}$$

where $B_0$ and $D_0$ [$mm^{-2}$] are constant terms, $m_B$ [$mm^{-1}$] and $m_D$ [$mm^{-3}$] are the slopes of the linear fits and *z* is the position of the camera [mm]. To simplify the description, we assume $h_0 = 0$, since $h_0$ is a term included to take into account lateral offset in the experiment. The slope and intercept of *B(z)* and *D(z)* are determined by performing a linear fit versus *z* (Figure 4.4).

In paraxial approximation, the spherical aberration of the lens is zero, *D(z)* = 0, which gives:

$$y(z) = y_0 + (B_0 + m_B \cdot z) \cdot h \qquad \text{(Eq.4.4)}$$

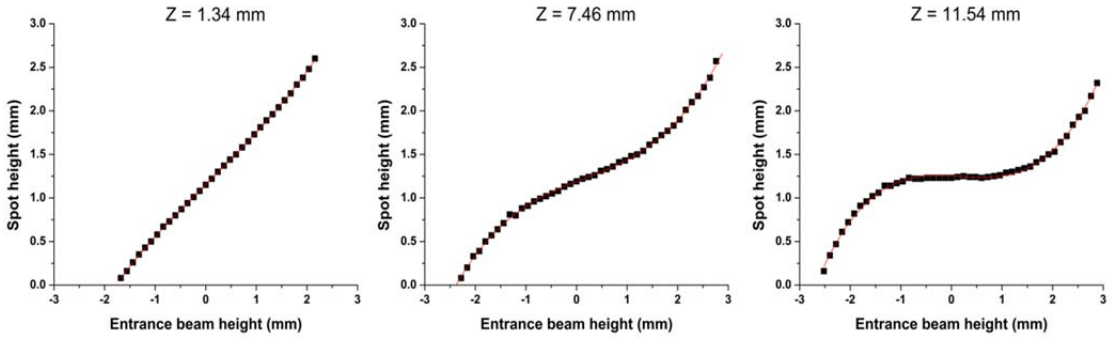


**Figure 4.3:** Spot heights on the camera (mm), as a function of entrance ray height (mm) for a typical cynomolgus monkey [age = 5.25 years, post-mortem time = 2 hours] unstretched lens at (Left) *z* = 1.34 mm, (Center) *z* = 7.46 mm, and (Right) *z* = 11.54 mm. The position *z* = 11.54 mm is near the paraxial focus of the crystalline lens exhibiting the third-order behavior characteristic of spherical aberration. A third-order polynomial fit was performed on each plot (shown in red).

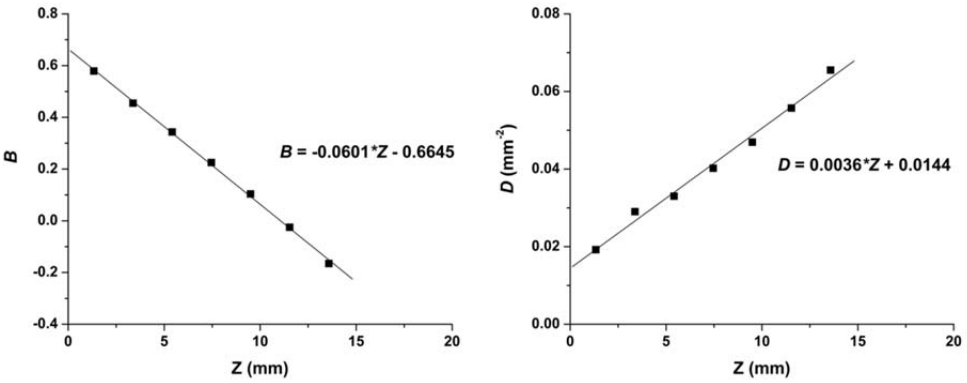


**Figure 4.4:** (Left) *B* and (Right) *D* coefficients plotted as a function of *z* distance for a typical cynomolgus monkey lens in the unstretched position. For this example, $m_B$ = -0.0601 mm$^{-1}$, $m_D$ = 0.0036 mm$^{-3}$, $b$ = 0.0144 mm$^{-2}$.

In the experimental setup, with the notation of Figure 4.5, the output ray height and slope are related to the input ray height and slopes by the following formula, expressed in paraxial matrix notation:

$$\begin{bmatrix} y \\ \theta' \end{bmatrix} = \begin{bmatrix} 1 - d_p \cdot \frac{P_L}{n_a} - P_L\left(\frac{d_w}{n_w} + z\right) & d_p + d_w \frac{n_a}{n_w} + n_a \cdot z \\ -P_L & n_a \end{bmatrix} \cdot \begin{bmatrix} h \\ \theta \end{bmatrix} \qquad \text{(Eq. 4.5)}$$

where $y$ is the measured ray height on the camera [mm], $\theta' = dy/dz$ is the output ray slope $d_p$ is the distance between the posterior surface of the lens and the anterior surface of the tissue chamber window [mm], $P_L$ is the measured effective power of the lens [D], $n_a$ is the refractive index of the medium ($n_a$=1.336), $d_w$ is the thickness of the glass window [mm], $n_w$ is the refractive index of the window ($n_w$=1.510), h is the entrance ray height [mm], and $\theta$ is the incident angle [°].

In these experiments, the incident angle is equal to zero ($\theta$=0). In this case, Eq. (4.5) can be simplified to:

$$y(z) = \left[1 - \frac{P_L \cdot d_p}{n_a} - P_L\left(\frac{d_w}{n_w} + z\right)\right] \cdot h \qquad \text{(Eq. 4.6)}$$

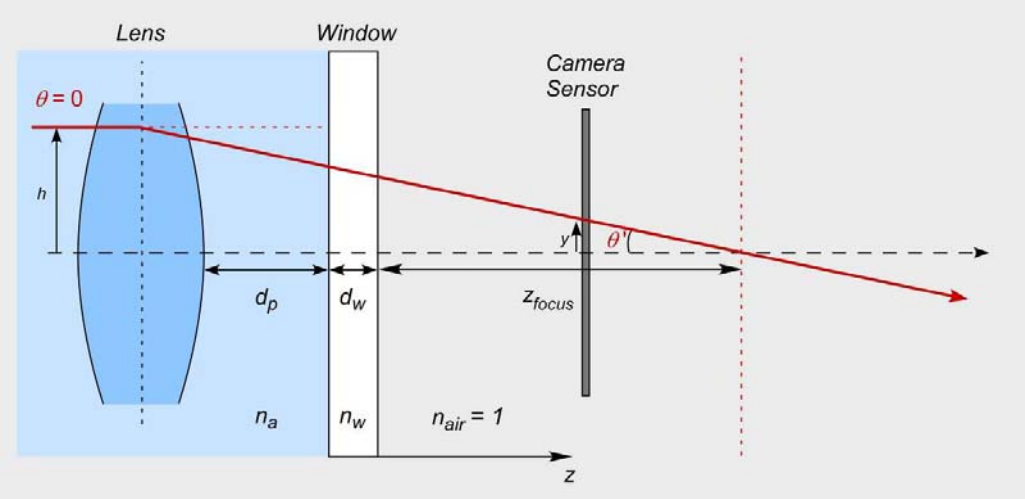


**Figure 4.5:** Schematic of LRT beam propagating through the lens along *z*-direction. *h* is the entrance ray height, $\theta$ *i*s the incident angle ($\theta$=0), $d_p$ is the distance between the posterior surface of the lens and the window of the tissue chamber, $n_a$ is the refractive index of the medium, $d_w$ is the thickness of the window, $n_w$ is the refractive index of the glass window, $n_{air}$ is the refractive index of air ($n_{air}$=1), *y* is the ray height incident on the camera, $\theta'$ = dy/dz is the output ray slope, and $z_{focus}$ is the distance between the posterior window surface and the intersection of the lens focus along the optical axis.

$$\theta' = \frac{dy}{dz} = -P_L \cdot h \qquad \text{(Eq. 4.7)}$$

Eq. (4.7) shows that the effective lens power is related to the output ray slope and entrance ray height. Comparison of Eq. (4.7) with Eq. (4.4) gives the following final result:

$$P_L = -m_B \qquad \text{(Eq. 4.8)}$$

The position of the lens focus is found by solving for the value of *z* that gives *y*=0 in Eq. 4.6, independent of *h*, which gives:

$$z_{focus} = -\frac{1}{P_L} - \frac{d_p}{n_a} - \frac{d_w}{n_w} \qquad \text{(Eq. 4.9)}$$

### *4.3.4 Calculation of lens spherical aberration*

In order to directly compare the spherical aberration coefficients, $D(z_{focus})$, measured with the Laser Ray Tracing system with previously published data, the values

were converted to Zernike spherical aberration coefficients. Higher-order aberrations other than spherical aberration were assumed to be negligible.

For each lens, the spot diagram at the focus was fit with a third-order term (Welford, 1986):

$$\Delta y(h) = D\left(z_{focus}\right) \cdot h^3 \qquad \text{(Eq. 4.10)}$$

where $\Delta y$ is the ray aberration equivalent to the spot shift on the camera [mm] at the paraxial focus of the lens, $h$ is the entrance ray height [mm], and $D(z_{focus})$ is the value of the function $D$ at the lens focus [$mm^{-2}$]. The contribution of spherical aberration to the Zernike wavefront aberration is (Thibos et al., 2002, Thibos et al., 2006):

$$W(h) = 6\sqrt{5} \cdot Z_4^0 \cdot \left(\frac{h}{a}\right)^4 \qquad \text{(Eq. 4.11)}$$

where $W$ is the wavefront aberration [μm], $Z_4^0$ is the Zernike spherical aberration coefficient [μm], $h$ is the input ray height [mm], and $a$ is the pupil radius [mm].

Using the Optical Society of America (OSA) recommend standards for reporting optical aberrations, the relation between ray aberration and wave aberration is (Thibos et al., 2002, Thibos et al., 2006):

$$\Delta y(h) = -\frac{R}{n'} \cdot \frac{dW}{dh} \qquad \text{(Eq. 4.12)}$$

where $R$ is the radius of the reference wavefront and $n'$ refractive index of the image space. In this case, for rays entering the lens parallel to the axis, $R$ is the effective focal length, $f'$, of the lens. In terms of the effective lens power, $P_L$:

$$\Delta y(h) = -\frac{1}{P_L} \cdot \frac{dW}{dh} \qquad \text{(Eq. 4.13)}$$

where $P_L = n'/f'$. Taking the derivative of Eq. 4.11:

$$\frac{dW}{dh} = \frac{24\sqrt{5}}{a^4} \cdot Z_4^0 \cdot h^3 \qquad \text{(Eq. 4.14)}$$

Combining Equations 4.5 and 4.6 results in:

$$\Delta y(h) = -\frac{24\sqrt{5}}{P_L \cdot a^4} \cdot Z_4^0 \cdot h^3 \qquad \text{(Eq. 4.15)}$$

Combining Equations 4.10 and 4.15 results in:

$$D = -\frac{24\sqrt{5}}{a^4} \cdot \frac{Z_4^0}{P_L} \qquad \text{(Eq. 4.16)}$$

Solving for $Z_4^0$ gives:

$$Z_4^0 = -\frac{a^4}{24\sqrt{5}} \cdot P_L \cdot D \qquad \text{(Eq. 4.17)}$$

The Zernike spherical aberration coefficient was determined from the value of the function *D(z)* at the paraxial focus of the lens (where $z = z_{focus}$). The Zernike spherical aberration coefficient, $Z_4^0$, in µm, was calculated using the OSA standard for a 6-mm optical zone based on published formulas (Welford, 1986):

$$Z_4^0 = -\frac{a^4}{24 \cdot \sqrt{5}} \cdot P_L \cdot D\left(z_{focus}\right) \qquad \text{(Eq. 4.18)}$$

where $a$ is the pupil radius ($a$ = 3 mm), $P_L$ is the effective lens power and $D(z_{focus})$ is the value of the function at the focal point of the lens.

## 4.4 Experiments

### *4.4.1 Donor tissue*

Data were acquired using 24 lenses from 20 cynomolgus monkeys (Macaca fascicularis; ages 4.4 – 16.0 years; postmortem time 13.5 ± 13.0 hours). In the four cases where the left and right eyes were measured in the same monkeys, there was a high degree of similarity between eyes. In the case where both eyes were measured, power and spherical aberration data were averaged for the analysis.

All experiments adhered to the Association for Research in Vision and Ophthalmology Statement for the Use of Animals in Ophthalmic and Visual Research. The eyes were obtained from the Division of Veterinary Resources at the University of Miami as part of a tissue-sharing protocol and were used in accordance with Institutional Animal Care and Use Guidelines. The eyes were enucleated immediately after monkeys were euthanized and wrapped in gauze and stored in a closed container. No animals were euthanized for the sole purpose of this study. Upon arrival at the laboratory, all eyes were either prepared for stretching experiments or refrigerated at 4°C (Nankivil et al., 2009).

### *4.4.2 Lens stretching experiments*

The tissue preparation protocol was described in Chapter 3. The EVAS II system was used to reproduce accommodation in post-mortem lenses. During the stretching experiment, the OCT beam was centered on the crystalline lens and the LRT system performed a ray trace by delivering 51 equally-spaced parallel rays along one meridian of the lens over the central 6-mm optical zone. A camera module mounted on a vertical positioning stage below the tissue chamber was used to record the spots corresponding to

each individual ray (51 in total). Images were acquired at multiple axial positions along the optical axis covering a range of up to 25 mm below the chamber (Figure 4.2). LRT experiments were performed on lenses in the unstretched and stretched (shoes were displaced radially outward by 2.5 mm) states.

## 4.5 Results

### *4.5.1 Effective lens power*

The effective lens power is greater in the unstretched (accommodated) state than in the stretched (unaccommodated) state, as expected. Figure 4.6 shows the effective lens power for cynomolgus monkey lenses plotted with respect to age. There is a significant decrease in the unstretched lens power with age ($p<0.0001$) while the stretched lens power is relatively constant. On average, the effective lens power is 59.10±4.27 D for young cynomolgus monkeys (<9.3 years) and 46.3±2.86 D for older cynomolgus monkeys (>13.3 years) in the unstretched state. The average effective power is 33.55±3.41 D for lenses in the stretched state.

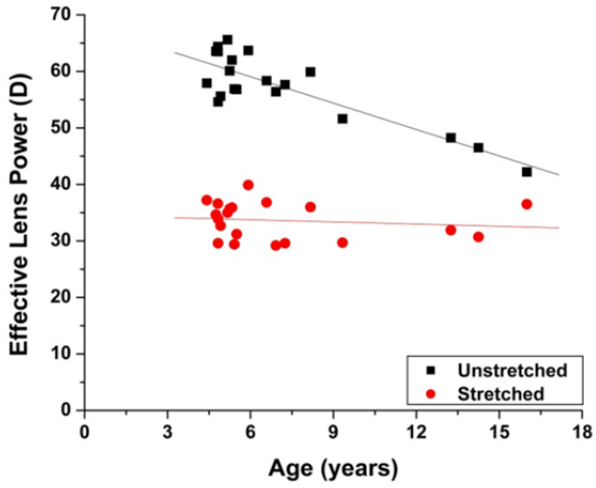


**Figure 4.6:** Effective lens power for cynomolgus monkey lenses with respect to age. There is a significant decrease in the unstretched lens power with age.

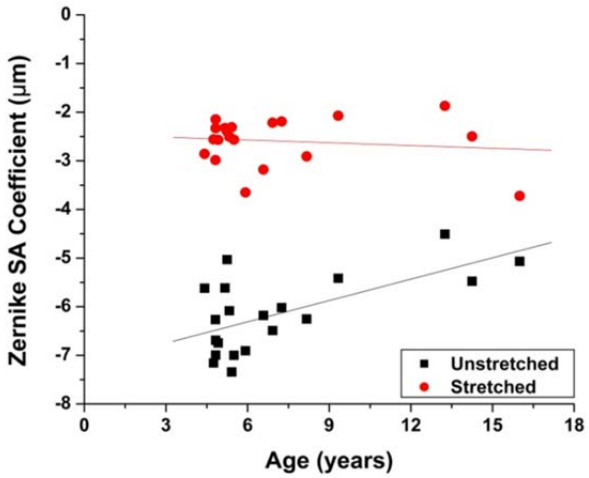


**Figure 4.7:** Zernike spherical aberration coefficient for cynomolgus monkey lenses plotted with respect to age. The unstretched lens shifts towards less negative spherical aberration with age.

### *4.5.2 Spherical aberration*

Figure 4.7 shows the Zernike spherical aberration coefficients for cynomolgus monkey lenses plotted with respect to age. Spherical aberration is more negative in the unstretched state than in the stretched state for all lenses. There is a significant positive correlation between the unstretched lens spherical aberration and age ($p=0.002$). On average, spherical aberration for the unstretched lens is -6.32±0.60 µm for young cynomolgus monkeys and -4.89±0.48 µm for older cynomolgus monkeys. The average spherical aberration is -2.57±0.52 µm for lenses in the stretched state. Stretching experiments produced changes corresponding to the lens spherical aberration becoming more negative with accommodation.

## 4.6 Discussion

This study demonstrated a new method to directly measure the changes in the spherical aberration of the lens during simulation of accommodation using a Laser Ray

Tracing system with a translating imaging sensor. The individual ray slopes were recreated and the focal length and spherical aberration of the lens at the paraxial focus were determined by recording spot images at multiple positions along the optical axis.

There is evidence that the lens is not rotationally symmetric and that spherical aberration varies along different meridians (Sun et al., 2014). In addition, it is possible that the lens stretcher could induce unexpected high-order aberrations. The current system is limited to measurements of spherical aberration along a single meridian and does not allow us to reconstruct complete 2-D aberration maps and quantify these effects.

These results show that the spherical aberration of the cynomolgus monkey lens is negative in the stretched (relaxed) state and becomes more negative with accommodation. We also find that the lens spherical aberration tends to become less negative with age. Based on the human age to equivalent primate age conversion (monkey age = human age/3) from Bito et al. (1982), humans become presbyopic at around 40-50 years so the equivalent monkey presbyopic age is 13-17 years. A linear regression was performed on the lens spherical aberration versus age to determine if there was a statically significant age-dependence. However, more data is required over a broader age range and with a more uniform distribution in order to verify if the age-dependent is linear, or if it follows a more complex non-linear behavior.

Overall, these findings are consistent with the previous *in vitro* studies on human lenses (Glasser & Campbell, 1998) and the preliminary results obtained on a macaque monkey lens by Roorda and Glasser (2004). These results cannot be directly compared with those by Glasser and Campbell (1998) because in their study the lens spherical aberration was presented as the longitudinal spherical aberration calculated for a

normalized lens diameter in Diopters. However, the general behavior of the cynomolgus monkey lenses in this study is similar to that of human lenses.

Interestingly, the measured spherical aberration values in this study are comparable to the predicted spherical aberrations, obtained on the same cynomolgus monkey lenses, using the GRIN reconstruction model by de Castro et al. (2013). Seven of the cynomolgus monkey lenses used in the present study were also used in the GRIN reconstruction study by de Castro et al. (2013). In that study, the GRIN was reconstructed with a search algorithm using the optical path measured from OCT images and the measured back focal length. A numerical ray-trace was performed through the reconstructed lens for a 6-mm pupil diameter (101 rays, ray spacing 30 μm) to estimate the spot diagrams at the same *z* positions as the LRT experiment. The spot diagrams for the reconstructed GRIN lens were simulated based on the ray-trace for lenses at the corresponding camera positions, *z*, in the unstretched and stretched states. The spot diagrams for the simulated spot diagrams are in close agreement with the measurements acquired with the LRT in the present study (Figure 4.8). Moreover, the predicted lens spherical aberration based on the reconstructed GRIN lens model is in good agreement with the measured spherical aberration using LRT for the seven lenses. Figure 4.9 (Left) shows the predicted spherical aberration versus the measured spherical aberration, and (Right) the Bland-Altman analysis for the two different methods. The difference between the two methods fell within ±2 SD for all lenses and the mean difference was -0.51 μm. The close agreement between experimental data and the model predictions using these two independent methods serves to validate the method for reconstructing the lens gradient refractive index from OCT images of crystalline lenses.

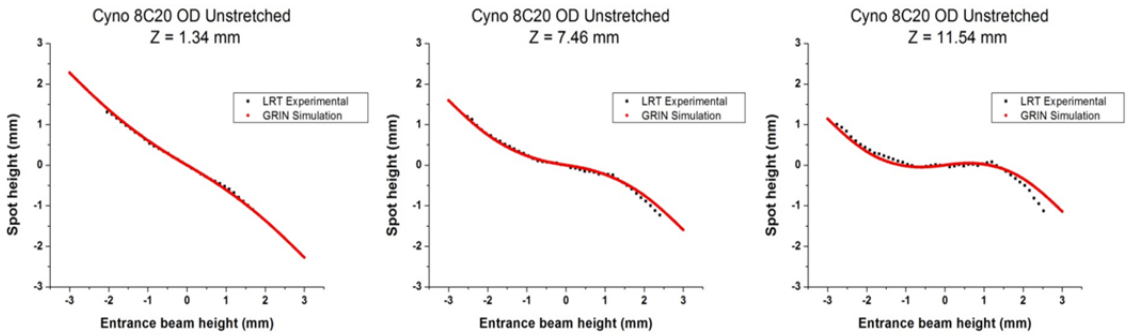


**Figure 4.8:** Spot diagrams for a typical cynomolgus monkey (age = 4.42 years, post-mortem time = 26 hours) unstretched lens. The spot heights obtained with the Laser Ray Tracing system are shown in black and the spot heights from the de Castro simulation (de Castro et al., 2013) are shown in red. The LRT experimental data were offset to be centered about zero to allow for direct comparison with the GRIN simulated data. The spot diagrams are shown for the (Left) $z$ = 1.34 mm, (Center) $z$ = 7.46 mm, and (Right) $z$ = 11.54 mm positions.

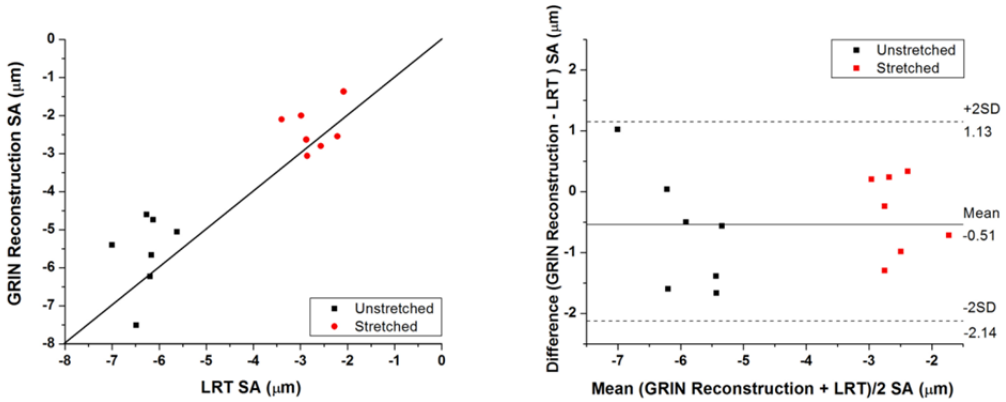


**Figure 4.9:** (Left) The predicted Zernike spherical aberration based on the reconstructed GRIN lens model (de Castro et al. 2013) plotted with respect to the measured Zernike spherical aberration using LRT for the same 7 cynomolgus monkey lenses. (Right) Bland-Altman plot of predicted spherical aberration versus measured spherical aberration.

This study showed that the OCT beam used to image the crystalline lens in the EVAS II stretching system can also be used for the LRT system, without requiring additional optics to refocus the beam on the imaging sensor. We were able to recreate the individual ray slopes by recording spot images at multiple positions along the optical axis with an imaging sensor mounted on a translation stage below the lens. This technique solves some of the limitations of the lateral LRT technique and can also be extended to

produce an aberration map by using a 2-D scan, similar to the method of Roorda and Glasser (2004).

One of the issues encountered by using the OCT beam as the LRT beam is that the beam is focused on the crystalline lens to provide the best quality OCT image. As a result, the beam diverges after it exits the crystalline lens. When the camera position is moved away from the lens and near the lens focus, the OCT beam becomes defocused, which reduces the quality of the spot images and the precision of the centroid calculation. To minimize this effect, spot images were recorded away from the focus near the tissue chamber, and the focus position was calculated from the linear fit of the function *B(z)* in Eq. (4.1). Another potential source of error in the LRT system is that the posterior window of the tissue chamber may contribute to the measured spherical aberration. To quantify the potential error introduced by the window, a ray-trace analysis was performed using ray-tracing software (OSLO, Lambda Research Corp, Littleton, MA). The analysis showed that the window contributes approximately 2% error to the spherical aberration coefficient (-0.4325 μm with the window compared to -0.4234 μm without) compared to the crystalline lens spherical aberration, which averaged -6.08±0.79 μm in the unstretched position and -2.57±0.52 μm in the stretched position. The window contribution was therefore not taken into account.

## 4.7 Summary and conclusion

In summary, the LRT system allows for the direct measurement of lens effective power and spherical aberration. The data shows that spherical aberration is negative in cynomolgus monkey lenses, and that spherical aberration becomes more negative with

accommodation and becomes less negative with age. This study produced results which are in very good agreement with the results obtained from numerical ray-tracing based on a model of the lens which serves to validate the GRIN reconstruction technique. Thus, lens spherical aberration can be measured experimentally using laser ray tracing or predicted using the GRIN reconstruction technique based on OCT images of the crystalline lens and the measured back focal length.

These experiments demonstrated the feasibility of directly measuring the changes in lens power and spherical aberration during simulated accommodation using a Laser Ray Tracing system with a translating imaging sensor. However, the current system is limited to measurements of spherical aberration along a single meridian, and does not allow us to reconstruct complete 2-D wavefront aberration maps of the crystalline lens. In addition, only on-axis measurements can be acquired with the current configuration. The next chapter will describe an enhanced LRT system which enables us to measure the changes in lens power and spherical aberration with simulated accommodation, both on-axis and off-axis, as well as the complete higher-order aberration maps of the crystalline lens.

# CHAPTER 5

# DESIGN OF A COMBINED LASER RAY TRACING AND OPTICAL COHERENCE TOMOGRAPHY SYSTEM TO MEASURE LENS OFF-AXIS POWER AND ABERRATIONS

## 5.1 Purpose

This chapter describes the development of a combined laser ray tracing (LRT) and optical coherence tomography (OCT) system related to Aim 3 of the project. The purpose of the LRT-OCT system is to measure the accommodative changes in lens power and aberrations both on-axis and off-axis. Ultimately, one of the future applications of this system will be to acquire off-axis 3-D OCT images of the crystalline lens to reconstruct the lens gradient refractive index.

## 5.2 Background and rationale

The feasibility of using a laser ray tracing system with a vertically translating imaging sensor to directly measure lens power and spherical aberration was demonstrated in the previous chapter. However, the LRT system was limited to measurements of spherical aberration along a single meridian, and did not allow for the reconstruction of complete 2-D wavefront aberration maps of the crystalline lens. Furthermore, the system was limited to on-axis measurements of lens power and spherical aberration and was not capable of obtaining off-axis measurements.

Based on the preliminary system described in Chapter 4, an enhanced laser ray tracing system was designed and built to measure the power and aberrations of crystalline lenses during simulated accommodation in a motorized lens stretcher. The combined LRT-OCT system will allow for the acquisition of off-axis 3-D spectral OCT images of

the lens and 2-D LRT data to measure complete higher-order aberration maps of the crystalline lens with stretching.

## 5.3 System overview

The laser ray tracing system uses the OCT system's light source as the LRT beam. The OCT system is used to center and align the crystalline lens for LRT experiments. The LRT and OCT systems share the same beam delivery optics. The beam delivery optics are mounted on a motorized rotation stage that pivots around the crystalline lens to allow acquisition of off-axis spot patterns. The LRT delivers rays across the crystalline lens at varying delivery angles and an imaging sensor which is mounted on a two-dimensional motorized positioning stage below the lens is used to record the spot positions along each individual ray for all delivery angles. The tissue sample is mounted into a motorized lens stretching system and placed in a tissue chamber within the system. A basic schematic of the LRT-OCT system depicting the off-axis data acquisition is shown in Figure 5.1.

The LRT-OCT system consists of the following components:

- Commercial spectral-domain OCT system (Bioptigen ENVISU R4400)
- Custom beam delivery probe mounted on a motorized rotation stage
- Camera mounted on motorized horizontal and vertical positioning stages
- Mini-motorized lens stretching apparatus
- Tissue chamber
- Computer with custom developed LabView software for automated data acquisition and control of motorized positioning stages

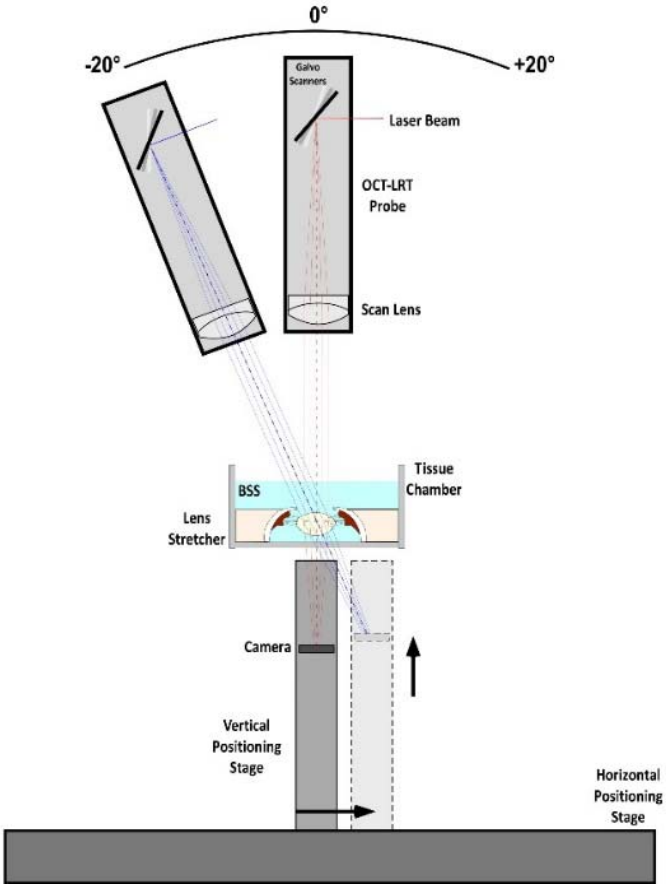


**Figure 5.1:** Schematic of LRT-OCT system demonstrating the principle of off-axis LRT data acquisition. The probe rotates about the crystalline lens and a camera mounted on a two-dimensional motorized positioning stage below the tissue chamber is used to record the spot positions along each individual ray for all delivery angles.

An LRT experiment is performed by projecting the beam onto the center of the crystalline lens. The camera is positioned directly below the tissue chamber and the horizontal position is adjusted automatically until the camera detects the beam. Once the beam is detected, the camera's horizontal position is automatically adjusted so that the spot is centered on the camera. Then, the LRT scanning sequence commences. An image is recorded for each individual ray of the scan sequence. Once the sequence is complete, the vertical height of the camera is adjusted (lowered) and the beam detection, centering, and LRT scanning sequence is repeated. This process is repeated for multiple camera vertical positions and multiple delivery angles, ranging from -45° to 45°, to obtain on-

axis and off-axis LRT spot patterns. The LRT-OCT system is controlled via LabView (National Instruments Corporation, Austin, TX) software to allow automated data acquisition. Figure 5.2 shows the SolidWorks assembly of the LRT-OCT system.

## 5.4 Hardware

### *5.4.1 OCT system modifications and delivery optics*

The LRT-OCT system uses a high-speed commercial ENVISU R4400 Spectral-Domain OCT system (16 mm depth range, 8 μm axial resolution in air) from Bioptigen, Inc. (Durham, NC). The OCT system uses a super-luminescent light emitting diode (Part No. IPSDS0806, Inphenix, Livermore, CA) light source with a continuous wave output operating at a center wavelength in the region of 880 nm and a bandwidth of 40 nm. The ENVISU R4400 is equipped with a handheld delivery probe (Figure 5.3). For our specific application, a custom delivery probe with a 100 mm working distance was required in order to image the crystalline lens. The Bioptigen OCT system was modified by adding a second control box to interface the galvanometer scanners of the custom delivery probe with commercial Bioptigen OCT system. The user has the option to switch the light source to use the handheld probe (for *in vivo* use) or the custom delivery probe (for *ex vivo* use). A basic schematic depicting the OCT modifications are shown in Figure 5.4.

The custom delivery probe was built based on a previous design described in Ruggeri et al., 2012. The probe consists of an aspheric lens collimator (C220TME-B, f = 11 mm, Thorlabs, USA), an X-Y galvanometer optical scanner (6210H, Cambridge Technology, Inc., USA) and a near infrared (NIR) achromatic objective lens (AC254-100-B, f = 100 mm, Thorlabs, USA). The collimator produces a 1.8 mm diameter beam.

The objective lens is aligned to provide a telecentric scan with flat field along the horizontal axis. The focused beam has a diameter of 62 μm at the beam waist and a depth of focus of 5.1 mm (in air). For optimal imaging quality, the focal plane of the scanning beam must be posvcgitioned near the center of the crystalline lens during imaging (Ruggeri et al., 2012).

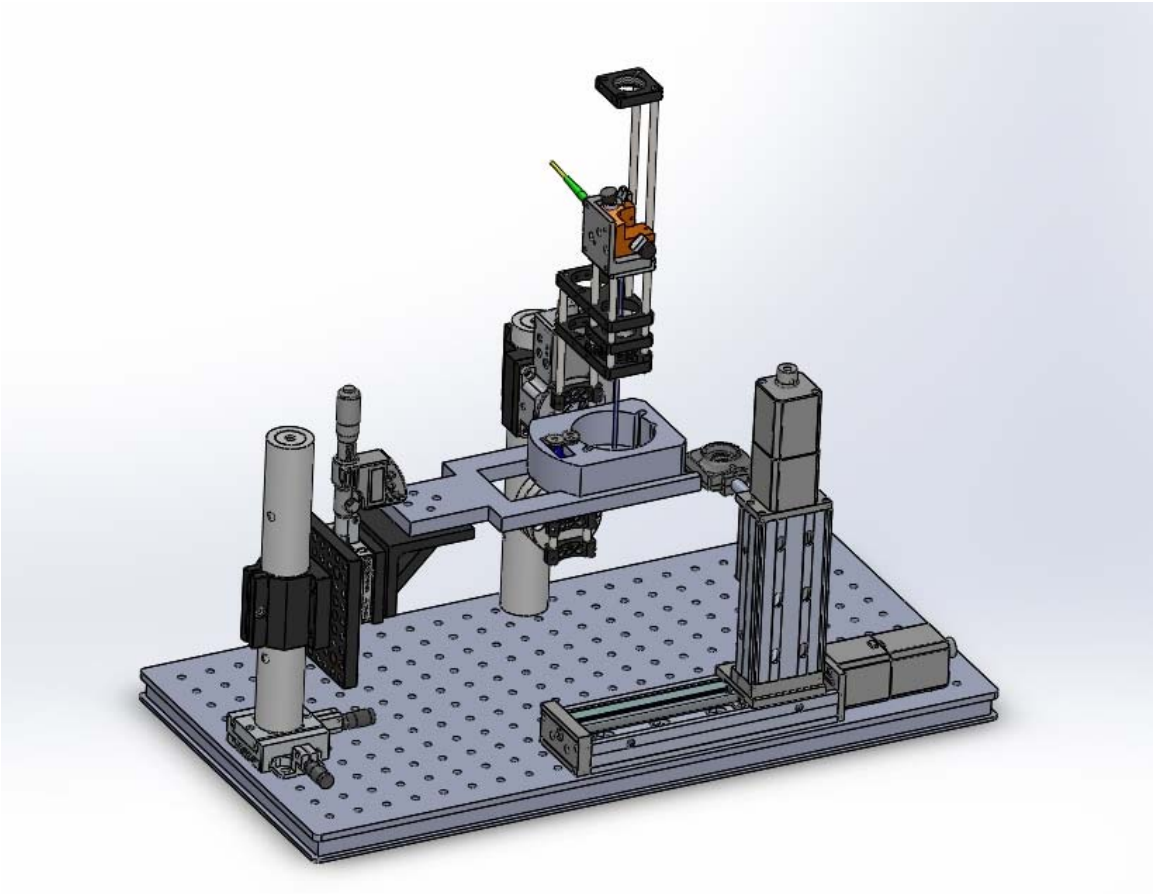

**Figure 5.2:** SolidWorks assembly of the combined laser ray tracing (LRT) and optical coherence tomography (OCT) system.

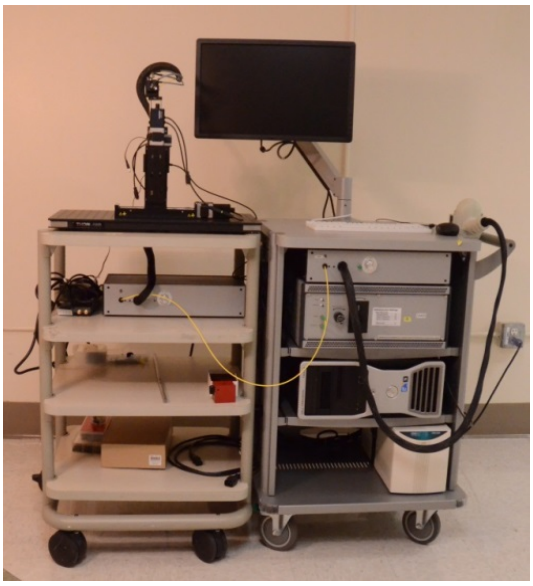

**Figure 5.3:** The LRT-OCT system benchtop setup and the corresponding control box are on the cart on the left. The Bioptigen ENVISU R4400 Spectral-Domain OCT system including the monitor, control box, computer tower, and power supply are shown on the cart on the right.

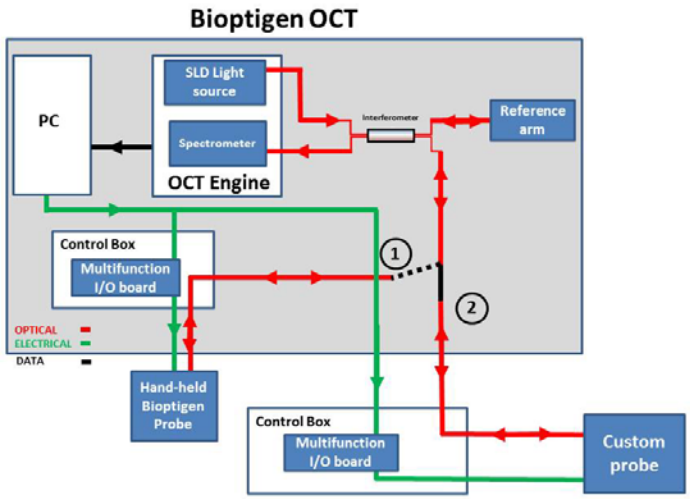


**Figure 5.4:** Basic schematic of the modifications made to the Bioptigen OCT system. The components in the gray box were part of the commercial Bioptigen OCT system. The second control box and custom delivery probe were integrated with the Bioptigen OCT for our application. The user has the option to switch the light source to use the 1) handheld probe or 2) the custom delivery probe.

### *5.4.2 Rotation positioning stage*

In order to obtain off-axis measurements of the crystalline lens, the custom delivery probe must pivot around the crystalline lens to image the off-axis LRT spot patterns. The maximum desired projection angle of the delivery beam onto the crystalline

lens is ±45°. The motorized rotation stage (T-RS60A, Zaber Technologies, Vancouver, BC) was selected for our application. The stage is stepper motor driven with built-in controller capable of a full 360 degree rotation, which meets the design criteria for the maximum delivery angle. The Zaber stage is daisy-chainable which allows it to be easily linked to other Zaber devices (discussed further in the Section 5.4.4). A list of motorized rotation stage specifications are shown in Table 5.1.

The custom delivery probe was mounted on the motorized rotation stage. The objective lens was positioned 100 mm from the center of the axis of rotation so that the beam waist (focused beam) coincides with where the crystalline lens is in the system.

| Specification | Value |
|---|---|
| Micro-step Size | 0.000234375° |
| Travel Range | 360° |
| Accuracy | 0.1° |
| Repeatability | < .02° |
| Backlash | < 0.06° |
| Maximum Speed | 13.2 °/s |
| Minimum Speed | 0.0011 °/s |
| Guide Type | Pre-loaded ball bearing |
| Motor Type | Stepper (2 phase) |
| Weight | 0.48 kg |

**Table 5.1:** Motorized rotation stage (T-RS60A) specifications.

| Parameter | Target |
|---|---|
| Exposure Mode | Electronic Rolling Shutter |
| Read Out Mode | Progressive Scan |
| Resolution | 1280 x 1024 Pixels |
| Mode | Monochrome |
| Frame Rate, Freerun Mode | 25 fps |
| Exact Sensitive Area | 6.66 mm x 5.32 mm |
| Pixel Size | 5.2 µm, Square |

**Table 5.2:** Camera specifications.

### *5.4.3 Camera*

The critical design criteria for the camera were the image sensor size, pixel resolution and frame rate. The camera should also be compact to fit directly below the tissue chamber. The protocol for LRT experiments scans the central 6-8 mm optical zone of the crystalline lens. Based on a lateral scan length of 8 mm, the minimum active area of the camera was determined by the scan length measured closest to tissue chamber. Assuming the image sensor is positioned 5 mm below the crystalline lens, the minimum desired active area of the image sensor is 7.31 mm. The total length of the experiment is constrained by the frame rate of the camera since so many images are recorded. Therefore, a high frame rate of 60 frames per second (fps) or above was desired for this application.

Several cameras were considered; however, the cameras which met the target values for both the image sensor size and frame rate were very expensive. Due to its low cost and availability, a high resolution board-level complementary metal-oxide semiconductor (CMOS) board-level camera (DCC1545M-GL, Thorlabs, USA), was selected for initial testing. The camera has an active area of 6.66 mm x 5.32 mm, 1280 x 1024 pixels in full frame mode, and 5.2 μm x 5.2 μm pixel size. The camera has a frame rate of 25 fps (in full frame mode) up to 250 fps (with reduced areas of interest). A full list of the camera specifications is shown in Table 5.2. With this camera, the maximum scan length of 8 mm can be recorded approximately 11.17 mm below the crystalline lens (using 6.66 mm as the camera length). Taking into account the position of the lens in the tissue cell, the distance between the posterior lens surface and the bottom of the cell is roughly 4 mm and the thickness of the window is 1 mm. Thus, the maximum scan length

can be recorded 6 mm below the tissue cell. Considering the physical dimensions of the camera height, the image sensor is an acceptable size of the LRT system.

### *5.4.4 Horizontal and vertical linear positioning stages*

The critical design parameters for the horizontal and vertical positioning stages were the travel range, resolution and repeatability. Since we want to capture LRT images from the position closest to the crystalline lens all the way at the lens focus, the travel range of the vertical stage is approximately equal to the focal length of the crystalline lens. The maximum travel range of the vertical stage was determined based on an extreme case for an older human lens. Assuming a delivery incidence angle of 0° and a lens power of 15 D, the focal length of the typical old human lens is 66.7 mm. Based on this case, a minimum travel range of 70 mm was chosen for the vertical positioning stage. A motorized linear slide with a 75 mm travel range was selected (T-LSR075B, Zaber Technologies, Vancouver, BC) for the LRT system.

Similarly, the travel range of the horizontal positioning stage was determined based on the extreme case for an older human lens. Assuming a maximum delivery angle of 45° and a lens power of 15 D, the spot height of the central ray at the focus is ±47.2 mm from the optical axis. This corresponds to a minimum total travel range of 94.4 mm for the horizontal stage. A motorized linear slide with a 150 mm travel range was selected (T-LSR150B, Zaber Technologies, Vancouver, BC) for the LRT system. A full list of the horizontal and vertical motorized stage specifications are shown in Table 5.3.

The horizontal and vertical positioning stages have a resolution of 0.496 μm, repeatability of < 2.5 μm, and an accuracy of ±8 μm. Both stages have a potentiometer

knob for smooth manual control and are stand-alone units. In addition, the stages have an integrated stepper motor controller and motor driver so a separate motion controller and driver is not needed. An additional advantage of the Zaber stages is that multiple stages can be assembled together and daisy-chained. The three positioning stages (1 rotation, 2 linear) can share one 15 V power supply and can be controlled via serial port without additional hardware, making the programing in LabVIEW straightforward.

| **Parameter** | **Target** | |
|---|---|---|
| | **Vertical** | **Horizontal** |
| Micro-step Size | 0.496 µm | |
| Travel Range | 75 mm | 150 mm |
| Accuracy | 15 µm | |
| Repeatability | < 2.5 µm | |
| Backlash | < 7 µm | |
| Maximum Speed | 20 mm/s | |
| Minimum Speed | 0.00465 mm/s | |
| Guide Type | Roller bearing | |
| Motor Type | Stepper (2 phase) | |
| Weight | 1.20 kg | 1.40 kg |

**Table 5.3:** Motorized vertical (T-LSR075B) and horizontal (T- LSR150B) positioning stage specifications.

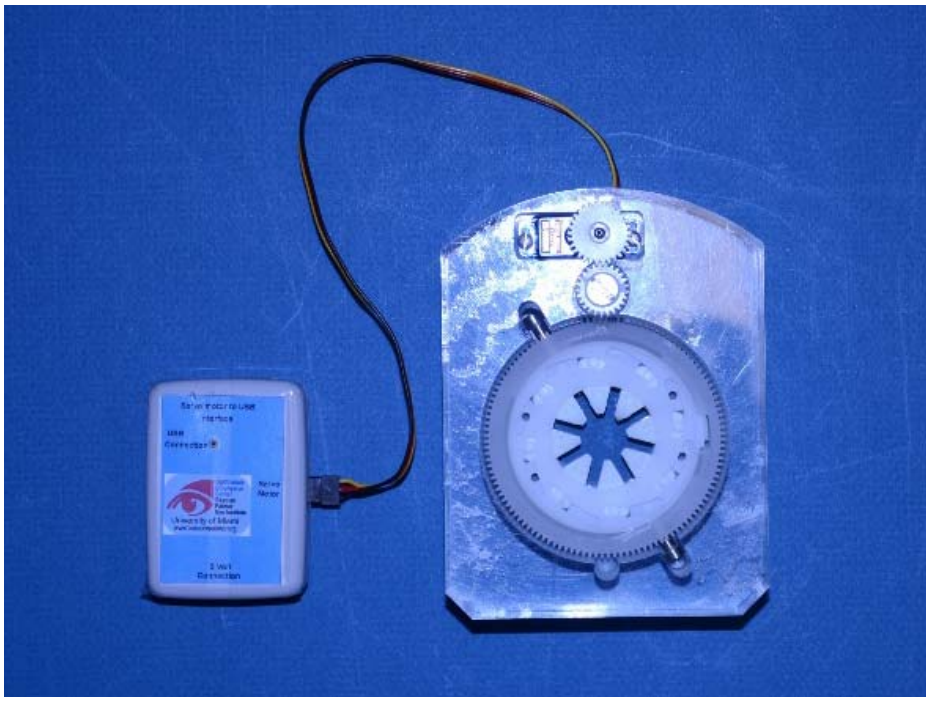

**Figure 5.5:** The mini-motorized lens stretching apparatus (mMLSA) used for automated stretching of the ocular tissue mounted in the tissue chamber. The USB control unit (shown on the left) connects the mMLSA directly to the computer.

### *5.4.5 Mini-motorized lens stretching apparatus*

A custom miniature lens stretching system was motorized to allow for the automated stretching of the ocular tissue (Figure 5.5). The lens stretcher was modified from a previous design (STR-MS-B, Basic lens stretcher, Bioniko Consulting LLC, Sunny Isles Beach, FL) to meet the physical constraints and stretching requirements for the LRT-OCT system. A minimum shoe displacement of 5.00 mm was necessary to simulate dis-accommodation in human and non-human primate lenses.

The mini-motorized lens stretching apparatus (mMLSA) consists a top plate, bottom plate, eight scleral shoes, and an outer case which holds of all the components together. The eight shoes are inserted into the bottom plate and are configured in a ring orientation to fit around the ocular tissue. The mMLSA simulates dis-accommodation of the lens by moving the shoes outwards to a maximum of 5.25 mm (in total). The lens

stretcher was programmed to displace the shoes outward in increments of 0.5 mm, up to 5.25 mm (discussed in Section 5.5). The stretching positions were calibrated to verify the displacement of the individual shoes. The calibration details are presented in the next section.

### *5.4.6 Tissue chamber and X-Y-Z positioning stage*

A custom tissue chamber (Figure 5.5) was fabricated to house the mMLSA. The tissue chamber has a built-in micro servo motor (HS-5055, Servo City, Winfield, KS) and gears which rotate the outer ring of the mMLSA and thereby shift the positions of the shoes to stretch the ocular tissue. The servo motor positions were carefully calibrated using a modified optical comparator (Topcon BP-30S, Tokyo, Japan) to verify the displacement of the individual shoes in both the stretching and de-stretching (reverse) directions. Figure 5.6 shows the position of the servo motor (in º) plotted with respect to the average shoe displacement (mm).

The bottom of the tissue chamber is a sapphire window (45-568, Edmund Optics, USA) of 1 mm thickness. The mMLSA is inserted into the tissue chamber which is positioned on the custom aluminum mount shown in Figure 5.7. The mount is fork-shaped which allows the camera to move directly below the tissue chamber to acquire images as close to the crystalline lens as possible. The mount extends from a 3-axis translation stage (460A-X & 460A-XY, Newport Corporation, Irvine, CA) enabling the precise alignment and centering of the crystalline lens for measurements in the LRT-OCT system (Figure 5.7).

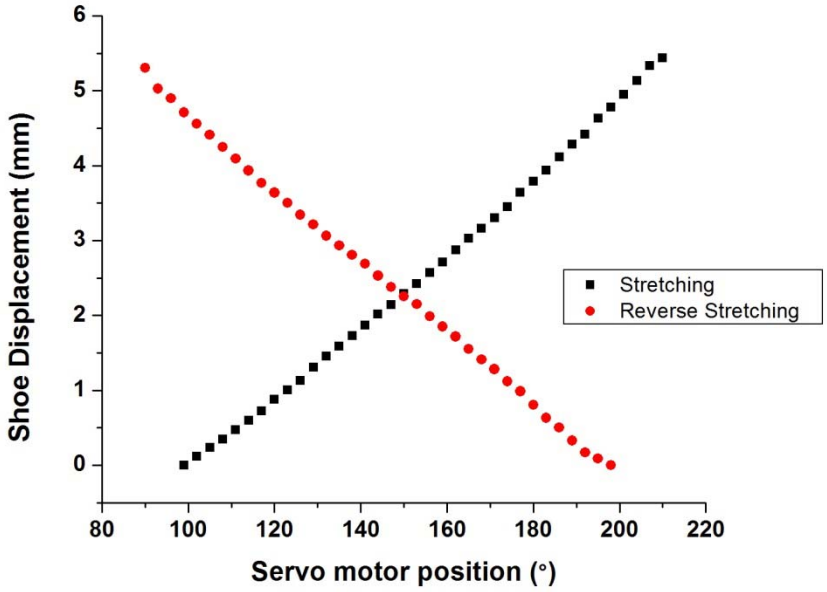


**Figure 5.6:** Servo motor position (in °) plotted as a function of shoe displacement (mm) for the mini-motorized lens stretching apparatus (mMLSA).

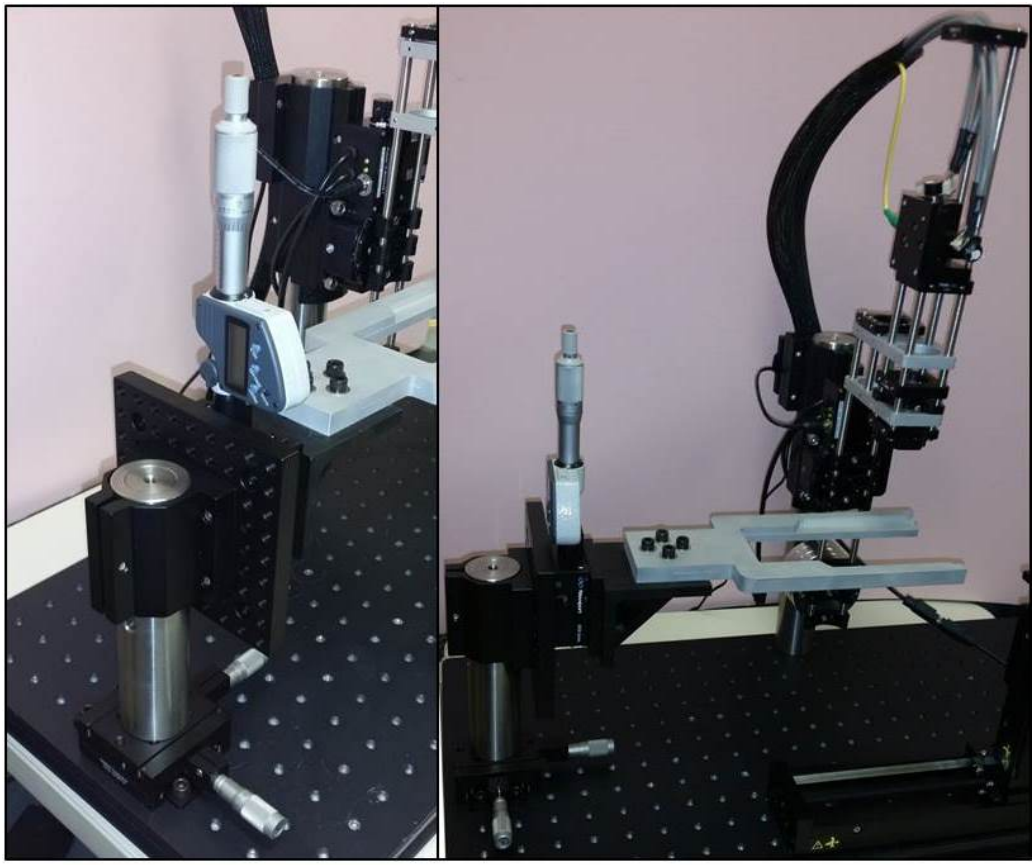

**Figure 5.7:** (Left) Close-up of the 3-axis translation stage which allows for precise positioning of the crystalline lens in the LRT-OCT system. (Right) Side view of 3-axis translation stage and aluminum mount to hold tissue chamber. Tissue mount was fabricated by Juan Silgado.

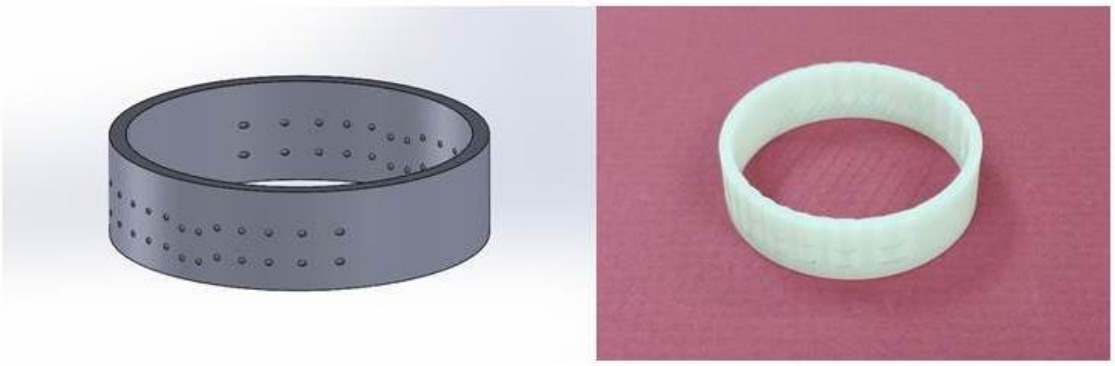

**Figure 5.8:** (Left) SolidWorks drawing and (Right) fabricated lens holder for imaging isolated crystalline lenses.

### *5.4.7 Isolated lens holder*

A custom lens holder was designed and fabricated to enable LRT-OCT experiments to be performed on isolated crystalline lenses (Figure 5.8, Right). The lens holder consists of a small plastic ring with 10-0 nylon sutures (Aurolab, Veerapanjan, Madurai, India) cross-stitched throughout the length of ring. The isolated lens is placed in the center of the ring using a lens spoon. The sutures position the lens 3.5 mm from the bottom of the tissue chamber, which is roughly the position of the lens when the tissue is mounted in the mMLSA. The sutures in the outer region of the lens holder run straight across the ring, while the sutures in the center region dip downwards. The radius of curvature of the central region is approximately 6 mm to match the shape of the posterior lens surface for an average adult human lens (Figure 5.8, Left).

## 5.5 Software

### *5.5.1 OCT imaging program*

During an OCT imaging experiment, the user records OCT images of the crystalline lens at various stretching positions, and at multiple delivery angles. The

Bioptigen InVivoVue software is used to scan and image the crystalline lens in real-time, and record the OCT images. An additional program was necessary to allow the user to control the lens stretcher and the orientation of the delivery probe.

Custom software was developed in LabView to control the stretching position of the mMLSA and the angle of the motorized rotation stage for on- and off-axis OCT imaging of the crystalline lens. Figure 5.9 shows a screenshot of the Bioptigen computer during an OCT imaging experiment. The Labview Virtual Instrument (VI) is seen on the left. The user has the option to choose the stretch position which range from: Home, Start, 0.5 mm, 1.0 mm, … 5.25 mm, and Center. The "Home" position is used to insert and remove the mMLSA from the tissue chamber. The "Start" position is equivalent to the unstretched (0 mm) position and is used as the starting position for stretching experiments. The "Center" position is used to remove the gears from the tissue chamber for cleaning purposes.

The user also has the option to select the delivery angle corresponding to the projection angle of the OCT probe (in air) onto the crystalline lens. The allowable delivery angles range from -45° to +45°, and vary in 5° increments. Furthermore, the user can choose the orientation of the mMLSA to indicate whether the lens stretcher is in the normal (anterior lens surface is upwards) or inverted (posterior lens surface is upward) orientation. The inverted orientation is used for imaging the lens posterior surface and is beyond the scope of this project. The right side of Figure 5.9 shows the Bioptigen InVivoVue software which allows the user to scan and record OCT images the lens.

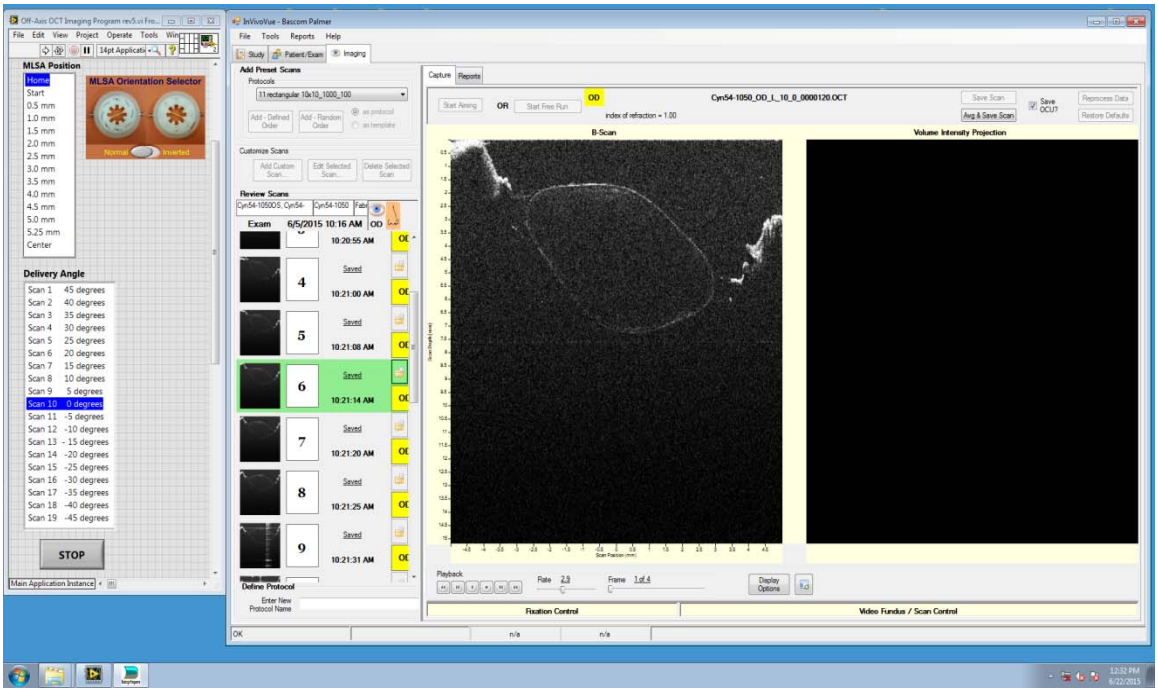


**Figure 5.9:** Screenshot of Bioptigen computer during an OCT imaging experiment. The custom Labview program (shown on the left) allows the user to control the stretching position of the mMLSA and adjust the delivery angle of the OCT probe. The Bioptigen InVivoVue software (shown on the right) allows the user to scan and image the crystalline lens in real-time and to record OCT images.

### *5.5.2 LRT program*

#### *5.5.2.1 General description*

During an LRT experiment, the custom delivery probe delivers narrow parallel beams sequentially through the crystalline lens to measure the lens power and aberrations. Control software was needed to allow the user to select the stretch position, scan pattern, height/positions of the camera, and the delivery angles for the LRT experiment. A flowchart of the LRT experimental process is shown in Figure 5.10.

At the start of the experiment, all of the devices are homed. Then, the tissue is stretched to the designated stretching position and a centering or "aiming" beam is projected onto the crystalline lens. The camera moves below the tissue chamber and locates the beam. Once the beam is detected, the beam is centered on the camera and the LRT scanning sequence begins. An image is recorded for each individual ray of the scan

sequence. Once the scan sequence is completed, the vertical height of the camera is adjusted and the beam detection, centering, and LRT scanning sequence is repeated. This process is repeated for each delivery angle, ranging from -45° to 45°, to obtain on-axis and off-axis LRT spot patterns.

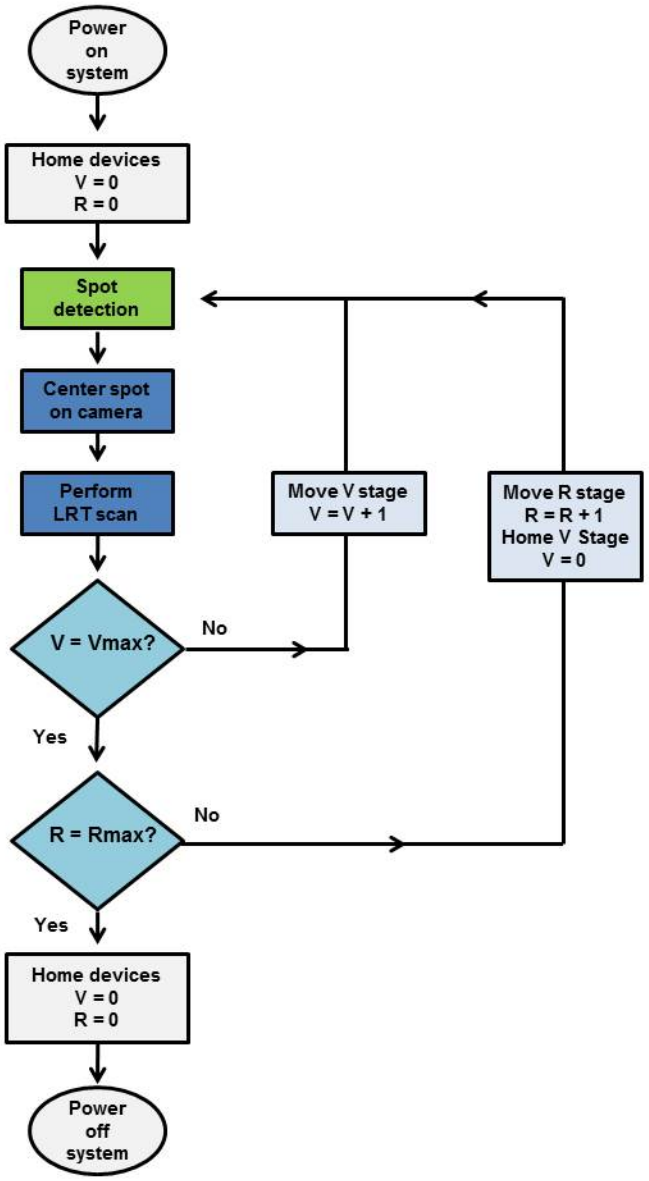


**Figure 5.10:** Basic flowchart of an LRT experiment. The stages are abbreviated where V = vertical and R = rotation. The sequence for the V stage movement is repeated until the stage reaches the maximum position, Vmax. The sequence for the R stage movement is repeated until the stage reaches the maximum position, Rmax. The spot detection diagram is depicted in Figure 5.12.

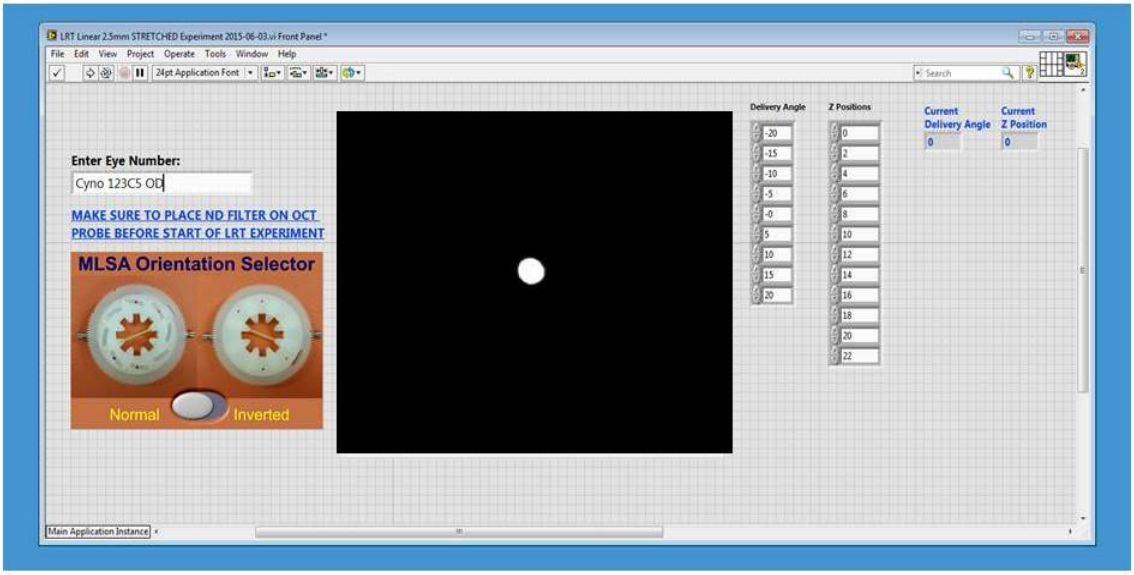


**Figure 5.11:** Screenshot of LabView program during an LRT experiment.

Custom software written in LabView was developed to automate the entire LRT experiment. The program displays the current delivery angle and camera position so the user can monitor the experiment progress. Figure 5.11 shows a screenshot of the LRT program.

The LRT program uses the following inputs from the user:

- Eye number
- mMLSA stretch position
- Number of delivery angles, $\alpha$, and degree increment, $\Delta\alpha$
- Range of heights, $z$, for image acquisition and height increment, $\Delta z$
- LRT scanning pattern: Linear, Raster, Meridional or Concentric
- LRT scanning pattern parameters (e.g. scan length, number of rays, etc.)

#### *5.5.2.2 Spot detection and centering*

The program stretches the tissue to the specified stretch position and performs a ray trace for each delivery angle set by the user. The LRT beam is first projected onto the crystalline lens with the scanners at the center position, and the camera is moved directly below the tissue chamber. An algorithm was developed to automatically locate the LRT beam. The algorithm starts with an initial guess for the horizontal position of the camera directly below the lens. The camera acquires images in real time and determines whether the beam is present by searching for a circle (spot) and calculating the centroid. If a spot is detected, the (X, Y) centroid position of the spot in pixels is equal to a value greater than zero and the software moves on to the next part of the program. However, if the camera does not detect a spot, the centroid position of the spot is set to (0, 0), and the horizontal position of the camera is varied in a feedback loop. The program runs the beam detection loop a maximum of 10 times before determining that no beam is present and saving an error message in a text file for that camera height. The diagram in Figure 5.12 shows the beam detection algorithm. The loop searches for the LRT beam and covers a horizontal length 50 mm before moving on to the next vertical position.

Once the spot is found, the beam is centered on the camera to maximize the imaging area for the LRT scan. The spot centering algorithm takes into account the current X-centroid position of the spot and finely adjusts the motorized horizontal positioning until the X-centroid falls within ± 15 pixels of the center pixel of the image sensor.

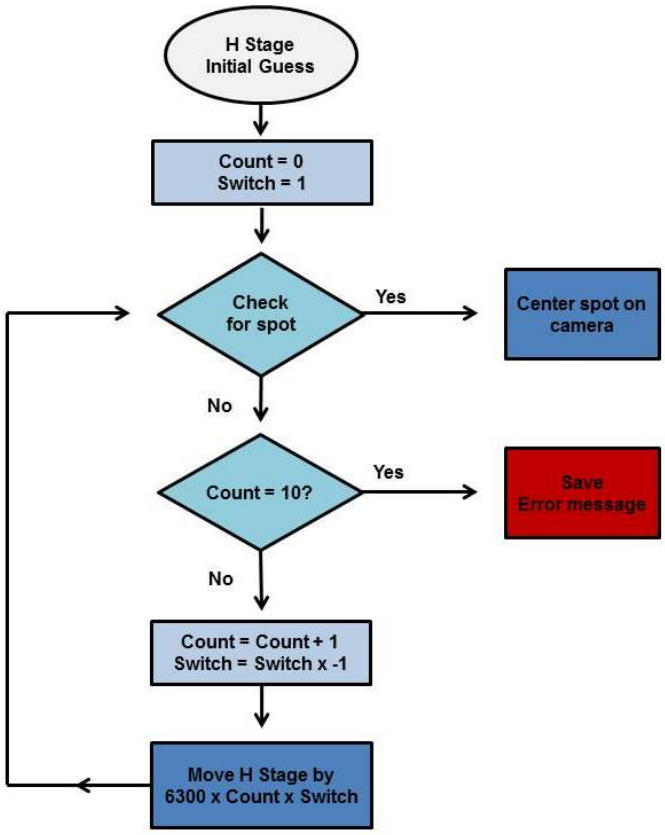


**Figure 5.12:** Beam detection algorithm for LRT program. The program starts with an initial guess for the horizontal (H) stage and checks to see if the beam is present. The program uses a switch (alternates between +1 and -1) and a counter. If the beam not present, the position of the camera mounted on the horizontal stage is moved relative to the current position by 6300 x counter x switch. The switch is multiplied by -1 and the count is increased by 1 each iteration. The spot detection loop is repeated until the beam is found, or a maximum of 10 iterations.

#### *5.5.2.3 LRT scanning and image acquisition*

Once the beam is centered on the camera, the LRT scanning sequence commences. The camera is synchronized with the galvanometer scanners to acquire an image for each individual ray position of the scanning pattern. The spot images of each ray are recorded and saved in a folder corresponding to the specific delivery angle and camera height position. The available scan patterns are linear, raster, meridional or

concentric, and are selected by the user at the start of the experiment. The individual scan patterns are discussed in greater detail in Section 5.6.6.

Once all of the images for the scanning sequence have been saved, the height of the camera is translated downwards by the specified height increment and the camera searches for the new beam position, centers the beam on the image sensor, and records an image for each individual ray of the scanning pattern. This process is repeated for the range of heights specified by the user. Once the scanning sequence is complete for the first delivery angle, the rotation stage is rotated by the specified degree increment and the entire process is repeated. The LRT program saves spot images for each height, and each delivery angle designated by user for a specific stretch position.

### *5.5.3 LRT image processing program*

A semi-automated program written in MATLAB was developed for post-processing of the LRT data. The program analyzes the spot images and calculates the centroid of each spot for all of the images (Figure 5.13, Top). The centroid positions are used as an estimate for the ray height incident on the camera.

As a first step, 2-D (linear) ray-trace data was analyzed similar to Chapter 4, where the program plots the measured spot heights as a function of entrance ray height. A plot is generated for each axial position of the camera and fit with a third-order polynomial (Figure 5.13, Bottom). The centroid positions and the coefficients of the third-order polynomial fits are exported to Excel and used to calculate the power and aberrations of the crystalline lens. In future applications, 3-D (raster) ray-trace data will be analyzed to measure the 2-D wavefront aberration maps of the crystalline lens.

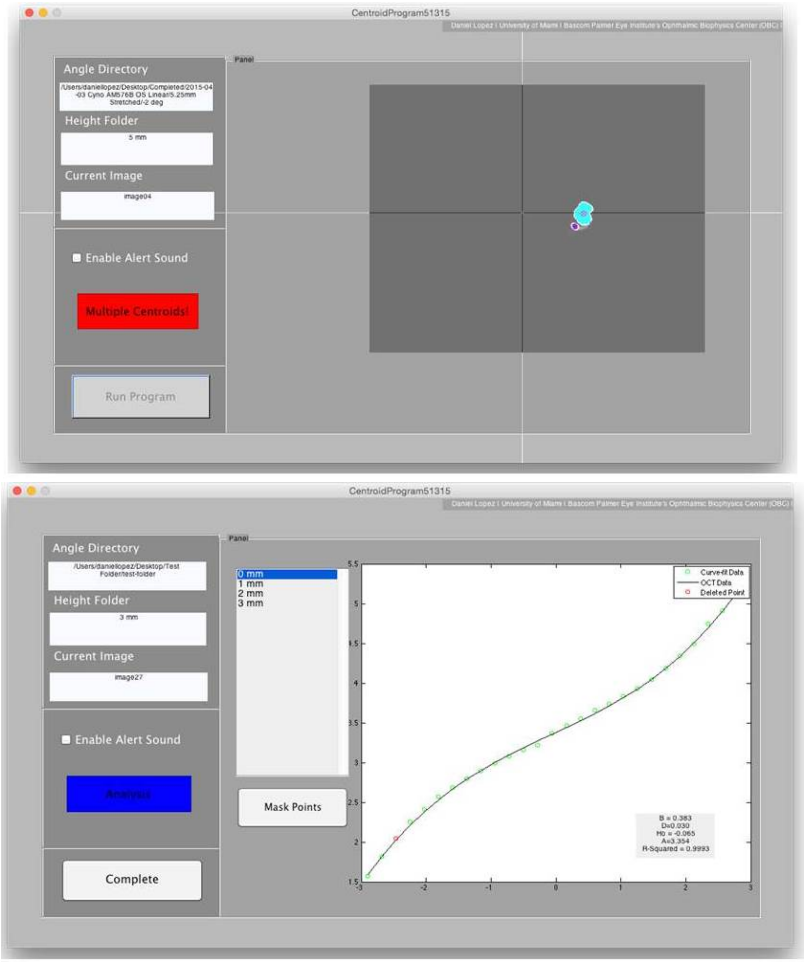


**Figure 5.13:** MATLAB program used to analyze the 2-D LRT images. (Top) The spot centroid detection user interface and (Bottom) the plotting and third-order polynomial fitting function.

## 5.6 Testing and validation

### *5.6.1 Lens centering and alignment*

Proper alignment of the crystalline lens in the LRT-OCT system is critical for acquiring reliable LRT measurements and OCT images. The crystalline lens must be positioned at the center (pivot point) of the rotation stage prior at the start of the experiment. The first step of the lens alignment protocol is to position the OCT beam on the crystalline lens by visualizing the horizontal and vertical OCT scans in real-time and adjusting the position of the tissue chamber (in the X-Y direction) until the anterior and posterior surfaces of the lens are centered in the OCT scans. Once the lens is centered in

the X-Y direction, the vertical height, Z, of the lens is adjusted by rotating the delivery optics to the -45° and +45° positions, and modifying the height of the tissue chamber until the lens is centered in the horizontal and vertical OCT scans as shown in Figure 5.14. Once the crystalline lens is properly aligned in the system, the LRT-OCT experiments may commence.

### *5.6.2 Pre-stretching tissue*

The importance of properly centering the crystalline lens in the LRT-OCT system was emphasized in the previous section. An inherent drawback of using a lens stretching system is that the lens translates upwards with stretching, which introduces the need for lens centering and alignment at different stretching positions throughout an experiment. The first few stretching steps (total displacement of < 1.50 mm) simply place the zonules under tension and do not produce significant changes in lens shape or power (Marussich et al., 2015). Therefore, these initial steps may be excluded from the LRT experiment and analysis.

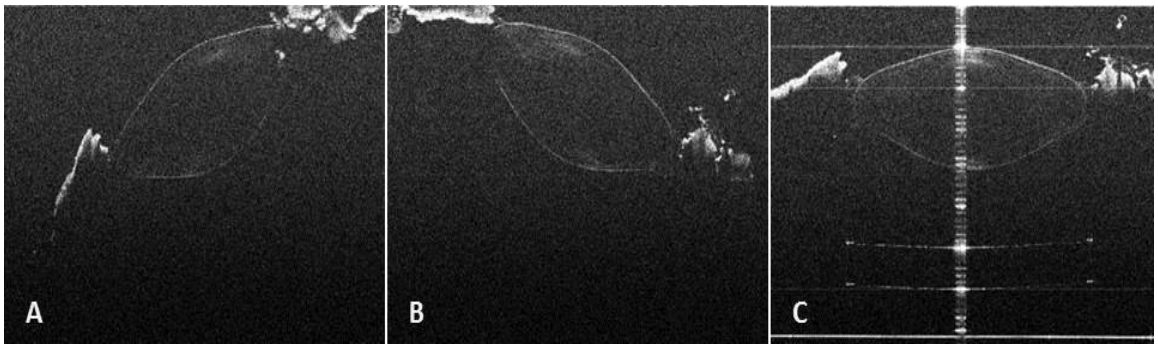


**Figure 5.14:** OCT images of an unstretched cynomolgus monkey lens (Age: 5.7 years, post-mortem time: 24 hours) acquired at A) -45°, B) +45° and C) 0° delivery angles.

LRT experiments were conducted to evaluate the effect of subsequent stretching steps on the lens position and determine whether there is a difference between the unstretched lens and the pre-stretched lens. Experiments were performed on 5 cynomolgus monkey lenses (Ages: 5.7-12.4 years; Post-mortem time: 33.6 ± 13.1 hours). Data were acquired on lenses in the unstretched state; then the tissue was "pre-stretched" and the experiments were repeated on the pre-stretched lens. The pre-stretched position was selected by stretching the tissue and determining where crystalline lens stopped moving upwards and began changing shape. The average pre-stretch position for the monkey lenses in this study was 2.5 mm. For the purposes of the pre-stretch study, only the on-axis (0 degrees) LRT data was analyzed.

The power and Zernike spherical aberration coefficients for lenses in the unstretched and pre-stretched state are shown in Table 5.4. The difference between the unstretched and pre-stretched lens power ranged from 0.99 to 4.42 D and spherical aberration ranged from 0.086 to 0.291 μm. The measurement variability may be due to the shift in lens position with pre-stretching. The size and age of the crystalline lens could also contribute to this difference. To take into account the variation between the unstretched and pre-stretched lens, the unstretched lens is scanned at 0º as a reference, the lens is pre-stretched and re-aligned in the system, and then the experimental protocol is performed on the pre-stretched lens and subsequent stretching positions. Tissue pre-stretching was implemented in the LRT-OCT experimental protocol as it eliminates the significant upward movement of the lens in the initial stretching steps, and the need for re-centering and aligning the lens during an LRT experiment.

### *5.6.3 Fluid level*

The tissue chamber is filled with balanced salt solution (BSS) to keep the tissue hydrated throughout the experiment. Due to the difference in refractive index at the fluid-air boundary, the fluid level creates a strong reflection line in the OCT image and influences the vertical position of the crystalline lens in the image. Therefore, it is essential that the fluid level remain constant throughout each OCT imaging experiment, and that a consistent fluid level be used for all the experiments.

Several tests were performed to determine the ideal fluid level which produces the best quality OCT image, and how to achieve a consistent fluid level for each experiment. Based on these experiments, a final protocol was developed which uses the BSS reflection line as a reference. The amount of fluid is gradually adjusted using a 10 mL syringe until the BSS reflection line coincides with the undistorted posterior window of the tissue chamber at the 11 mm mark (Figure 5.15).

| Eye | Power (D) | | Change in Power (D) | Z40 Aberration Coefficient (µm) | | Change in Power (D) |
|---|---|---|---|---|---|---|
| | Unstretched | Pre-Stretched | | Unstretched | Pre-Stretched | |
| **Cyno 9C59 OD** | 58.61 | 55.10 | 3.51 | -4.410 | -4.622 | -0.212 |
| **Cyno 4C105 OD** | 47.70 | 46.70 | 0.99 | -3.991 | -4.079 | -0.088 |
| **Cyno 54-1050 OD** | 50.28 | 45.86 | 4.42 | -3.914 | -3.076 | 0.838 |
| **Cyno 54-1050 OS** | 47.48 | 44.19 | 3.29 | -3.491 | -3.782 | -0.291 |
| **Cyno 7C101 OD** | 49.05 | 44.67 | 4.38 | -3.460 | -3.374 | 0.086 |

**Table 5.4:** Comparison of lens power and Zernike spherical aberration coefficients for cynomolgus monkey lenses in the unstretched and pre-stretched state. Ages ranged from 5.7 to 12.4 years.

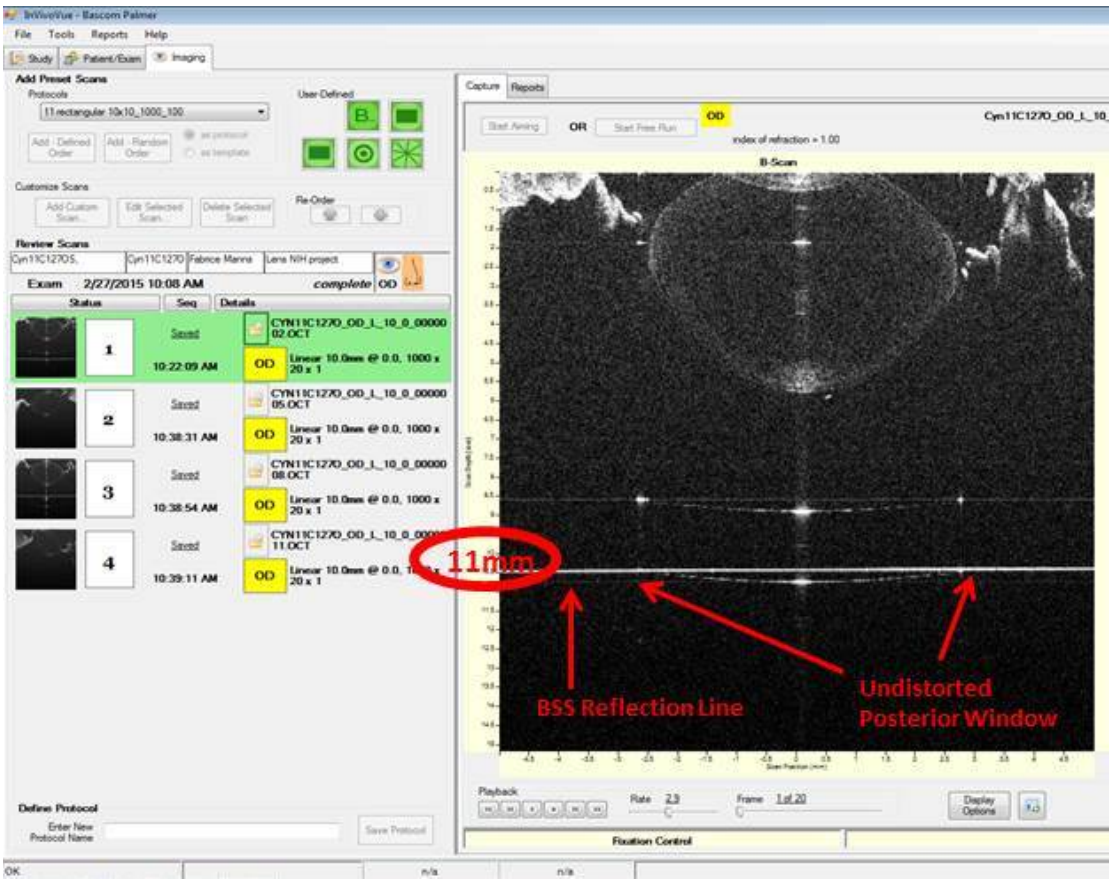


**Figure 5.15:** Screenshot of the Bioptigen InVivoVue software showing BSS reflection line coinciding with the posterior window of the tissue chamber at 11mm.

### *5.6.4 Beam attenuation*

The output power of the OCT beam through the sample arm fiber is ~0.6 mW, which is too powerful for the LRT camera and saturates the sensor. In order to image the beam, the beam must be attenuated. An 850 nm long-pass filter (FGL850, Ø25 mm RG850 Colored Glass Filter, Thorlabs, USA) was mounted on the camera to filter out ambient light, and an experiment was conducted to determine the optical density (OD) needed to sufficiently reduce the power of the beam to image it with the camera.

Absorbing neutral density (ND) filters were mounted on the delivery probe to attenuate the OCT beam. The ND filters were stacked to produce an OD ranging from 1.6 to 4.7. It is challenging to select a single value for all cases because the beam attenuation

also depends on the transparency and optical quality of the crystalline lens. LRT experiments were performed on both an isolated human lens and isolated cynomolgus monkey lens with varying optical densities to determine the optimal OD.

The OCT images were visually assessed to determine the best quality spot. Figure 5.16 shows the spot images recorded with neutral density filters of varying OD for a cynomolgus monkey and human lens. The ideal spot has a distinct boundary and is large enough to be detected by the MATLAB program to calculate the spot centroid. In the case of the under attenuated beam, the resulting spot does not have a clear boundary while the over attenuated beam produces a clearly defined spot in the central region but the spot is lost and cannot be visualized in the periphery. An optical density of 1.8 was chosen based on the spot images. Two ND filters of OD 1.5 (#63-392, 25mm Dia. Non-Reflective ND Filter, Edmund Optics, USA) and 0.3 (#63-406, 25mm Dia. Non-Reflective ND Filter, Edmund Optics, USA) were stacked and mounted on a removable magnetic cage mount (CP90F, 30 mm Removable Cage Plate, Thorlabs, USA). The magnetic mount allows the user to place the ND filters on the delivery probe prior to the start of the LRT experiment, and to remove the ND filters for OCT imaging.

### *5.6.5 Rotation stage homing*

Initially, the custom delivery probe was mounted on the motorized rotation stage so the "home" position of the stage corresponded with the probe being upright at 0º. An intrinsic property of the Zaber rotation stage homing mechanism is that the stage always rotates counter-clockwise to the home position. Therefore, if the rotation stage is homed when the stage is at a negative delivery angle (to the left of the home position), the stage will rotate the full 360 degrees back to home.

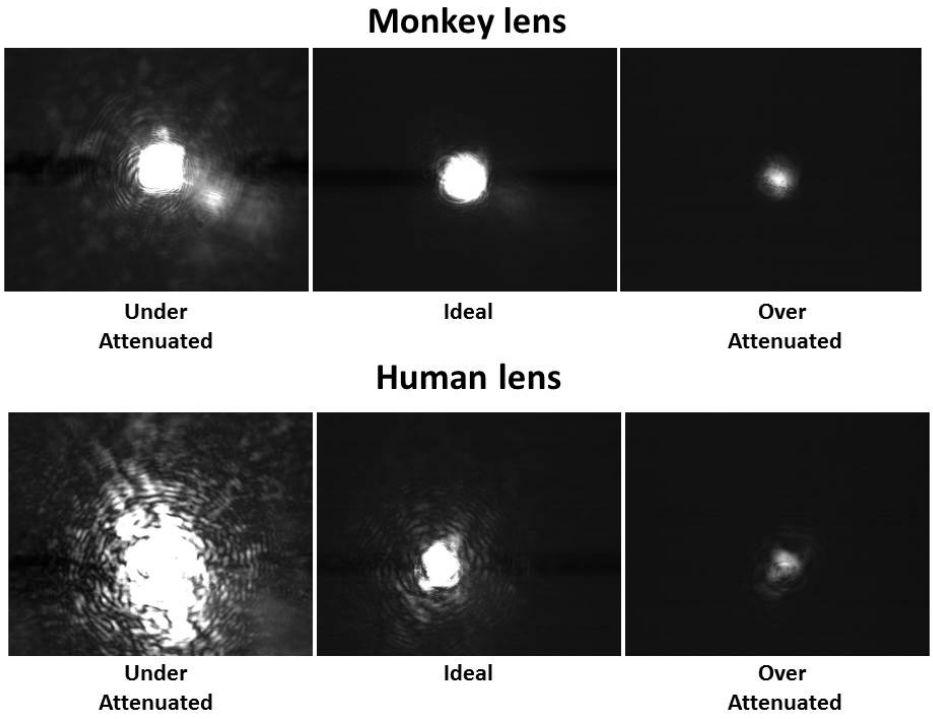


**Figure 5.16:** LRT spot images for imaged with neutral density filters of varying optical density depicting the spot quality for the under and over attenuated beam and the ideal case. (Top) Isolated cynomolgus monkey lens (Age = 5.92 years, PMT = 48 hours) and (Bottom) isolated human lens (Age = 57 years, PMT = 120 hours).

Due to delicacy of the OCT fiber and nearby components in the LRT-OCT system, this poses a serious risk to the fiber and cables which connect to the custom mount. Since the homing mechanism could not be modified, the delivery probe was mounted on the rotation stage at -45º. Since the maximum delivery angle for an LRT-OCT experiment is -45º, the delivery probe will never exceed the home position throughout an experiment and the risk of the probe rotating the full 360º and damaging the OCT fiber is avoided.

### *5.6.6 Calibration of LRT scan pattern*

Experiments were conducted on an empty cell (no lens was present) to calibrate the voltage (V) delivered to the galvanometer mirrors of the OCT probe to the ray height

(mm) incident on the crystalline lens. The calibration was performed by delivering equally-spaced rays in a linear pattern from 0.78 V to -0.18 V in 0.01 V increments (97 rays in total) corresponding to a scan length of 5.05 mm. The experiments were performed on-axis and in both the X and Y directions. An image was recorded for each individual ray and the images were processed in MATLAB to calculate the centroid positions for each spot.

Figure 5.17 shows the ray height versus voltage for the X and Y directions. The slope of the linear fit was used as the calibration factor. A calibration factor of 5.2673 mm/V was determined for the X direction and 5.2106 mm/V for the Y direction. The calibration factors were used to generate the LRT scanning patterns. Additional experiments were conducted to validate the linear, raster, circle and meridional scans. An example of a LRT circular scan with 11 rays, 3 mm diameter is shown in Figure 5.18.

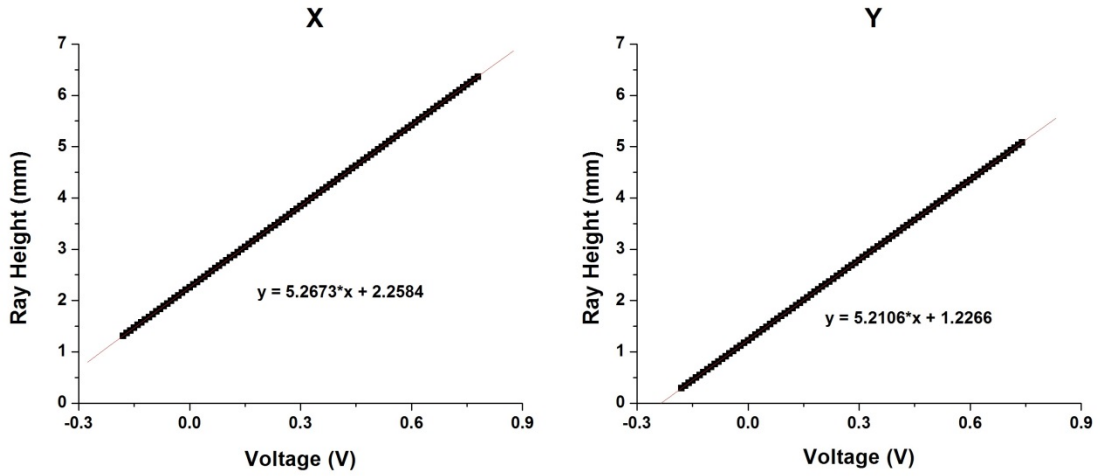


**Figure 5.17:** Ray height versus voltage plots in the X and Y directions. The linear fit is shown in red.

| Ray No. | X (mm) | Y (mm) |
|---|---|---|
| 1 | 1.823 | 1.823 |
| 2 | 2.109 | 2.109 |
| 3 | 2.858 | 2.858 |
| 4 | 3.784 | 3.784 |
| 5 | 4.532 | 4.532 |
| 6 | 4.818 | 4.818 |
| 7 | 4.532 | 4.532 |
| 8 | 3.784 | 3.784 |
| 9 | 2.858 | 2.858 |
| 10 | 2.109 | 2.109 |
| 11 | 1.823 | 1.823 |

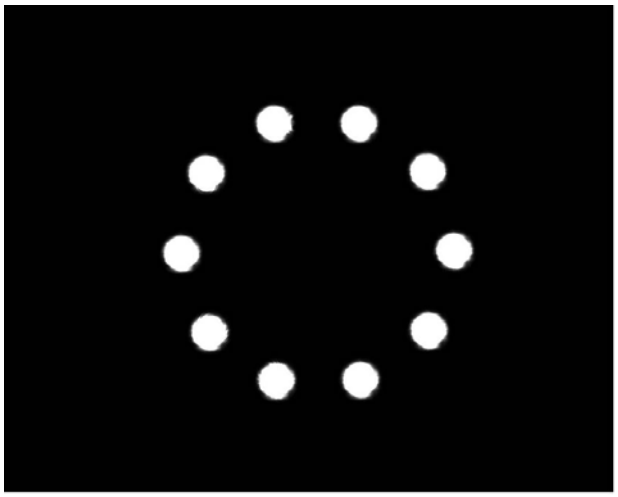

**Figure 5.18:** Example of a LRT circular scan with 11 rays and 3 mm diameter. (Left) Table showing the 11 spots and the (X, Y) positions on the camera. (Right) Superimposed image of the spots in circular scan.

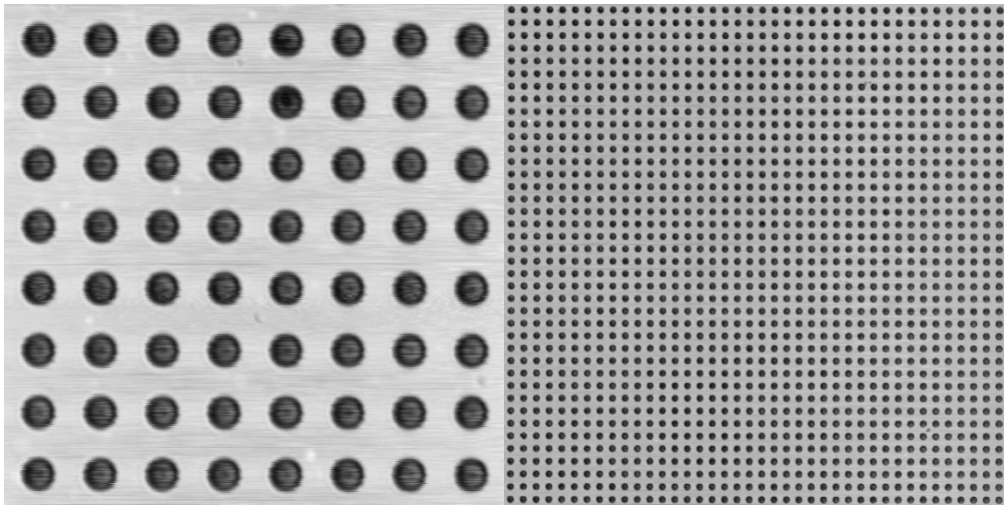

**Figure 5.19:** Top view images of the glass distortion target scanned with the custom designed beam delivery probe for scan lengths 3 x 3 mm (Left) and 10 x 10 mm (Right). These images were used to calibrate the Bioptigen InVivoVue *Ex Vivo* software.

### *5.6.7 Calibration of OCT scan head*

The Bioptigen InVivoVue *Ex Vivo* software was finely calibrated for the custom beam delivery probe using a glass distortion target (Fixed Frequency Grid Distortion Target #58-527, Edmund Optics, USA). The target has a grid of dots with a pattern size of 25 x 25 mm where each dot has a diameter of 0.125 mm and 0.25 mm dot spacing (center to center). 3-D Volume scans of the target were recorded with the *Ex Vivo* probe for scan sizes 2 x 2 mm, 3 x 3 mm, 4 x 4 mm, … up to 20 x 20 mm. pixels Sample top

view, or volume intensity projection (VIP), images for varying scan lengths are shown in Figure 5.19. The images recorded with 800 a-lines in the X and Y directions. Therefore, all of the images were 800 x 800 pixels.

The images were processed in MATLAB to determine the positions of the dot centroids. The difference between the centroid positions for adjacent dots was used to calculate the actual scan length, *SL*, for each image based on the following equation:

$$SL = 800\ px * \frac{0.25\ mm}{\Delta C} \qquad \text{(Eq. 5.1)}$$

where 0.25 mm is the dot spacing and $\Delta C$ is the difference between X or Y centroids of adjacent dots on the target.

The parameters in the Bioptigen InVivoVue *Ex Vivo* software were modified so that the X and Y scan lengths corresponded to the proper image scan length. For instance, the 14 x 14 mm scan length in the Bioptigen InVivoVue *Ex Vivo* software corresponds to 13.95 mm in the X direction and 13.94 mm in the Y direction. The Bioptigen software automatically saves the actual scan length values in a text file for each data set for image post-processing.

### *5.6.8 Camera height range and increments*

During an LRT experiment, images are recorded at camera heights ranging from 0 to 20 mm, where 0 mm corresponds to the top of the motorized vertical positioning stage and the camera is moved 20 mm downwards. A maximum range of 20 mm was selected because the LRT beam becomes defocused (as discussed in Section 4.6), which reduces the quality of the spot images and the precision of the centroid calculation.

An analysis was performed to determine the optimal height increment (in mm) for the camera to accurately measure lens power and aberrations while minimizing the number of images recorded per eye. LRT experiments were performed on two cynomolgus monkey lenses (unstretched and stretched) for delivery angles ranging from 20º to -20º degrees using 1 mm camera height increments. The LRT images were processed in MATLAB and the lens power was calculated for each delivery angle.

The lens power was then recalculated using the LRT data for every 2 mm, 3 mm, 4 mm and 5 mm position. The error difference from the standard 1 mm height increment was calculated for each new camera height interval. The lens power measured for camera height increments of 1 to 5 mm are shown in Figure 5.20. Recording LRT images using height increments from 2 to 5 mm produced a maximum error of 2.5% in the lens power measurement. Based on these results, an ideal camera height increment of 3 mm was selected for LRT experiments, corresponding to a total of 8 positions over a z-range of 0 to 21 mm.

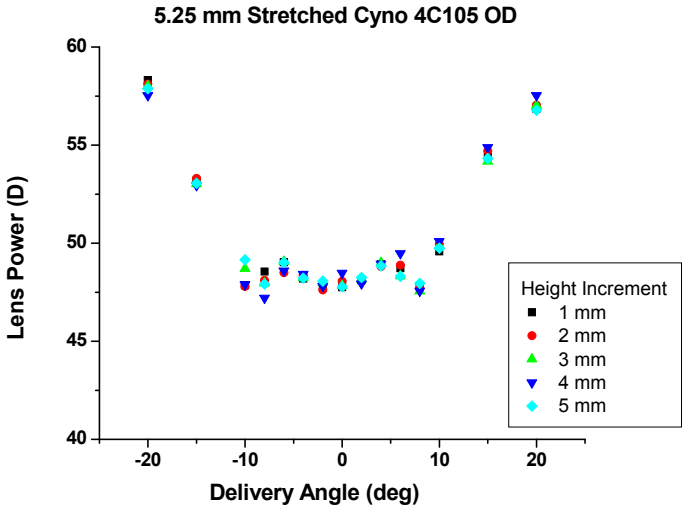


**Figure 5.20:** Unstretched cynomolgus monkey lens power plotted with respect to delivery incidence angle for camera height increments ranging from 1 to 5 mm.

| Edmund Optics Lens Focal Length (mm) | Measured Lens Focal Length (mm) | Edmund Optics Lens Power (D) | Measured Lens Power (D) | Lens Power Measurement Error | Difference in Lens Power (D) |
|---|---|---|---|---|---|
| 12 | 11.81 | 83.33 | 84.65 | -1.58% | -1.32 |
| 15 | 15.07 | 66.67 | 66.37 | 0.45% | 0.30 |
| 18 | 18.53 | 55.56 | 53.98 | 2.84% | 1.58 |
| 24 | 24.30 | 41.67 | 41.16 | 1.23% | 0.51 |
| 36 | 36.94 | 27.78 | 27.07 | 2.55% | 0.71 |
| 42 | 42.61 | 23.81 | 23.47 | 1.43% | 0.34 |
| 48 | 48.98 | 20.83 | 20.42 | 1.99% | 0.42 |
| 54 | 54.34 | 18.52 | 18.40 | 0.62% | 0.12 |
| 60 | 60.91 | 16.67 | 16.42 | 1.50% | 0.25 |
| 72 | 72.70 | 13.89 | 13.76 | 0.96% | 0.13 |

**Table 5.5:** Focal length and power measurements for glass calibration lenses obtained with the LRT system.

### *5.6.9 Lens power measurements*

The power measurements obtained with the LRT system were validated using glass lenses from a calibration set (#48-161, 12mm Diameter VIS 0° Coated Plano-Convex Lens Kit, Edmund Optics, USA). LRT experiments were performed on glass calibration lenses (in air) with focal lengths ranging from 12 to 72 mm to determine the accuracy and precision of the power measurements.

The glass lenses were placed on a rubber O-ring in the LRT tissue chamber. The lens was centered and aligned in the system, and a ray trace was performed by sequentially delivering 27 equally-spaced parallel rays along one meridian of the lens over the central 5.5 mm optical zone. The LabView software developed in Section 5.5.2 was used to acquire LRT data for each lens at 0° for multiple camera heights, ranging from 0 to 15 mm in 1 mm increments. The focal length and power measurements for the glass calibration lenses are shown in Table 5.5. The difference between the actual lens power and the power measured with the LRT system were within 0.30 ± 0.71 D.

## 5.7 Summary

In conclusion, the LRT system described in Chapter 4 was enhanced to allow on-axis and off-axis measurements of power and 2-D wavefront aberration maps of the crystalline lens. The beam delivery optics were mounted on a motorized rotation stage that pivots around the crystalline lens to allow acquisition of off-axis spot patterns. A camera mounted on a horizontal and vertical motorized positioning stage was used to record the spot positions along each individual ray below the lens for all delivery angles. In the next chapter, the enhanced LRT-OCT system will be used to measure the on-axis and off-axis power of the crystalline lens in the accommodated (unstretched) and relaxed (stretched) states. Off-axis lens power measurements will be used to characterize the changes in lens power with field angle and to study how accommodation impacts these changes.

# CHAPTER 6

# ACCOMMODATIVE CHANGES IN CRYSTALLINE LENS OFF-AXIS POWER

## 6.1 Purpose

In this chapter, the experiments related to Aim 3 of the project are described. Laser ray tracing experiments were performed on cynomolgus monkey lenses to measure the changes in lens off-axis power with accommodation using the system developed in Chapter 5. The purpose is to quantify the changes in lens power with varying incidence angle for lenses in the accommodated (unstretched) and relaxed (fully stretched) states. This information will help us to better understand the contribution of the crystalline lens to the peripheral optical performance of the whole eye.

## 6.2 Background and significance

In recent years, there has been considerable interest in studying the peripheral (off-axis) optics of the human eye. Peripheral vision plays an important role in the detection of stationary and moving objects, and is critical for navigation in dimly lit settings (Atchison, 2012; Burnat, 2015). Peripheral vision may effect central refractive development; therefore, it is important to understand how optical defocus across the entire visual field influences the development of peripheral refractive error and ocular shape. In humans (Millodot, 1981; Seidemann et al., 2002; Atchison et al., 2005) and rhesus monkeys (Huang et al., 2009), spherical-equivalent refractive errors were shown to vary considerably with eccentricity (i.e. towards the periphery).

The optics related to the periphery of the visual field, including peripheral refraction and off-axis aberrations, are associated with refractive error (Smith EL et al., 2010; Smith EL et al., 2009; Smith EL et al., 2005). Studies have also demonstrated that peripheral refraction influences the onset and progression of myopia in humans (Whatham et al., 2009; Smith EL, 2011; Rosen, Lundstrom & Unsbo, 2012). Standard treatments for myopia correction including traditional spectacles or contact lenses correct for defocus of the retinal image at the fovea. However, a majority of the retina, particularly the periphery, experiences hyperopic defocus which stimulates axial eye growth and leads to an increase the rate of myopia progression.

Peripheral optical treatments strategies (Figure 6.1) have been recently proposed as a novel method for correcting and slowly the progression of myopia. The primary goal of peripheral treatment strategies is to provide optimal vision in the central and peripheral region by manipulating the curvature of field of the image shell (Smith EL, 2011). This treatment method would provide an in-focus image at both the fovea and peripheral retinal, and would reduce the peripheral visual signals that stimulate axial eye growth thus slowing the rate of myopia progression.

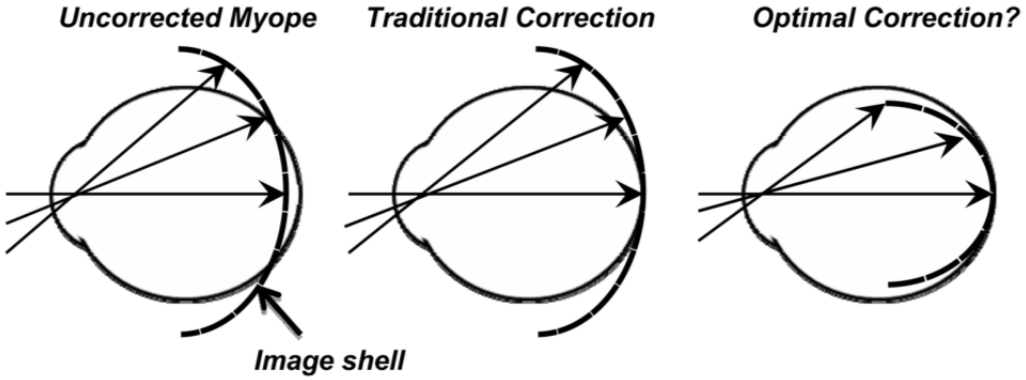


**Figure 6.1:** Schematic of the goal for peripheral treatment strategies to slow myopia progression. The left side shows the image shell for a distant object for a typical unaccommodated myopic eye. The center shows traditional correction where the foveal image is in focus, but there is relative hyperopia in the retinal periphery. The right side shows the fundamental goal of peripheral treatment strategies which is to provide optimal central vision and produce visual signals that normally reduce axial growth (Smith EL, 2011).

Despite its importance to ocular growth and myopia development, little is known about the peripheral optics of the eye and its effect on visual performance. Studies have shown that accommodation (Mathur, Atchison & Charman, 2009) and age (Atchison et al., 2005) influence peripheral refraction. The crystalline lens plays a significant role in our eye's ability to accommodate. The optical properties of the crystalline lens, particularly the gradient refractive index, are also shown to change with age (Augusteyn, Jones & Pope, 2008; Jones et al., 2005; Moffat, Atchison & Pope, 2002). Therefore, one would expect that changes in the optics of the crystalline lens would contribute to changes in the peripheral optics of the whole eye.

It is challenging to directly measurement the off-axis power of the crystalline lens *in vivo* due to the lens' position behind the cornea and iris. *Ex vivo* lens stretching systems (Glasser & Campbell, 1998; Roorda & Glasser, 2004; Manns et al., 2007; Ehrmann, Ho & Parel, 2008; Augusteyn et al., 2011) have enabled the direct measurement of crystalline lens power, aberrations and shape with simulated accommodation. To our knowledge, no studies have reported direct measurements of lens peripheral (off-axis) power. Off-axis power measurements of the lens could provide further insights into the potential role of the crystalline lens in the peripheral optics of the whole eye.

The purpose of this study was to demonstrate the feasibility of measuring the off-axis power of the crystalline lenses using the combined laser ray tracing (LRT) and optical coherence tomography (OCT) system developed in Chapter 5. Off-axis lens power measurements were obtained for lenses mounted in a lens stretcher in the relaxed

and accommodated states to characterize the changes in lens power with field angle and study how accommodation impacts these changes.

## 6.3 Experiments

### *6.3.1 Donor tissue*

Data were acquired on 13 lenses from 8 cynomolgus monkey eyes obtained as part of a tissue-sharing protocol (age: 5.7-12.4 years, post-mortem time: 37±17 hours). All experiments adhered to the Association for Research in Vision and Ophthalmology Statement for the Use of Animals in Ophthalmic and Visual Research. The eyes were obtained from the Division of Veterinary Resources at the University of Miami as part of a tissue-sharing protocol and were used in accordance with Institutional Animal Care and Use Guidelines. The eyes were enucleated immediately after euthanasia, wrapped in gauze, and stored in a closed container. No animals were euthanized for the sole purpose of this study. Upon arrival at the laboratory, all eyes were either prepared for LRT-OCT experiments or refrigerated at 4°C (Nankivil *et al.* 2009).

### *6.3.2 Tissue preparation*

The tissue dissection followed the same protocol described in Section 3.3.2. To summarize, the whole globe was bonded to eight scleral shoes which were assembled in the miniature motorized lens stretching apparatus (mMLSA). Next, the posterior pole, cornea and iris were removed. Incisions were made in between the sclera of adjacent shoes to create eight independent segments for stretching. Following the dissection, the mMLSA containing the prepared tissue was inserted in the tissue chamber which was

placed in the LRT-OCT system. The tissue chamber was filled with balanced salt solution (BSS) so the mMLSA was fully submersed and the tissue remained hydrated throughout the experiment. A consistent fluid level was used for all experiments in this study (Refer to Section 5.6.3).

### *6.3.3 Experimental setup*

The OCT system was used to align and center the crystalline lens in the LRT-OCT system. The center of the crystalline lens was positioned at the center (pivot point) of the rotation stage prior at the start of the experiment to acquire useful LRT measurements and OCT images. The OCT beam was positioned on the crystalline lens apex prior to start of the experiments by visualizing the horizontal and vertical OCT scans in real-time, and adjusting the position of the tissue chamber (in the X-Y direction) until the anterior and posterior lens surfaces were centered in the OCT scans. Afterwards, the vertical height, Z, of the crystalline lens was adjusted by rotating the OCT delivery probe to the -45° and +45° positions, and modifying the height of the tissue chamber so that the lens was centered in the horizontal and vertical OCT scans as described in Section 5.6.1.

### *6.3.4 Laser ray tracing experiments*

Once the crystalline lens was properly aligned in the system, LRT experiments were performed on the lens in the unstretched state. Following the completion of the unstretched lens experiments, the tissue was stretched to the 5.25 mm position, the tissue alignment protocol was repeated, and LRT experiments were performed on the lens in the

stretched state. The LRT system performed a ray trace by sequentially delivering 27 equally-spaced parallel rays along one meridian of the lens over the central 5.5 mm optical zone. The LabView software developed in Chapter 5 was used to obtain LRT data for delivery angles ranging from -20° to +20° (in air), in 2° or 5° increments.

A motorized camera was positioned directly below the tissue chamber to capture a series of images from the position closest to the crystalline lens all the way at the lens focus. The travel range of the vertical stage is approximately equal to the focal length of the crystalline lens. The LRT system was programmed to automatically find the beam at off-axis delivery angles by adjusting the horizontal position of the camera. Spot images were acquired at multiple axial positions along the optical axis covering a vertical range of up to 20 mm for all delivery angles.

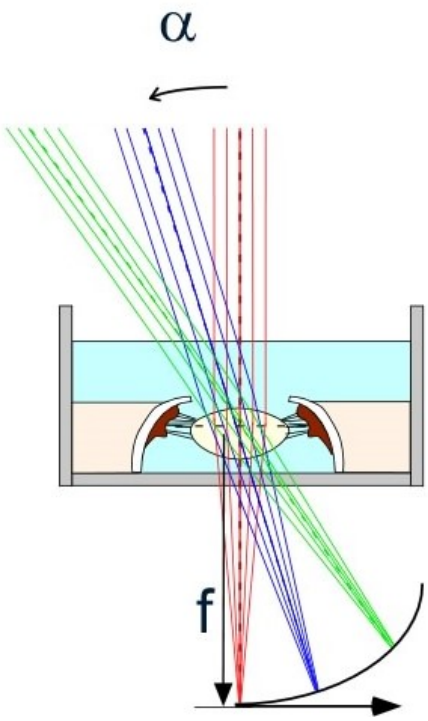


**Figure 6.2** Basic schematic showing the incidence rays entering the crystalline lens at varying delivery angles, α. The rays pass through the crystalline lens and are focused in the image plane at the lens focal point, *f*.

### *6.3.5 Data analysis*

The methodology used to calculate lens power is described in Chapter 4 (Refer to Sections 4.3.3 and 4.3.4). In summary, a MATLAB program (Mathworks, Natick, MA, USA) was used to calculate the centroid of each spot for all the images. The centroid position was used as an estimate for the ray height incident on the camera. The measured ray height was plotted as a function of entrance ray height, and fit with a third-order polynomial. The coefficients of the fit were used to calculate the optical power, $P$, of the crystalline lens for each delivery incidence angle, $\alpha$. The change in lens power from the on-axis (0°) position was calculated for each respective angle, where $\Delta P = P(0°) - P(\alpha)$. The change in lens power, or peripheral defocus, was calculated for lenses in the unstretched and stretched positions.

Figure 6.2 shows a basic schematic of the incidence rays entering the crystalline lens at varying delivery angles and being focused in the image plane. The change in lens power with respect to delivery angle was plotted for all of the eyes in this study. The plots for the unstretched and stretched lens were compared.

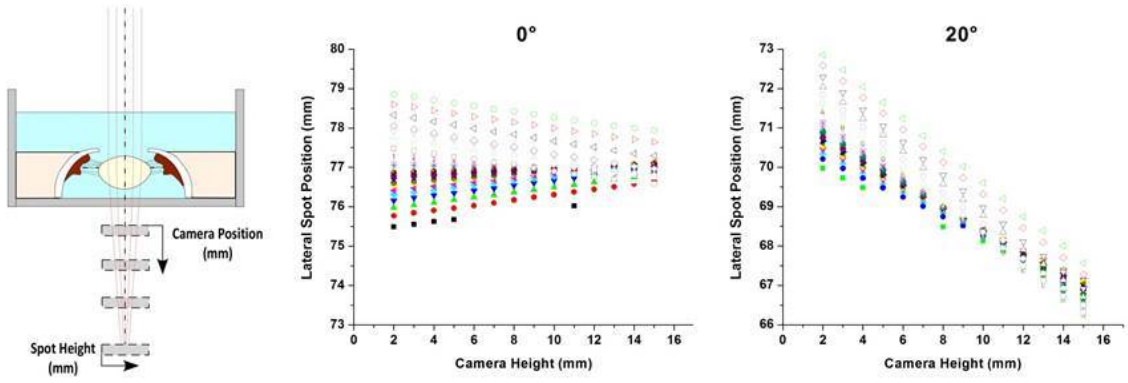


**Figure 6.3:** (Left) Basic schematic of spot image acquisition. Discrete points along each ray are shown at 0° (Center) and (Right) 20° delivery angles for a typical unstretched cynomolgus monkey lens (Age: 6.3 years, Post-mortem time: 24 hours). The spot heights correspond to the lateral position of the camera (in mm) on the motorized horizontal positioning stage and vary based on the delivery angle of the incidence rays.

## 6.4 Results

### *6.4.1 Typical results*

Figure 6.3 shows the measured spot positions along the individual rays at 0° and 20° incidence angles for a typical unstretched monkey lens. The spot positions correspond to the lateral position of the camera (in mm) on the horizontal positioning stage and the camera height (in mm) is the position of the camera on the vertical positioning stage (where 0 mm is the highest position of the stage and the camera is translating downwards). The spot positions vary based on the delivery angle of the incidence rays. The central rays appear to converge at the focal point of the lens which corresponds to 9 mm at 0° and 7 mm at 20° on the vertical stage. These focal points are equivalent to a lens focal length of 31.2 mm at 0° and 25.1 mm at 20°. Figure 6.4 shows the typical LRT and OCT results for an unstretched cynomolgus monkey lens.

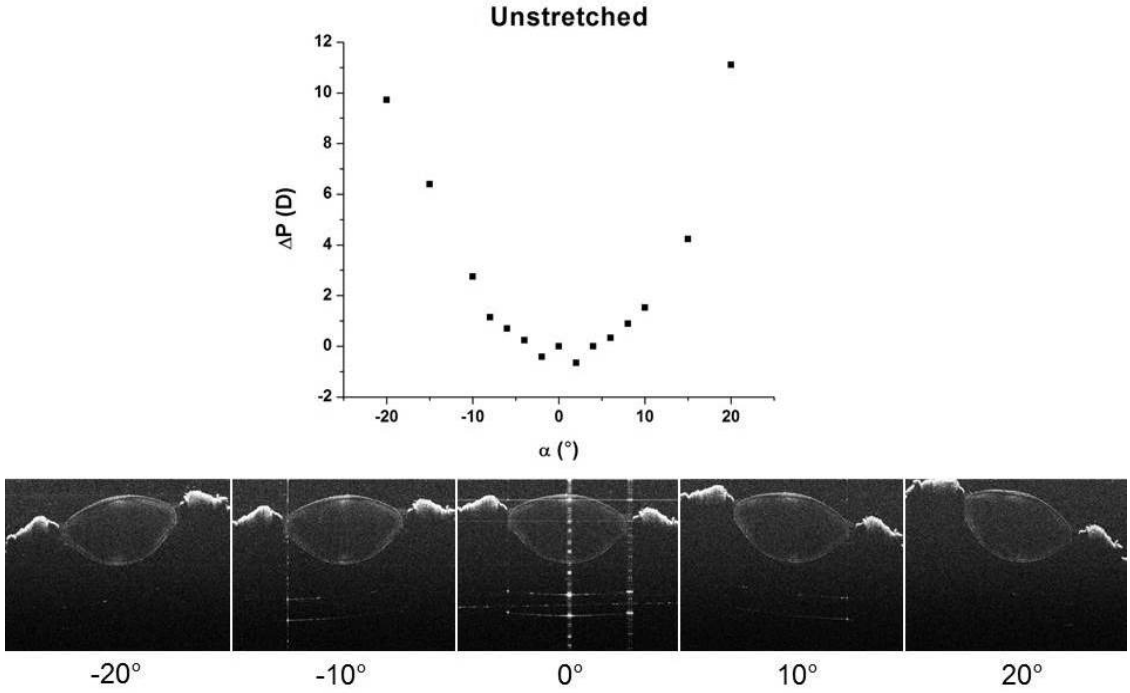


**Figure 6.4:** Typical result for an LRT-OCT experiment. (Top) The change in lens power versus incidence angle for a typical unstretched cynomolgus monkey lens (Age: 9.2 years, Post-mortem time: 24 hours). A fourth-order polynomial fit was performed on the plot. (Bottom) OCT images of the crystalline lens acquired at varying delivery angles ranging from -20º to +20º.

### *6.4.2 Change in lens power vs. incidence angle*

The change in lens power was plotted with respect to delivery incidence angle for all of the lenses in this study. Typical plots for lenses in the unstretched and stretched state are shown in Figures 6.5 and 6.6. The data was fit with a modified second-order polynomial:

$$P = P_0 + B*(\alpha - \alpha_0)^2 \qquad \text{(Eq. 6.1)}$$

where $P_0$ is a constant term [D], $B$ [D/(º)$^{-2}$] is a constant coefficient, $\alpha$ is the incidence angle [º], and $\alpha_0$ is an offset that accounts for decentration from 0º [º].

On average, the on-axis lens power was 52.0 ± 4.4D in the unstretched state and 32.7 ± 6.1D in the stretched state. In both unstretched and stretched states, the peripheral defocus was found to increase with increasing incidence angle. The peripheral defocus at 5°, 10°, 15° and 20° for lenses in the unstretched and stretched state are shown in Table 6.1.

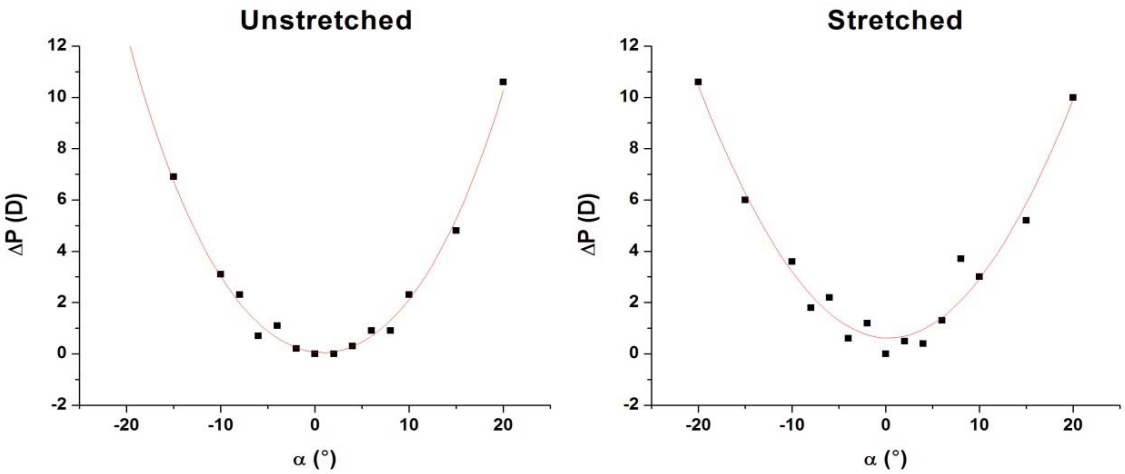


**Figure 6.5:** The change in lens power versus incidence angle for a cynomolgus monkey lens (Age: 5.7 years, Post-mortem time: 24 hours) in the (Left) unstretched and (Right) stretched states. A second-order polynomial fit was performed on each plot (shown in red) where unstretched: $P_0$ = -0.106 D, $\alpha_0$ = 0.914º, $B$ = 0.028 D/(º)$^{-2}$, and stretched: $P_0$ = 0.641D, $\alpha_0$ = 0.277º, $B$ = 0.024 D/(º)$^{-2}$.

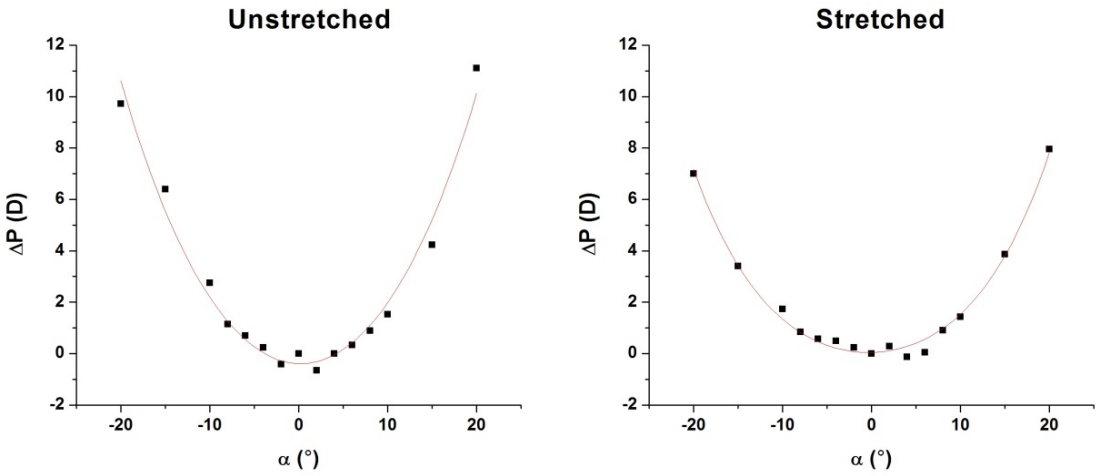


**Figure 6.6:** The change in lens power versus incidence angle for a cynomolgus monkey lens (Age: 9.2 years, Post-mortem time: 24 hours) in the (Left) unstretched and (Right) stretched states. A second-order polynomial fit was performed on each plot (shown in red) where unstretched: $P_0$ = -0.493 D, $\alpha_0$ = 0.293º, $B$ = 0.027 D/(º)$^{-2}$, and stretched: $P_0$ = -0.1876 D, $\alpha_0$ = -0.289º, $B$ =0.019 D/(º)$^{-2}$.

| | Peripheral defocus (D) | |
|---|---|---|
| | **Unstretched** | **Stretched** |
| **5º** | 0.2 ± 1.8 D | -0.7 ± 1.6 D |
| **10º** | 1.3 ± 2.2 D | 1.2 ± 1.3 D |
| **15º** | 4.0 ± 2.2 D | 3.0 ± 1.8 D |
| **20º** | 9.8 ± 1.6 D | 7.5 ± 2.8 D |

**Table 6.1:** Peripheral defocus, or change in lens power, with varying incidence angle.

## 6.5 Discussion

This study demonstrated the feasibility of acquiring on-axis and off-axis ray trace measurements of the crystalline lens using the combined LRT-OCT system. The system can be used to directly measure the changes in lens off-axis power during simulated accommodation in a lens stretcher. The unstretched and stretched lens power was found to increase peripherally (with increasing incidence angle) in all lenses in this study. The stretched lens showed a decreased variation in power across the visual field. These results suggest that accommodation changes the peripheral defocus of the lens and that the lens significantly contributes to the peripheral optical performance of the whole eye.

Future work will involve comparing the behavior of the natural crystalline lens which contains a gradient refractive index, with a lens containing a uniform refractive index, by modelling a cynomolgus monkey lens in the optical design program, OSLO (Optics Software for Layout and Optimization). The values for the lens shape (thickness, anterior and posterior surface radii of curvature) and the lens refractive index will be assumed for typical 5-year-old cynomolgus monkey lens. The peripheral defocus for a lens with and without the gradient refractive index will be compared. The data obtained with the LRT-OCT system can be used to improve current lens models by incorporating measurements of the lens shape and the changes in lens off-axis power and aberrations to predict the changes in the lens shape, power and aberrations with accommodation and age.

## 6.6 Summary

There has been significant interest in studying the peripheral optics of the eye due to its potential influence in refractive error development. There is some evidence that changes in the crystalline lens with age or accommodation affect peripheral defocus. The purpose of this study was to quantify the change in lens power (peripheral defocus) of the crystalline lens and its changes during simulated accommodation in a lens stretcher. The combined LRT-OCT system was used to measure the on-axis and off-axis ray trace of the crystalline lens. Lens power was found to increase peripherally with increasing incidence angle in cynomolgus monkey lenses.

# CHAPTER 7

## SUMMARY

The goal of this dissertation project was to gain a better understanding of the relationship between the crystalline lens shape, its gradient refractive index, optical power and aberrations, and how each of these parameters vary with accommodation and age. The growing lens poses a difficult challenge because its optical and mechanical properties produce changes in the optical power and higher-order aberrations which impact refractive development and the optics of the eye. In order to optimize vision correction procedures, we need to understand of how changes in the gradient refractive index affect the power and spherical aberrations of the lens and the whole eye.

The purpose of the first aim was to determine the contribution of the gradient to the change in lens power with accommodation. A lens stretching system was used to perform simulated accommodation experiments on post-mortem lenses. The changes in lens optical power, thickness and shape were quantified to determine the contribution of the gradient refractive index to the accommodative amplitude. The gradient was found to contribute approximately 65% of the total lens power change during accommodation for cynomolgus monkeys and 66% for hamadryas baboons, assuming an outer cortex refractive index of 1.365. The relative contribution of the gradient remains constant with accommodation. These findings show that accommodation-dependent optical models of the lens can assume a constant equivalent refractive index. They also suggest that a material of uniform refractive index could serve as a lens substitute for lens refilling procedures to restore accommodation.

The objective of the second aim was to measure the contribution of the gradient refractive index to lens spherical aberration. A laser ray tracing (LRT) system was used to obtain direct measurements lens effective power and spherical aberration in non-human primate lenses. This study produced results which were in very good agreement with the results obtained from numerical ray-tracing based on an optical model of the same lens with a reconstructed gradient refractive index produced from OCT images. The data showed that spherical aberration is negative in cynomolgus monkey lenses, and that spherical aberration becomes more negative with accommodation and becomes less negative with age. The experiments demonstrated the feasibility of directly measuring the changes in lens power and spherical aberration during simulated accommodation using an LRT system with a translating imaging sensor.

The final aim of the project involved designing and building an enhanced LRT system combined with an optical coherence tomography (OCT) system to measure changes in lens power, spherical aberration and shape with simulated accommodation, both on-axis and off-axis, as well as the 2-D wavefront aberration maps of the crystalline lens. The beam delivery optics were mounted on a motorized rotation stage that pivots around the crystalline lens to allow acquisition of off-axis spot patterns. An imaging sensor mounted on a two-dimensional motorized positioning stage below the lens was used to record the spot positions along each individual ray for all delivery angles.

The first application of the LRT system was to measure the changes on-axis and off-axis power of the lens during simulated accommodation in a lens stretcher. The unstretched and stretched lens power was found to increase peripherally (with increasing incidence angle) in all lenses. Lens stretching decreased the variation in power across the

field. These results suggest that accommodation changes the peripheral defocus of the lens and that the lens significantly contributes to the peripheral optical performance of the whole eye.

The combined LRT-OCT system will be used to measure on-axis and off-axis lens power and 2-D wavefront aberration maps of crystalline lenses. This work will be extended to human lenses. Future studies will investigate the changes in the 2-D wavefront aberrations to explore how aberrations of the lens vary along different meridians and the astigmatism of the lens. The system will acquire off-axis 3-D OCT images of the crystalline lens to reconstruct the lens gradient refractive index. Finally, the LRT-OCT data will be used to improve models of the lens by incorporating measurements of the lens shape and the changes in lens off-axis power and aberrations to more accurately predict the changes in the lens with accommodation and age.

## WORKS CITED


Artal P, Berrio E, Guirao A, Piers P. Contribution of the cornea and internal surfaces to the change of ocular aberrations with age. *Journal of the Optical Society of America.*2002;19(1):137-143.

Atchison DA. Accommodation and presbyopia. *Ophthalmic Physiol Opt*. 1995;15(4):255-272.

Atchison DA. The Glenn A. Fry Award Lecture 2011: Peripheral optics of the human eye. *Optometry and Vision Science.* 2012;89(7):954-966.

Atchison DA, Collins MJ, Wildsoet CF, Christensen J, Waterworth MD. Measurement of monochromatic ocular aberrations of human eyes as a function of accommodation by the howland aberroscope technique. *Vision Research*. 1995; 35(3):313-333.

Atchison DA, Pritchard N, White SD, Griffiths AM. Influence of age on peripheral refraction. *Vison Research*. 2005;45(6):715–720.

Atchison DA, Smith G. Optics of the human eye. *Oxford: Butterworth-Heinemann*. Oxford, UK. 2000;21-29.

Atchison DA, Smith G. Chromatic dispersions of the ocular media of human eyes. *Journal of the Optical Society of America.* 2005;22(1):29–37.

Augusteyn RC. Growth of the lens: in vitro observations. *Clinical and Experimental Optometry*. 2008;91(3):226–239.

Augusteyn RC. On the growth and internal structure of the human lens. *Experimental Eye Research*. 2010; 90(6):643-654.

Augusteyn RC, Jones CE, Pope JM. Age-related development of a refractive index plateau in the human lens: evidence for a distinct nucleus. *Clinical and Experimental Optometry*. 2008;91(3):296-301.

Augusteyn RC, Mohamed A, Nankivil D, Veerendranath P, Arrieta E, Taneja M, Manns F, Ho A, Parel JM. Age-dependence of the optomechanical responses of ex vivo human lenses from India and the USA, and the force required to produce these in a lens stretcher: the similarity to in vivo disaccommodation. *Vision Research*. 2011;51(14):1667–1678.

Augusteyn RC, Nankivil D, Mohamed A, Maceo B, Pierre F, Parel J-M. Human ocular biometry. *Experimental Eye Research*. 2012;102:70-75.

Birkenfeld J, de Castro A, Ortiz S, Pascual D, Marcos S. Contribution of the gradient refractive index and shape to the crystalline lens spherical aberration and astigmatism. *Vision Research.* 2013;86:27–34.

Bito LZ, DeRousseau CJ, Kaufman PL, Bito JW. Age-dependent loss of accommodative amplitude in rhesus monkeys: an animal model for presbyopia. *Investigative Ophthalmology and Visual Science.* 1982;23(1):23-31.

Borja D, Manns F, Ho A, Ziebarth N, Rosen AM., Jain R, Amelinckx A, Arrieta E, Augusteyn RC, Parel J-M. Optical power of the isolated human crystalline lens. *Investigative Ophthalmology and Visual Science*. 2008;49(6):2541–2548.

Borja D, Manns F, Ho A, Ziebarth, Z. M., Acosta, A. C., Arrieta-Quintera, E., Augusteyn, RC, Parel, J-M. Refractive power and biometric properties of the nonhuman primate isolated crystalline lens. *Investigative Ophthalmology and Visual Science.* 2010;51(4):2118-2125.

Borja D, Siedlecki D, de Castro A, Uhlhorn S, Ortiz S, Arrieta E, Parel J-M, Marcos S, Manns F. Distortions of the posterior surface in optical coherence tomography images of the isolated crystalline lens: effect of the lens index gradient. *Biomedical Optics Express.* 2010;1(5):1331-1340.

Brown NP. The change in lens curvature with age. *Experimental Eye Research.* 1974;19:175-183.

Burnat K. Are visual peripheries forever young? *Neural Plasticity*. 2015;2015:1-13.

Charman WN. The eye in focus: accommodation and presbyopia. *Clinical and Experimental Optometry*. 2008;91(3):207-225.

Charman WN, Tucker J. Dependence of accommodation response on the spatial frequency spectrum of the observed object. *Vision Research*. 1977;17(1):129-139.

Charman WN, Radhakrishnan H. Peripheral refraction and the development of refractive error: a review. *Ophthalmic and Physiological Optics*. 2010;30(4):321-338.

Cheng H, Barnett JK, Vilupuru AS, Marsack JD, Kasthurirangan S, Applegate RA, Roorda A. A population study on changes in wave aberrations with accommodation. *Journal of Vision.* 2004;4(4):272-280.

de Castro A, Birkenfeld J, Maceo B, Manns F, Arrieta E, Parel JM, Marcos S. Influence of Shape and Gradient Refractive Index in the Accommodative Changes of Spherical Aberration in Nonhuman Primate Crystalline Lenses. *Investigative Ophthalmology and Visual Science.* 2013;54(9):6197-6207.

de Castro A, Ortiz S, Gambra E, Siedlecki D, Marcos S. Three-dimensional reconstruction of the crystalline lens gradient index distribution from OCT imaging. *Optics Express*, 2010;18(21):21905–21917.

de Castro A, Siedlecki D, Borja D, Uhlhorn S, Parel J-M, Manns F, Marcos S. Age-dependent variation of the gradient index profile in human crystalline lenses. *Journal of Modern Optics*. 2011;58(19-20):1781-1787.

Dubbelman M, Van der Heijde GL. The shape of the aging human lens: curvature, equivalent refractive index and the lens paradox. *Vision Research*. 2001;41(14):1867-1877.

Dubbelman M, Van der Heijde GL, Weeber HA. Change in shape of the aging human crystalline lens with accommodation. *Vision Research*. 2005;45(1):117-132.

Dunne MC. Model for co-ordination of corneal and crystalline lens power in emmetropic human eyes. *Ophthalmic Physiol Opt*. 1993;13(4):397-9.

Dunne MC, Barnes DA, Royston JM. An evaluation of Bennett's method for determining the equivalent powers of the eye and its crystalline lens without resort to phakometry. *Ophthalmic and Physiological Optics*. 1989;9(1):69-71.

Ehrmann K, Ho A, Parel J-M. Biomechanical analysis of the accommodative apparatus in primates. *Clinical and Experimental Optometry*. 2008;91(3):302-312.

El Hage SG, Berny F. Contribution of the crystalline lens to the spherical aberration of the eye. *Journal of the Optical Society of America*. 1973;63(2):205-11.

Enten AC, Nankivil D, Maceo B, Arrieta E, Manns F, Parel J-M. Optomechanical response of primate lenses: effects of decentration. *Investigative Ophthalmology and Visual Science*. 2011;52(14):816.

Fincham EF. The mechanism of accommodation. *British Journal of Ophthalmology*, Monograph Supplement VIII, Pulman & Sons Ltd. London. 1937;7-76.

Fisher RF. The significance of the shape of the lens and capsular energy changes in accommodation. *The Journal of Physiology*. 1969;201(1):21-47.

Gambra E, Sawides L, Dorronsoro C, Marcos S. Accommodative lag and fluctuations when optical aberrations are manipulated. *Journal of Vision*. 2009;9(6):1–15.

Garner LF, Smith G. Changes in equivalent and gradient refractive index of the crystalline lens with accommodation. *Ophthalmology and Visual Science*. 1997;74(2):114-119.

Glasser A, Campbell MCW. Presbyopia and the optical changes in the human crystalline lens with age. *Vision Research*. 1998;38(2):209-229.

Glasser A, Campbell MC. Biometric, optical and physical changes in the isolated human crystalline lens with age in relation to presbyopia. *Vision Research*. 1999;39(11):1991-2015.

Glasser A, Kaufman PL. The mechanism of accommodation in primates. *Ophthalmology*. 1999;106(5):863-72.

Gullstrand, A. Mechanism of accommodation. In H. H. Helmholtz von (Ed.), Handbuch der physiologischen optik (appendix IV, pp. 383–415). (J. P. C. Southall, Trans.: Helmholtz's treatise in physiological optics). New York: Dover. 1909;(Original work published 1962).

Gullstrand, A. How I Found the Mechanism of Intracapsular Accommodation. Nobel Lecture December 11, 1911. Nobel Lectures, Physiology or Medicine 1901-1921, Elsevier Publishing Company, Amsterdam. 1911.

He JC, Burns SA, Marcos S. Monochromatic aberrations in the accommodated human eye. *Vision Research*. 2000;40(1):41–48.

Heys KH, Cram SL, Truscott RJW: Massive increase in the stiffness of the human lens with age: the basis for presbyopia? *Molecular Vision*. 2004;10:956–963.

Helmholtz H. Uber die Akkommodation des Auges. [On the accommodation of the eye] *Albrecht v Graefes Arch Ophthalmol.* 1855;1:1-74.

Hermans EA, Dubbelman M, Van der Heijde R, Heethaar RM. Equivalent Refractive index of the human lens upon accommodative response. *Optometry and Vision Science*. 2008;85(12):1179-84.

Holden BA, Fricke TR, Ho SM, Wong R, Schlenther G, Cronjé S, Burnett A, Papas E, Naidoo KS & Frick KD. Global vision impairment due to uncorrected presbyopia. *Arch Ophthalmol*. 2008;126(12):1731-9.

Huang J, Hung L-F, Ramamirtham R, Blasdel TL, Humbird TL, Bockhorst KH, Smith EL III. Effects of form deprivation on peripheral refraction and ocular shape in infant rhesus monkeys (Macaca mulatta). *Investigative Ophthalmology and Visual Science.* 2009;50(9):4033-44

Ivanoff A. About the spherical aberration of the eye. *Journal of the Optical Society of America*. 1956;46(10):901-903.

Jenkins TC. Aberrations of the eye and their effects on vision. Part 1. *British Journal of Physiological Optics*. 1963;20:59-91.

Jenkins FA, White HE. *Fundamentals of Optics*. New York: McGraw-Hill, Inc. 1976.

Jones CE, Atchison DA, Meder R, Pope JM. Refractive index distribution and optical properties of the isolated human lens measured using magnetic resonance imaging (MRI). *Vision Research.* 2005;45(18):2352-2366.

Kaufman PL. Accommodation and Presbyopia: Neuromusclar and Biophysical Aspects. Adler's Physiology of the Eye, 9th Edition, Hart, William M., Mosby Year Book, Missouri: St. Louis. 1992;391-41.

Kasthurirangan S, Markwell EL, Atchison DA., Pope JM. In vivo study of changes in refractive index distribution in the human crystalline lens with age and accommodation. *Investigative Ophthalmology and Visual Science*. 2008;49(6):2531-2540

Kessler J. Experiments in refilling the lens. *Archives of Ophthalmology.* 1964;71:412-417.

Koomen M, Tousey R, Scolnik R. The spherical aberration of the eye. *Journal of the Optical Society of America.* 1949;39(5):370-376.

Koopmans SA, Terwee T, Barkhof J, Haitjema HJ, Kooijman AJ. Polymer refilling of presbyopic human lenses in vitro restores the ability to undergo accommodative changes. *Investigative Ophthalmology and Visual Science.* 2003;44(1):250-257.

Koretz FK, Bertasso AM, Neider MW, True-Gabelt B, Kaufman PL. Slit-lamp studies of the rhesus monkey eye: II. Changes in crystalline lens shape, thickness and position during accommodation and aging. *Experimental Eye Research.* 1987;45(2):317-326.

Koretz FK, Cook CA, Kaufman PL. Accommodation and presbyopia in the human eye. changes in the anterior segment and crystalline lens with focus. *Investigative Ophthalmology and Visual Science*. 1997;38(3):569-578.

Koretz FK, Handelman GH, Brown NP. Analysis of human crystalline lens curvature as a function of accommodative state and age. *Vision Research.* 1984;24(10):1141-1151.

Manns F, Parel J-M, Denham D, Billotte C, Ziebarth N, Borja D, Fernandez V, Aly M, Arrieta E, Ho A, Holden B. Optomechanical response of human and monkey lenses in a lens stretcher. *Investigative Ophthalmology and Visual Science.* 2007;48(7):3260–3268.

Marcos S. Optical quality of the eye and aging. in wavefront customized visual correction – The quest for supervision II. RR Krueger, RA Applegate, SM McRae Editors. Slack Inc, Thorofare NJ; 2004;101-108.

Marcos S. Aberrometry: Basic Science and Clinical Applications. *Bulletin de la Société Belge d'Ophtalmologie*. 2006;302:197-213.

Marussich L, Manns F, Nankivil D, Maceo Heilman B, Yao Y, Arrieta-Quintero E, Ho A, Augusteyn R, Parel J-M. Measurement of crystalline lens volume during accommodation in a lens stretcher. *Investigative Ophthalmology and Visual Science.* 2015;56(8):4239-4248.

Mathur A, Atchison DA, Charman WN. Effect of accommodation on peripheral ocular aberrations. *Journal of Vision.* 2009;9(12):1-11.

Millodot M. Effect of ametropia on peripheral refraction. *American Journal of Optometry and Physiological Optics.* 1981;58(9):691-695.

Moffat BA, Atchison DA, Pope JM. Age-related changes in refractive index distribution and power of the human lens as measured by magnetic resonance micro-imaging in vitro. *Vision Research.* 2002;42(13):1683-1693.

Mutti DO, Sholtz RI, Friedman NE, Zadnik K. Peripheral refraction and ocular shape in children. *Investigative Ophthalmology and Visual Science*. 2000;41(5):1022-1030.

Mutti DO, Zadnik K, Fusaro RE, Friedman NE, Scholtz RI, Adams AJ. Optical and structural development of the crystalline lens in childhood. *Investigative Ophthalmology and Visual Science*. 39:120-133; 1998.

Nakao S, Ono T, Nagata R, Iwata K. Model of refractive indices in the human crystallin lens. *Japanese Journal of Clinical Ophthalmology*. 1969;23:903-906.

Nankivil D., Manns F, Arrieta-Quintero E, Ziebarth N, Borja D, Amelinckx A, Bernal A, Ho A, Parel J-M. Effect of anterior zonule transection on the change in lens diameter and power in cynomolgus monkeys during simulated accommodation. *Investigative Ophthalmology and Visual Science. 2009;*50(8):4017-4021.

Nankivil D, Maceo Heilman B, Durkee H, Manns F, Ehrmann K, Kelly S, Arrieta E, Parel J-M A. The zonules selectively alter the shape of the lens during accommodation based on the location of their anchorage points. *Investigative Ophthalmology & Visual Science*. 2015;56(3):1751-1760.

Navarro R, Losada MA. Aberrations and relative efficiency of light pencils in the living human eye. *Optometry and Vision Science.* 1997;74(7):540–547.

Navarro R, Moreno-Barriuso E. Laser ray-tracing method for optical testing. *Optics Letters*. 1999;24(14):951-3.

Nishi Y, Mireskandari K, Khaw P, Findl O. Lens refilling to restore accommodation. *Journal of Cataract and Refractive Surgery*. 2009;35(4):374–382.

Parel J-M, Gelender H, Trefers WF, Norton EW. D. Phaco-Ersatz: cataract surgery designed to preserve accommodation. *Graefe's Archive for Clinical and Experimental Ophthalmology*. 1986;224(2):165-173.

Pau H, Krantz J. The increasing sclerosis of the human lens with age and its relevance to accommodation and presbyopia. *Graefes Arch. Clin. Exp. Ophthalmol*. 1991;229:294–296.

Pierscionek BK, Chan DY. Refractive index gradient of human lenses. *Optometry and Vision Science.* 1989; 66(12):822-829.

Pierscionek B, Smith G, Augusteyn RC. The refractive increments of bovine α-, β- and γ-crystallins. *Vision Research.* 1987;27(9):1539-1541.

Pomerantzeff O, Pankratov M, Wang GJ, Dufault P. Wide-angle optical model of the eye. *Journal of Optometry and Physiological Optics.* 1984;61(3):166-176.

Roorda A, Glasser A. Wave aberrations of the isolated crystalline lens. *Journal of Vision.* 2004;4(4):250–261.

Rosales P, Wendt M, Marcos S, Glasser A. Changes in crystalline lens radii of curvature and lens tilt and decentration during dynamic accommodation in rhesus monkeys. *Journal of Vision.* 2008;8(1):1–12.

Rosén R, Lundström L, Unsbo P. Sign-dependent sensitivity to peripheral defocus for myopes due to aberrations. *Investigative Ophthalmology & Visual Science*. 2012;53(11):7176-82.

Ruggeri M, Uhlhorn SR, De Freitas C, Ho A, Manns F, Parel JM. Imaging and full-length biometry of the eye during accommodation using spectral domain OCT with an optical switch. *Biomedical Optics Express*. 2012;3(7):1506-20.

Seidemann A, Schaeffel F, Guirao A, Lopez-Gil N, Artal P. Peripheral refractive error in myopic, emmetropic, and hyperopic young subjects. *Journal of the Optical Society of America A*. 2002;19(12):2363–2373.

Sharma KK, Santhoshkumara P. Lens aging: Effects of crystallins. *Biochimica et Biophysica Acta.* 2009;1790(10):1095–1108.

Sivak JG. The role of the lens in refractive development of the eye: Animal models of ametropia. *Vision Research. 2008;* 87(1):3-8.

Sivak JG, Kreuzer RO. Spherical aberration of the crystalline lens. *Vision Research*. 1983;23(1):59-70.

Smith EL III. Prentice Award Lecture 2010: A case for peripheral optical treatment strategies for myopia. *Optometry and Vision Science*. 2011;88(9):1029-44.

Smith EL III, Hung LF, Huang J. Relative peripheral hyperopic defocus alters central refractive development in infant monkeys. *Vision Res*earch. 2009;49(19):2386–2392.

Smith EL III, Hung LF, Huang J, Blasdel TL, Humbird TL, Bockhorst KH. Effects of optical defocus on refractive development in monkeys: evidence for local, regionally selective mechanisms. *Investigative Ophthalmology and Visual Science*. 2010;51(8):3864–73.

Smith EL III, Kee CS, Ramamirtham R, Qiao-Grider Y, Hung LF. Peripheral vision can influence eye growth and refractive development in infant monkeys. *Investigative Ophthalmology and Visual Science*. 2005;46(11):3965–72.

Smith, G. The optical properties of the crystalline lens and their significance. *Clinical and Experimental Optometry.* 2003;86(1):3-18.

Smith G, Atchison DA. The gradient index and spherical aberration of the lens of the human eye. *Ophthalmic and Physiological Optics.* 2001;21(4):317-26.

Smith G, Cox MJ, Calver R, Garner LF. The spherical aberration of the crystalline lens of the human eye. *Vision Research*. 2001;41(2):235–243.

Smith G, Pierscionek BK. The optical structure of the lens and its contribution to the refractive status of the eye. *Ophthalmic and Physiological Optics.* 1998; 18(1):21-29.

Sun M, Birkenfeld J, de Castro A, Ortiz S, Marcos S. OCT 3-D surface topography of isolated human crystalline lenses. *Biomedical Optics Express*. 2014;5(10):3547-3561.

Tabernero J, Berrio E, Artal P. Modeling the mechanism of compensation of aberrations in the human eye for accommodation and aging. *Journal of the Optical Society of America A*. 2001;28(9):1889-1895.

Tabandeh H, Thompson GM, Heyworth P, Dorey S, Woods AJ, Lynch D. Water content, lens hardness and cataract appearance. *Eye*. 1994;8:125-129.

Thibos LN, Applegate RA, Schwiegerling JT, Webb R, VSIA Standards Taskforce Members. Standards for reporting the optical aberrations of eyes. *Journal of Refractive Surgery*. 2002;18(5):S652-S660.

Thibos LN, Applegate RA, Schwiegerling JT, Webb R, VSIA Standards Taskforce Members. Appendix A: Optical Society of America's standards for reporting optical aberrations. Edited by Porter J, Queener H, Lin J, Thorn K, Awwal AAS. Adaptive Optics for Vision Science: Principles, Practices, Design and Applications. John Wiley & Sons, Inc. 2006:511-528.

Thibos LN, Bradley A, Liu T, Lopez-Gil N. Spherical aberration and the sign of defocus. *Optometry and Vision Science.* 2013;90(11):1284-1291.

Uhlhorn SR, Borja D., Manns F, Parel J-M. Refractive index measurement of the isolated crystalline lens using optical coherence tomography. *Vision Research.* 2008;48(27):2732–2738.

Urs R, Ho A, Manns F, Parel J-M. Age-dependent Fourier model of the shape of the isolated ex vivo human crystalline lens. *Vision Research.* 2010;50(11):1041–1047.

Vilupuru AS, Roorda A, Glasser A. Spatially variant changes in lens power during ocular accommodation in a rhesus monkey eye. *Journal of Vision*. 2004;4(4):299-309.

Walsh G, Charman WN. The effect of defocus on the contrast and phase of the retinal image of a sinusoidal grating. *Ophthalmic and Physiological Optics*. 1989;9(4):398-404.

Weale RD. Presbyopia toward the end of the 20th century. *Surv Ophthalmol*. 1989;34(1):15-30.

Weeber HA, Eckert G, Pechhold W, Van der Heijde RGL. Stiffness gradient in the crystalline lens. *Graefe's Arch Clin Exp Ophthalmol*. 2007;245(9):1357–1366.

Weeber HA, Eckert G, Soergel F, Meyer CH, Pechhold W, van der Heijde RGL: Dynamic mechanical properties of human lenses. *Experimental Eye Research*. 2005;80:425–434.

Welford WT. Chapter 6: Optical Invariants. Pike ER, Welford WT. Aberrations of Optical Systems. Bristol, England. Adam Hilger imprint by IOP Publishing Ltd. 1986:79-129.

Werner LP, Trindade F, Pereira F, Werner L. Physiology of accommodation and presbyopia. *Arq. Bras. Oftalmol*. 2000;63(6): 487-493.

Whatham A, Zimmerman F, Martinez A, Delgado S, Lazon de la Jara P, Sankaridurg P, Ho A. Influence of accommodation on off-axis refractive errors in myopic eyes. *Journal of Vision*. 2009;9(3):1-13.

Wilson BJ, Decker KE, Roorda A. Monochromatic aberrations provide an odd-error cue to focus direction. *Journal of the Optical Society of America A*, 2002;19(5):833-839.

Zadnik K. Myopia development in childhood. *Optometry and Vision Science.* 1997;74(8):603-608.